**The 5-th element**

**A new high pressure high temperature allotrope**


Von der Fakultät für Chemie und Geowissenschaften

Der Universität Bayreuth


zur Erlangung der Würde eines Doctors der Naturwissenschaften


-Dr. rer. nat.-


Dissertation


vorgelegt von

Evgeniya Zarechnaya

aus Moskau (Russland)


Bayreuth, April 2010

# TABLE OF CONTENTS

# SUMMARY

Boron is the fifth element in the Periodic Table known for its structural complexity, unusual types of bonding, and for a rich variety of compounds that it forms. Even the number of its existing or hitherto proven elemental modifications is still under discussion. Despite the fact that the last successful synthesis of rhombohedral $\alpha$-B in form of single crystals was done about 40 years ago and the actual number of interstitial and partially occupied positions of boron atoms in structure of rhombohedral $\beta$-B is uncertain, the existence of these two modifications of boron obtained at ambient conditions is proven beyond doubt.

The present study of boron behavior at high pressures and high temperatures (*HPHT*) comprises various experimental techniques for HP synthesis and material characterization, as well as theoretical modeling. A series of high pressure (up to 20 GPa) and high temperature (up to 1900 °C) synthesis experiments were conducted in multianvil apparatus at Bayerisches Geoinstitut. For testing of the reproducibility of HPHT experiments different types of boron precursors and assemblages for large-volume presses were used.

The synthesis products were studied by X-ray diffraction and spectroscopic methods. The diffraction patterns collected from samples synthesized from highly purified boron powders (> 99.99 % purity) resemble those published by R.H. Wentorf in 1965 and described as a new boron form, but later effectively forgotten. To eliminate any possible contaminations that could take place during the synthesis process, the purity of the HP boron samples was confirmed by scanning electron and transmission electron microscopy and electron microprobe analysis. The structure of this *HPHT* boron polymorph was first unknown, but subsequently determined from our X-ray powder diffraction data and further refined using single-crystal synchrotron diffraction data. The structure was found to be orthorhombic with a *Pnnm* space group and composed of $B_{12}$ icosahedra and $B_2$ dumbbells. The unit cell contains 28 atoms (two icosahedra and two dumbbells) and will be called here $B_{28}$. Atoms in $B_{28}$ are bonded covalently as revealed experimentally by single-crystal X-ray diffraction studies and calculated Electron

Localization Function. The X-ray density of 2.52 g cm$^{-3}$ of this boron allotrope is the highest among its other known modifications.

In order to determine the phase transition boundary between $\beta$-and $B_{28}$ boron phases, *in situ* HP laser heating experiments were performed at European Synchrotron Radiation Facilities (ESRF). It was demonstrated that $B_{28}$ is a stable phase above 9 GPa.

Systematic investigations aimed at the development of the technique of the HP single crystal growth of $B_{28}$ were undertaken. It was found that single crystals of the orthorhombic boron can be grown from metal solutions (Au, Cu, or Pt), i.e. after dissolution in metals at high temperature boron precipitates in form of single crystals with temperature decrease. Experimental products were free from any borides only when Au was used. The maximal length of synthesized $B_{28}$ crystals was ~100 μm and after their isolation high quality X-ray diffraction data was obtained.

Synthesized single crystals of the orthorhombic high-pressure boron phase were studied by means of polarized Raman spectroscopy at ambient conditions. Among all possible 42 Raman-active modes, 32 modes were registered and assigned. Investigation of the high pressure behavior of $B_{28}$ orthorhombic boron was carried out through combining single crystal X-ray diffraction up to 65 GPa and Raman spectroscopy measurements performed up to 105 GPa. Above 40 GPa discontineous behavior in the mode Grueneisen parameter was detected. At the same pressure an inflection in the dependence of the relative volume of a unit cell versus pressure occurs. However, the structure of the material does not change. It is suggested that $B_{28}$ undergoes an isostructural phase transformation, probably due to reducing of the polarity of covalent bonds.

The orthorhombic $B_{28}$ boron reveals extraordinary physical properties. It was found that this material is transparent in thin slides. Due to very strong covalent bonding it has a very high Vickers hardness $H_V$=58 GPa, making $B_{28}$ to be the second hardest elemental material after diamond. The electrical resistance and IR-spectroscopic measurements demonstrated the semiconducter nature of $B_{28}$. Combination of these properties makes the high-pressure boron polymorph a prospective material for industrial applications.

# ZUSAMMENFASSUNG

Bor ist das fünfte Element im Periodensystem der Elemente und ist bekannt für seine strukturelle Komplexität, ungewöhnliche Bindungsarten und eine große Vielfalt von Verbindungen, die es eingeht. Sogar die Zahl der existierenden bzw. bisher belegten elementaren Modifikationen ist immer noch Gegenstand von Fachdiskussionen. Die Existenz zweier Bor-Modifikationen, $\alpha$ –rhomboedrisches und $\beta$ –rhomboedrisches Bor, scheint für Umgebungsdruck zweifellos bewiesen, auch wenn das letzte erfolgreiche Züchten eines Einkristalls aus $\alpha$-B schon ungefähr 40 Jahre zurückliegt und trotz der Tatsache, dass die tatsächliche Anzahl der Bor-Zwischengitterplätze und der nur teilweise von Bor besetzten Gitterpositionen in $\beta$-B ungewiss ist.

Die vorliegende Untersuchung zum Verhalten des Bors bei hohen Drücken und Temperaturen (HP, HT) beinhaltet sowohl verschiedene experimentelle Techniken zur Hochdruck-Synthese und zur Materialbestimmung als auch theoretische Modelle. Eine Reihe von HP-/HT-Synthesen (bis 20 GPa und bis 1900 °C) wurde mit Pressen vom Typ „Multianvil" in den Laboratorien des Bayerischen Geoinstituts durchgeführt. Es wurden unterschiedliche Bor-Ausgangsmaterialien sowie verschiedene Druckwerkzeuge für die großvolumigen Synthesepressen getestet.

Die Versuchsprodukte wurden mit Röntgenbeugungsanalysen und spektroskopischen Methoden untersucht. Die erfassten Beugungsmuster von aus hochreinem Bor (> 99.99 % Reinheit) synthetisierten Proben ähneln denen, in denen R.H. Wentdorf 1965 eine neue Form des Bor beschrieben hatte, die dann aber wieder in Vergessenheit geriet. Um jegliche Kontamination im Verlauf des Syntheseprozesses auszuschließen, wurde der Reinheitsgrad der HP-Borproben mit elektronenmikroskopischen Verfahren (Raster-, Transmissionselektronenmikroskopie, Elektronenstrahlmikrosonde) kontrolliert. Das Gefüge dieses HP/HT-Bor-Polymorphs blieb zunächst unbestimmt, konnte aber im Folgenden durch Auswertung der Röntgenbeugungsmessungen an Pulverpräparaten und weitere Verfeinerung durch Auswertung von Einkristall-Synchrotron-Beugungsdaten identifiziert werden. Das Kristallgitter erwies sich als orthorhombisch, zur *Pnnm*-Raumgruppe und zusammengesetzt aus $B_{12}$-Ikosaedern und $B_2$-Hanteln. Die Einheitszelle enthält 28 Atome

(2 Ikosaeder und 2 Hanteln) und soll hier als $B_{28}$ bezeichnet werden. Die Atome weisen in $B_{28}$ kovalente Bindungen auf, was sich nach Röntgenbeugungsmessungen an Einkristallen und nach Berechnungen mit der Elektronenlokalisierungsfunktion offenbarte. Die durch Röntgenbeugungsverfahren bestimmte Dichte dieses Bor-Allotrops ist mit 2.52 g cm$^{-3}$ die höchste aller anderen bekannten Modifikationen.

Die Grenze des Phasenübergangs von $\beta$- nach $B_{28}$-Bor wurde an der Europäischen Synchrotron-Einrichtung (ESRF) in Grenoble mittels laserbeheizten Proben in Hochdruck-Experimenten *in situ* bestimmt. Es konnte gezeigt werden, dass $B_{28}$ bei Drücken oberhalb von 9 GPa stabil ist.

Systematische Untersuchungen zielten darauf, eine geeignete Methode für die Züchtung von HP-Einkristallen aus $B_{28}$ zu entwickeln. Es zeigte sich, dass Einkristalle aus orthorhombischem Bor in Metalllösungen (Au, Cu, oder Pt) gezüchtet werden können; d. h., dass Bor nach der Auflösung in Metallen unter hoher Temperatur bei sinkender Temperatur in Form von Einkristallen ausfällt. Die Versuchserzeugnisse waren nur dann frei von Boriden jeglicher Art, wenn Gold als Auflösungsmedium verwendet wurde. Die maximale Länge der synthetisierten $B_{28}$-Kristalle lag bei ~100 µm, Röntgenbeugungsmessungen ergaben eine hohe Kristallqualität.

Die erzeugten Kristalle der orthorhombischen HP-Borphase wurden mit Methoden der polarisierten Ramanspektroskopie bei Umgebungsbedingungen untersucht. Von allen 42 möglichen aktiven Raman-Schwingungsarten wurden 32 erfasst und zugeordnet. Für die Untersuchungen über das HP-Verhalten von orthorhombischem $B_{28}$-Bor wurden Röntgenbeugungsmessungen bis zu 65 GPa mit Ramanspektroskopie-Messungen bis 105 GPa kombiniert. Oberhalb von 40 GPa wurde ein diskontinuierliches Verhalten des Grüneisen-Parameters festgestellt. Im gleichen Druckbereich tritt eine Krümmung in der Kurve auf, die das relative Volumen der Einheitszelle in Abhängigkeit vom Druck darstellt. Das Gefüge der Materie ändert sich jedoch nicht, was zu der Annahme führt, dass $B_{28}$ eine Phasenumwandlung unter Beibehaltung der Kristallstructur durchläuft, was auf einer Polaritätsabnahme der kovalenten Bindungen beruhen mag.

Orthorhombisches $B_{28}$-Bor offenbart außergewöhnliche physikalische Eigenschaften. Es zeigte sich, dass das Material in Dünnschliffen transparent ist. Aufgrund seiner starken kovalenten Bindungen weist es eine sehr hohe Vickers-Härte

von $H_V$=58 GPa auf, wodurch es nach Diamant als zweithärteste elementare Materie gilt. Messungen des elektrischen Widerstands und Infrarot-Spektroskopie-Analysen ergaben für $B_{28}$ Eigenschaften eines Halbleiters. Die Kombination dieser Eigenschaften macht diese Hochdruck-Modifikation des Bors für zukünftige industrielle Anwendungen interessant.

# 1    INTRODUCTION


## 1.1  History of the discovery of boron

The humanity is acquainted with boron compounds more than thousand years. In Europe the Latin term "borax" came from Arabic "baurach". Many centuries ago, by "baurach" Arabians understood most of salts and other white crystals. Borax, sodium salt of tetra-boric acid ($Na_2B_4O_7 \cdot 10H_2O$), is white crystalline substance which was used as flux. Another wide-spread natural boron compound is boric acid known since 1777. In 1808, two famous French scientists, J.L. Gay-Lussac and L.-J. Thenard, declared about extraction of chemical element boron by reduction of boron anhydride (as a product of burning of boric acid) by metallic potassium (Albert and Hillebrecht 2009). Several months later, English chemist H. Davy proposed another method of getting boron using electrolysis of melted boron anhydride (Albert and Hillebrecht 2009). It seems that the narration is completed if not one circumstance. In second half of 19-th century, French chemist H. Moissan proved the sensitivity of boron to oxygen. Thus, the products obtained by J.L. Gay-Lussac and L.-J. Thenard could not contain more than 60-70% of boron in outcome products. However, the thermal reduction of $B_2O_3$ by magnesium is yielded in samples with purity less than 90% (Albert and Hillebrecht 2009). German metallurgist F. von Crell improved the H. Moissan method but could not achieve the purity of material higher than 93-94% (Albert and Hillebrecht 2009). Crystalline and amorphous boron, modifications established in 1858 by F. Wöhler and H.E.S.-C. Deville, were seriously criticized in 1876 and attributed to inter-metallic compounds ($AlB_{12}$ and $B_{48}C_2Al$, correspondingly) (Albert and Hillebrecht 2009). In 1909, American scientist E. Weintraub was able to get 99% of pure boron by reduction of boron chloride by hydrogen (Albert and Hillebrecht 2009). Nowadays, there are several ways to achieve elemental boron: by reduction on Ta-wire or in arc melting. In both cases, the presence of impurities is inevitable. Even small amount of additional atoms can significantly affects in physical properties of the material such as melting temperature, and boiling temperature.

## 1.2 Basic chemistry and crystal-chemistry of boron

Boron is the 5-th element in the Periodic table with $1s^2 2s^2 2p^1$ atomic configuration. Its three valence electrons are too localized to form metallic bonding but insufficient in number to create a simple covalent structure. As a compromise, boron atoms form quasimolecular $B_{12}$ icosahedra which can be considered as building block of boron structures and its compounds. 12 atoms of an icosahedron provide 36 valence electrons. For polycentric bonding systems with *n* vertices *2n+2* electrons are necessary to stabilize a *closo*-cluster (Wade 1972). According to this, 26 electrons are used for intra-icosahedral bonds. If icosahedra are arranged in the cubic close packed way, another available 10 electrons of an icosahedron can be involved in the formation of inter-icosahedron bonds with icosahedra of neighboring layers and the neighboring icosahedra in its own layer, forming six two-electron-two center (*2e2c*) bonds and six closed *2e3c* bonds, correspondingly. The fact of possible sharing of two electrons by several centers (more than two icosahedra) reveals in the complex polymorphism of boron structures.

The number of boron polymorphs that became discussed subjects is at least 16 (Donohue 1974, Amberger 1981). However, only two crystalline modifications: *α*-, and *β*-phase are proposed as truly existing pure forms of boron at ambient pressure. Most of other suggested boron allotropes can be stabilized by small amount of impurities, i.e. not a pure boron phases.

The rhombohedral *α*-boron ($R\bar{3}m$ space group, *a*=5.057 Å) (Decker and Kasper 1959) is based on only $B_{12}$ icosahedra located in the corners of lattice (Figure 1.2.1 a). Boron atoms in the unit cell are situated on two crystallographically independent sixfold sites. Each icosahedron has 12 icosahedra neighbors. The actual rhombohedral angle of 58 ° is smaller than in a cubic system. This is explained by the influence of the three-center bonds between the icosahedra. Pure single crystals of *α*-boron were grown by pyrolytic decomposition of $BI_3$ on different substrates (Ta, W, and BN) at temperatures of 800-1000 °C (Mccarty, Kasper et al. 1958). The rhombohedral *α*-boron was found to be stable at temperatures lower than 1200 °C (Mccarty, Kasper et al. 1958).

Under higher temperatures *α*-boron irreversibly transforms into a more complex

*β*-boron with rhombohedral structure (Mccarty, Kasper et al. 1958) with considerably larger unit cell (*a*=10.139 Å, *α*=65.2 °). The structure of *β*-boron consists of icosahedra at the corners and in the middle of the edges, and two $B_{28}$ units (three condensed icosahedra) on the body diagonal linked via an isolated B atom in the center of the rhombohedral unit cell (Figure 1.2.1 b). In addition, there are many partially occupied sites (POS) with occupancy rates that are not integer numbers, varying roughly from 2% to 75% from site to site (Slack, Hejna et al. 1988). If sites with 75% of occupancy would be fully occupied, *β*-boron would be a perfect crystal with 105 atoms in the rhombohedral unit cell. The accurate experimental estimate of number of atoms in rhombohedral unit cell is 106 $^2/_3$ implying violation of rhombohedral symmetry (Ogitsu, Gygit et al. 2009). Due to presence of sites with 75% of occupancy, the coordination of a single B atom in the center of the unit cell is distorted tetrahedral instead of the trigonal-antiprismatic. Theoretically it was obtained that antiferromagnetic correlations in POS occupancy in *β*-boron are related to the suppression of dangling bonds created by the presence of sites with 75% of occupancy which form trimers (Ogitsu, Gygit et al. 2009). Additional unoccupied sites, next to surrounding of trimers, form pairs resulting in the presence of hole-states in *β*-boron. The optimization of structure of β-boron by taking into account these unoccupied sites leads to the result that the structure of *β*-boron calculated from first principles is more stable than *α*-boron polymorph at zero temperature (Ogitsu, Gygit et al. 2009).

The synthesis of tetragonal-I boron (T-50) was described in 1943 (Laubengayer 1943) and its structure was proposed as $B_{50}=B_{48}B_2$. The reproducible synthesis (Ploog K., Kossobut. Kh et al. 1972) by pyrolysis of $BBr_3/CH_4/H_2$ on Ta substrate and $BBr_3/N_2/H_2$ on BN substrate at 1670 K resulted in the formation of $B_{48}B_2C_2$ and $B_{48}B_2N_2$ compounds, respectively. Thus, the preparation of the tetragonal-I form of boron was proved impossible. Later, based on consideration of a close shell configuration it was concluded that $B_{48}B_2$ structure is not stable due to electrons shortage and non-fulfillment of requirement that 12-*sp*-hybrid bonds must find atomic orbitals close enough and in proper direction (Will and Ploog 1974).

However, the reduction of $BBr_3$ by $H_2$ at ambient pressure and temperatures 1200-1600 K on Ta and Re wires yielded formation of the so-called T-192 tetragonal-II

(t-II) boron phase with a density of 2.36 g cm$^{-3}$ (Amberger and Ploog 1971; Ploog and Amberger 1971). But, the synthesis of t-II in the form of single crystals was not reproduced. Thus, the existence of that phase is doubtful.
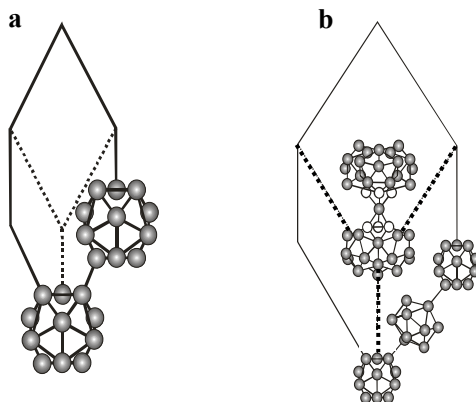


**Figure 1.2.1.** Rhombohedral unit cells of a). *α*-boron and b). *β*-boron. Partially occupied sites formed trimers close to central boron atom are shown by opaque spheres.

Amorphous boron was obtained by reduction of $B_2O_3$ by Mg (Albert and Hillebrecht 2009). The obtained boron modification is usually highly contaminated. During the synthesis process, one of the contaminating substance was $MgB_2$, known since 2001 as a superconductor with a transition superconducting temperature of 39 K (Nagamatsu, Nakagawa et al. 2001). The structure of amorphous boron is based on a statistical arrangement of $B_{12}$ icosahedra and can be characterized by a narrow range (determined by $B_{12}$ icosahedra) and medium range (determined by inter-icosahedral bonds closely related to β-boron) order (Kobayashi, Higashi et al. 1997).

## 1.3   Boron in natural systems

Like lithium and beryllium, boron is a rare element in the cosmos. Due to high volatility, boron is enriched in the Earth's upper continental crust relatively to the primitive mantle (Taylor and Mclennan 1995). Also, boron is soluble in aqueous fluids playing a significant role in geochemistry. Boron minerals form wide range of

geological environments from volcanic fumes to salts deposited in dry climates, and boric acid lagoons to materials formed under granulite-facies conditions.

Usually, boron minerals are oxygen compounds where boron is linked only to oxygen or hydroxyl either trigonally or tetrahedrally. The minerals with $BO_3$ groups are stable at low pressures, while those with $BO_4$ tetrahedra are obtained in deeply subducted rocks.
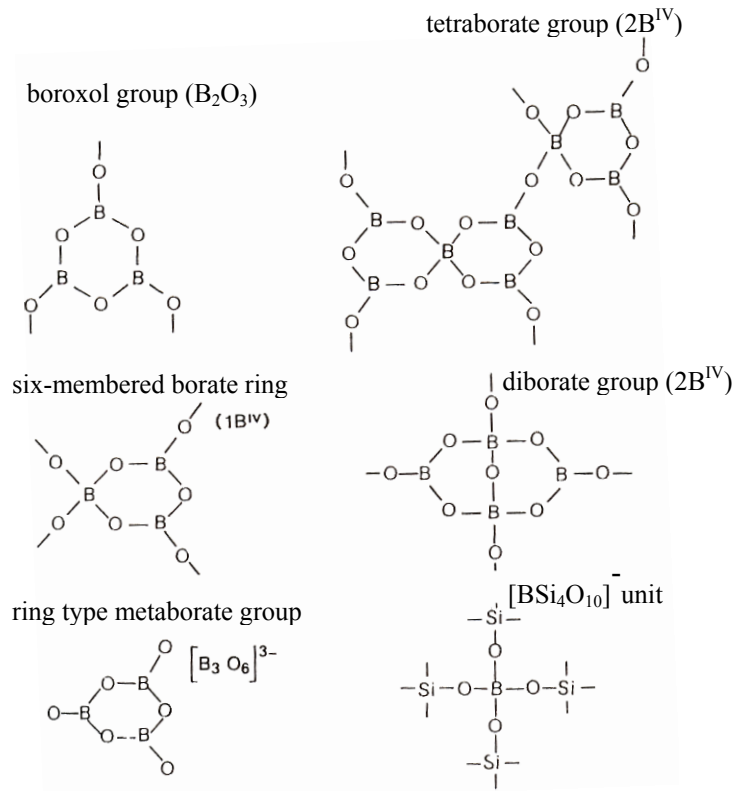


**Figure 1.3.1.** Structure of the borate species.

The oxygen-bearing boron minerals can be grouped into borates (near surface environments) and borosilicates (in depth). In borates, boron polyhedra can be either isolated or share vertices with each other or rarely with Be tetrahedra. While in borosilicates boron polyhedra share vertices with B (making bridges B-O-B) or Si and sometimes with Al and Be tetrahedra. Other types of polyhedra such as $CO_3$, $SO_4$, $PO_4$, and $AsO_4$ are also presented in boron minerals (Gillespie and Robinson 1962).

In general, borates have lower melting and glass transition temperatures than silicates and may be used as flux in producing borosilicate glasses (Pichavant 1987; Dingwell, Knoche et al. 1992). Tourmaline (Figure 1.3.2.) is the most abundant borosilicate and can be appeared in unusual *P-T* conditions (Benard, Moutou et al. 1985).



**Figure 1.3.2.** Watermelon tourmaline.

The presence of boron in magmatic systems is revealed by crystallization of tourmaline. Boron behaves as an incompatible element in igneous systems and concentrated in melt by crystal fractionation. For this reason, boron tends to be enriched in feisic and silicic differentiates of magmatism, i.e. granites. Boron reduces the viscosity of silicate systems melts (Pichavant 1987). This allows magmas migration. As a result, most B-enriched granitic rocks are siliceous and peraluminous. Although, whole rock analyses of granites indicate low B contents in the magmas. Metamorphic processes may result in depletion of boron in the lower crust (Shaw, Truscott et al. 1988; Leeman, Sisson et al. 1992). The relative depletion of boron in granulites is attributed primarily to dehydration during melting reaction where anatexis is may be superimposed on this process.

The basaltic and ultramafic components of oceanic lithosphere are known to absorb boron following hydrothermal alteration at mid-ocean ridges (Thompson and Melson 1970; Humphris and Thompson 1978; Mottl and Holland 1978; Bonatti, Lawrence et al. 1984; Seyfried, Janecky et al. 1984). High temperature hydrothermal phases are associated with the late-magmatic evolution of many types of granites. Boron

may be lost from the melt to the vapor phase if tourmaline is not stable during the magmatic stage.

Principle source of atmospheric B include volatilization from the oceans, particle weathering, gaseous and particulate emissions from volcanoes, wildfires and fuel burning and local release related to mining operations (Fogg and Duce 1985).

The sources of combined boron are sassolite ($H_3BO_3$) found in Italy; colemanite ($Ca_2B_6O_{11.5}H_2O$); ulexite ($CaNaB_5O_{9.8}H_2O$); and kernite (rasorite, $Na_2B_4O_{7.4}H_2O$), in the United States. Ulexite is also found in Bolivia, Chile and Peru. Boracite ($Mg_7B_{10}C_{12}O_{30}$) is found in Germany. The world's major source of boron is kernite from the Mojave Desert in California, USA.

## 1.4   Physical properties of boron and its application

Boron is a trivalent metalloid characterized with black-grayish or dark-brown color in powder. High melting point ($T_m$) of 2076 °C, and high boiling temperature of 3927 °C as well as low thermal expansion of 5-7 $\mu m \cdot m^{-1} \cdot K^{-1}$ (Holcombe 1973) of $\beta$-boron can be explained by strong covalent bonds. Also, covalency reflects on hardness of boron polymorphs, for example, Vickers hardness ($H_V$) of $\beta$-boron is 25-30 GPa (Holcombe 1973). Because of presence of additional partially occupied sites in structure of $\beta$-boron (as discussed above) the bulk modulus of this modification is slightly lower (185-210 GPa (Masago, Shirai et al. 2006)) than the one of $\alpha$-boron (213-224 GPa (Nelmes, Loveday et al. 1993)).

At ambient conditions boron is known to be poor semiconductor; the experimentally determined band gaps for $\alpha$-boron and $\beta$-boron are 2 eV (Horn 1959) and 1.6 eV (Werheit 1970), respectively. Contrary to all metals and most of non-metals, electric conductivity of boron is rapidly increasing with increasing temperature, and at 600 °C it is 100 times higher than at room temperature (Golikova, Zaitsev et al. 1974).

In nature boron is presented in different minerals and its extraction is a multistep technological process which requires high reaction temperatures. A few applications of elemental boron are known.

$^{10}$B is one of two naturally occurring isotopes of boron (the other is $^{11}$B). It has high neutron capture cross-section making boron to be an attractive material for nuclear physics and technology. $^{10}$B is used as a material for the control rods of nuclear reactors, for a radiation shield, and for a neutron counting detector as well as for medicine (boron neutron capture therapy) (Gabel 1997). There are better neutron absorbers, for example samarium, europium, gadolinium, dysprosium, plutonium ($^{239}$Pu, $^{241}$Pu), and cadmium. But boron has advantages of heat-resistance; it is non-toxic and wide-spread in comparison with lanthanides.

Amorphous boron is used in pyrotechnic flares to provide a distinctive green color and also as an ignition source in some rockets. Amorphous boron was applied to high pressure research as a material for gaskets (Lin, Shu et al. 2003). Because of the high strength amorphous boron gaskets for deeper sample chamber provide better hydrostatic conditions, stronger X-ray diffraction from the sample and reduced intensities of diffracted X-rays from a gasket.

Boron is sufficiently reactive to preclude its occurrence in the free state in nature. Boron compounds (borides), due to variety of their physical properties, find large area of applications. Borides are widely used as hard/abrasive materials as well as electronic components in semiconductor industry, and currently found to serve as hydrogen storage compounds.

Boron nitride has remarkable properties and can be used to make a material as hard as diamond (with $H_V$ of 49-54 GPa (Kitamura 2003)). It also behaves like an electrical insulator but conducts heat like a metal. Another high value construction material is boron carbide with $H_V$ of 26.1 GPa (Viala, Gonzales et al. 1992; Pyzik and Beaman 1995). Contrary to boron nitride, it has high heat-resistance and reveals excellent abrasive properties even at high temperature making boron carbide to be useful as grinding material. Hafnium diboride with $T_m$ of 3543 K and a low thermal expansion coefficient is used in thermal shock experiments (Werheit 1995; Imai, Mukaida et al. 2001). The borophosphosilicate/borosilicate glasses are non-conducting and used as insulator layers in semiconductor industry. The chemical stability of borosilicate glasses allows their use as materials for chemical tools. The $TaB_2$ is not corrosive even in the boiling aqua Regis.

Boron composites are high-strength, lightweight materials employed as filaments for advanced aerospace structures and also attractive for applications in personal security (bullet-proof vest) (Hayun, Dilman et al. 2009).



**Figure 1.4.1.** Boron carbide bulletproof plate 70x70 mm$^2$ Trademark: CAEC, China Abrasives Cor.

The saturation of the metal (mostly transition metals) surfaces by boron leads to formation of metal borides (for example, ferroboron). These compounds are also hard and durable materials (Telle 1988; Riedel 1994) and may be used as mechanical parts exposed to high strain (turbine and rotor blades, sports equipment). In addition, metal-borides reveal high electrical conductivity and may serve as electrode materials (Chopra, Luyken et al. 1995). For example, lanthanum hexaboride can be used as thermo-ionic emitter in transmission electron microscopes and especially for electron beam lithography due to very low work function. Recently, it has been proposed for so-called high-performance electronic applications (Yoon, Carroll et al. 2009). The CaB$_6$ was suggested as a "new and semiconducting material for spin electronics" (MillenniumCell). The MgB$_2$ is a superconductor at 39 K and used in form of wires for tomographs. B-rich borides could play an important role as thermoelectric materials of resource-sensitive energy conversion, especially in high temperature applications (Loiseau, Willaime et al. 1996; Zhang, Zhang et al. 2005).

Structural resemblance of boron hydrates (boranes) with organic compounds (for example benzol) result in similarity of their chemical and physical properties. Boranes

first came to public attention as rocket fuels due to their easier oxidation with considerable value of heat of combustion (even higher than in hydrocarbons). Boron hydrogen compounds came to modern technologies as hydrogen-storage materials (for example, $LiBH_4$, $NaBH_4$, $NH_3BH_3$) for fuel cells (Schlapbach and Zuttel 2001; Marder 2007; Zuttel, Borgschulte et al. 2007).

The annual world production of boron and its compounds is about 100 tonnes (Germany: Fa. H. C. Starck, ca. 30 tonnes).
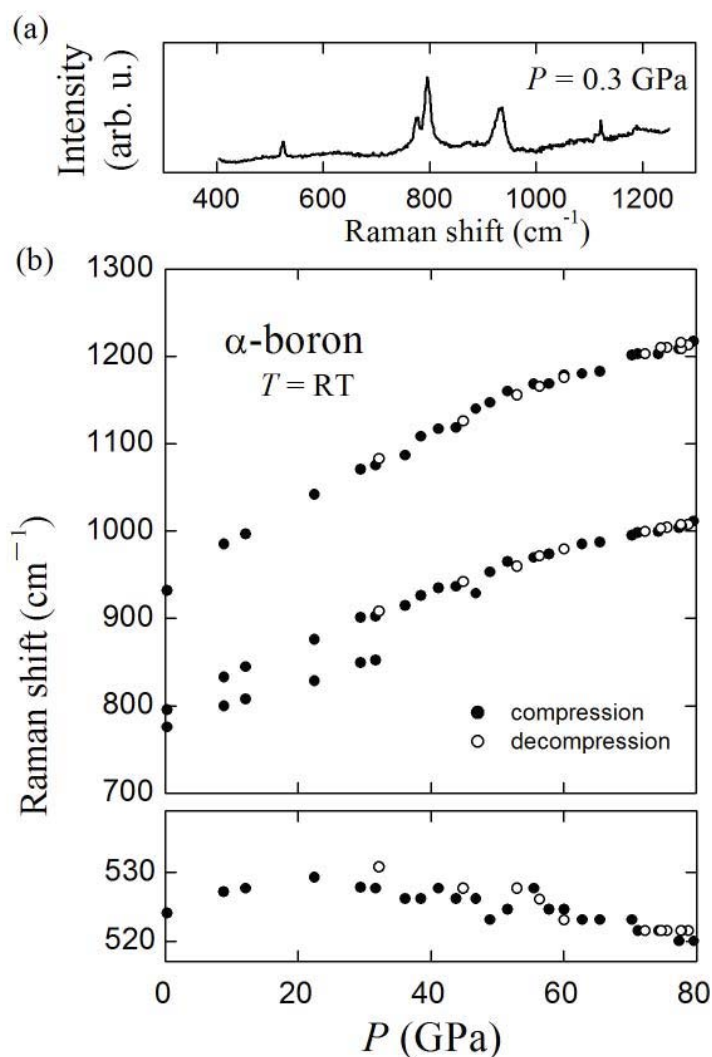
## 1.5 Boron at high pressure

Boron forms quasimolecular structures based on icosahedral units ($B_{12}$) as common building blocks linked in various ways. There is no doubt about existence of *α-* and *β-* rhombohedral boron allotropes at ambient conditions. However, their phase relation is unclear. Even in comparison with other low-*Z* elements, boron remains the least studied at high pressure.

Experimental studies of high pressure behavior of boron were performed by various experimental techniques.

Raman spectrum of *α*-boron between 300 and 1300 $cm^{-1}$ collected at room temperature did not show any discontinuous change at pressures up to 80 GPa, which indicates that no significant structural change occurs (Kaneshige 2007). A low frequency line around 525 $cm^{-1}$ assigned to the librational mode of the icosahedron reveal a softening at pressures above 30 GPa (Figure 1.5.1). This may indicate the possible change in the strength of the interaction between $B_{12}$ icosahedral clusters.

Angle-dispersive X-ray diffraction (ADX) spectra from single-crystal of *β*-boron with 5 μm in dimensions were collected at room temperatures under compression up to 100 GPa. The sample was under good quasi-hydrostatic conditions up to at least 97 GPa (Sanz, Loubeyre et al. 2002). At higher pressures the intensities of the diffraction peaks drastically decreased due to amorphization of the sample (Sanz, Loubeyre et al. 2002). The deterioration of hydrostatic conditions in compression experiments on polycrystalline and single crystal *β*-boron with 7 μm in dimensions was appeared at pressures of 20 GPa and 60 GPa, respectively. In these both experiments it was obtained

that non-hydrostaticity leads to the formation of an intermediate rhombohedral phase with larger unit cell than in *β*-boron (Sanz, Loubeyre et al. 2002). However, the refinement of this phase was not done due to insufficient quality of the ADX spectra.



**Figure 1.5.1.** (a) Raman spectrum of *α*-boron obtained at 0.3 GPa and (b) pressure dependence of Raman lines (Kaneshige 2007).

The high-pressure/high-temperature (*HPHT*) behavior of *β*-boron has been investigated up to 30 GPa using X-ray diffraction techniques (Ma, Prewitt et al. 2003). High *P-T* studies were conducted using double-sided laser heating up to temperatures of 3500 K.

16

From visible observation after heating at 2280 K and 11.7 GPa, the sample revealed red color in transmitted light and opaque in reflected light (Ma, Prewitt et al. 2003). The X-ray diffraction pattern clearly showed a phase transformation compared to that before heating (Figure 1.5.2).
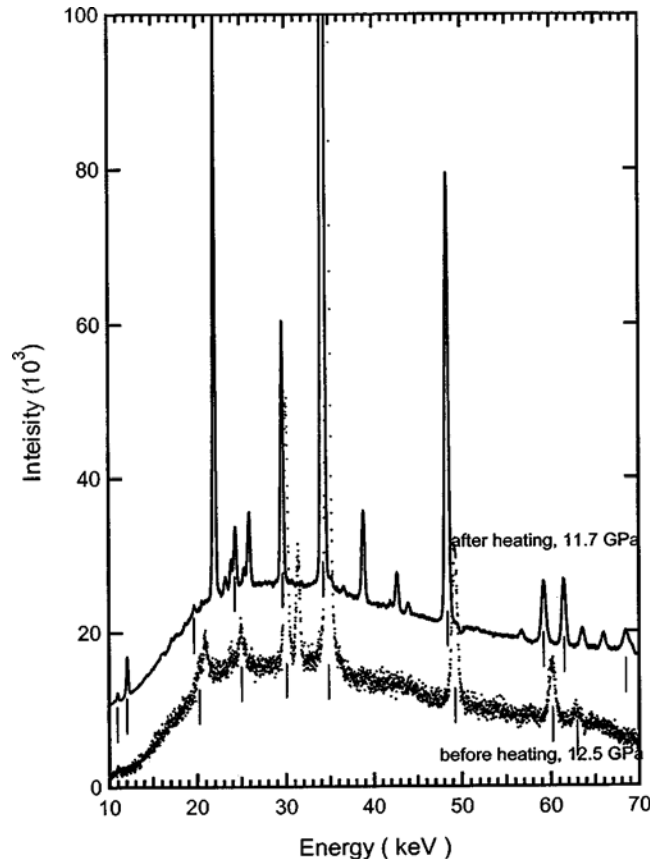


**Figure 1.5.2.** Comparison of diffraction patterns before and after heating at 2280 K. The vertical bar marks the NaCl diffraction peaks, fluorescence and escape peaks. Before heating the pressure measured by ruby was 12.5 GPa. After heating the pressure dropped to 11.7 GPa. NaCl peaks showing higher pressure according to its equation of state, which became comparable after heating (Ma, Prewitt et al. 2003).

The X-ray diffraction patterns measured with the energy-dispersive two-dimensional (Figure 1.5.3) and angle-dispersive methods from the temperature-quenched sample at 11.7 GPa and from the sample quenched to ambient conditions, respectively, fit with those from the tetragonal T-192 boron phase. But, the existence of "tetragonal boron" as a true modification of the pure element is still a subject of debate (Hoard 1970; Naslain 1997).
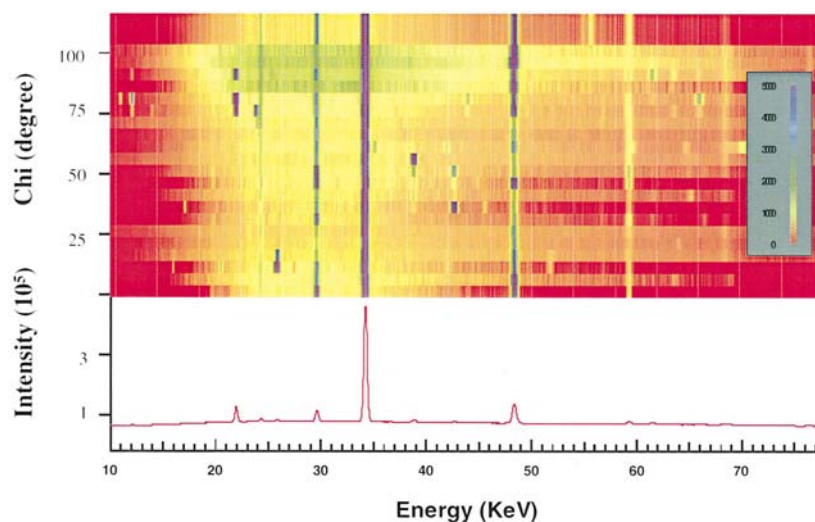
**Figure 1.5.3.** (Color) Step-rotated X-ray diffraction image with an integrated pattern of boron in NaCl at 11.7 GPa. Bottom: calculated pattern from boron T-192 structure with the cell parameter refined from the data at 11.7 GPa (Ma, Prewitt et al. 2003).

In 1965 R.H. Wentorf conducted series of synthesis experiments using of β-boron as a starting material (Wentorf 1965). The β-boron powder was loaded into different assemblages. Capsules were made of Ti or Ta. In some experiments boron particles were insulated from the capsule walls by MgO or mixed with MgO or Si powders. In different experimental runs the samples were heated to temperatures of 1723 K or 2273 K at maximum pressures of 10 GPa or 15 GPa. HPHT synthesis experiments resulted in the formation of a product characterized as dark, pitchlike solid, which was deep red in thin sections. Debye-Scherrer X-ray diffraction patterns of the synthesized samples showed some weak lines corresponding to some of the known forms of boron, together with a strong pattern which could not be attributed to any combination of the known boron polymorphs or borides (Table 1.5.1) (Wentorf 1965). The structural model of this new boron phase was not proposed, and the synthesis was not reproduced until now.

Electrical resistance measurements performed on both α- and β-boron indicate insulator-metal transition in these systems at room temperature and pressures of 112 GPa (Kaneshige 2007) and 175 GPa (Eremets, Struzhkin et al. 2001), respectively. Figure 1.5.4 a shows the increasing of conductivity under compression of β-boron. Under compression of β-boron to 175 GPa and cooling to liquid helium temperature a transformation to a superconducting phase was obtained at 6 K. With further compression

the superconducting transition shifts to higher temperatures (Figure 1.5.4 b). However, the structure of metallic boron is so far unknown.

Phase transformations in boron and its properties were also studied by theoretical methods. The first principles calculations based on density functional theory suggested a transition from $\alpha$-boron structure to body-centered tetragonal (*bct*) phase at 210 GPa (Zhao and Lu 2002). At 160 GPa strengthened boron-boron interactions in $\alpha$-boron broaden both the valence and conduction bands, and eventually lead to the band gap closure and the development of metallic states near the Fermi level (Figure 1.5.5).

**Table 1.5.1.** Debye-Scherrer *d*-values of the synthesized samples (Wentorf 1965).

| Å | Relative intensity * |
|:---:|:---:|
| 4.4 | m |
| 4.1 | m |
| 3.75 | ms |
| 3.50 | m |
| 2.51-2.54 | s |
| 2.30-2.32 | s |
| 2.15 | w |
| 2.10 | w |
| 2.00 | w |
| 1.98 | w |
| 1.68 | w |
| 1.60 | w |
| 1.50 | mw |
| 1.48 | mw |
| 1.45 | m |
| 1.41 | ms |
| 1.39 | m |
| 1.38 | m |
| 1.35 | m |
| 1.3 | m |
| 1.27 | w |

m, medium; s, strong; w, weak.
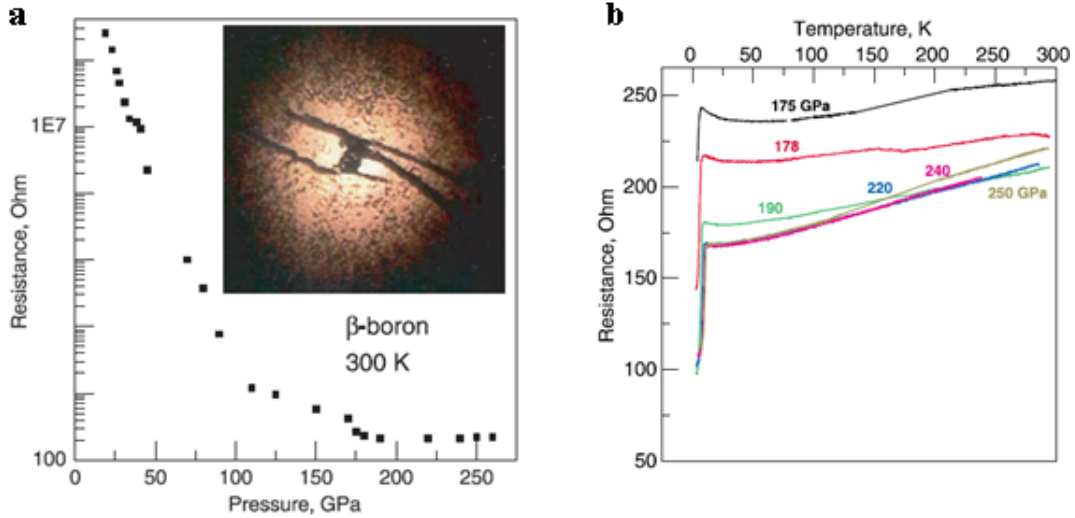
**Figure 1.5.4.** a) Pressure dependence of the resistance of *β*-boron at 300 K. The inset shows a sample in transmitted light at 175 GPa with Pd electrodes; b) Temperature dependence of the resistance of boron (Eremets, Struzhkin et al. 2001).

Considerations of boron in congenetic structures of Al, Ga, and In, i.e. face-centered cubic (*fcc*), *α*-Ga as well as *bct* structures, respectively, reveal possible transition from *α*-boron to *α*-Ga structure at 74 GPa (Haussermann, Simak et al. 2003). The electronic density of states (DOS) of B in the competing *α*-Ga structure has no real band gap but a pronounced pseudogap with an extremely low value of the density of states (0.018 states/eV atom) at the Fermi level (Haussermann, Simak et al. 2003) (Figure 1.5.6).

Modern, evolutionary *ab* initio algorithm implemented in Universal Structure Predictor: Evolutionary Xtallography (USPEX) code allows search the dynamically and thermodynamically stable structure among known or hypothetical forms. Such simulations on boron resulted in so called γ-B phase (Oganov 2009). This γ-B phase with Pnnm space group contains 28 atoms in the unit cell which form structural clusters ($B_{12}$ and $B_2$). The γ-B resembles a NaCl-type structure, with the $B_{12}$ icosahedra and $B_2$ pairs, playing the roles of 'anions' and 'cations', respectively. Charge transfer between these constituent clusters was estimated from Bader theory to be 0.34 and 0.48 based on calculations performed in both local-orbital and in projector augmented wave (PAW) approximations, respectively (Oganov 2009). Thus γ-B can be considered as a boron boride $(B2)^{\delta+}(B12)^{\delta-}$ (Oganov 2009).

20
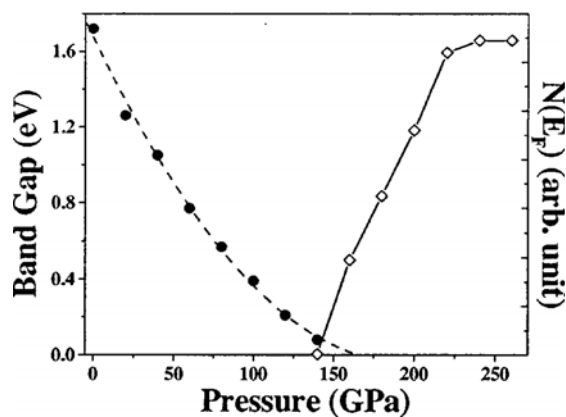
**Figure 1.5.5.** Theoretically predicted band gap (filled dots) and the electronic density of states $N(E_F)$ (open squares) at the Fermi level for $\alpha$-$B_{12}$ as functions of pressure. The extrapolated pressure for band gap closure is 160 GPa (Zhao and Lu 2002).
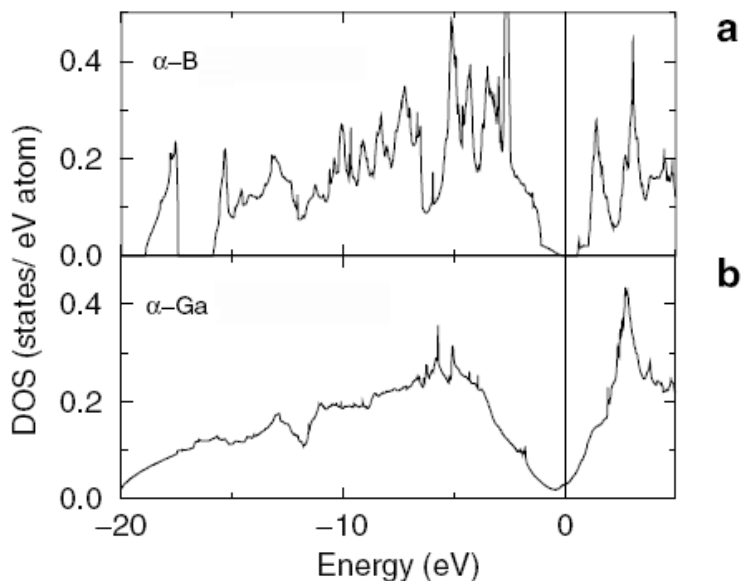


**Figure 1.5.6.** (a) DOS of B in the $\alpha$-B structure at transition pressure (P=74 GPa, $V/V_0$=0.765). (b) DOS of B in the $\alpha$-Ga structure at transition pressure (P=74 GPa, $V/V_0$=0.711) (Haussermann, Simak et al. 2003).

## 1.6   Experimental techniques and sample characterization

In this work, we used an integrated experimental and theoretical approach for investigation of boron and its properties. Experimental methods include high pressure

high temperature (*HPHT*) synthesis and characterization of the synthesized samples. The synthesis procedure was carried out using multi-anvil technique. The studies of the synthesized samples were performed by using of spectroscopic (Raman and IR) techniques and by X-ray diffraction performed as "in house" as well as using synchrotron facilities. Chemical compositions of all the synthesized samples were verified by scanning electron microprobe, transmission electron microscopy, and electron microprobe analysis. The *in-situ* studies of high pressure behavior of the synthesized samples were done by means of the diamond anvil cell technique. Theoretical studies of the phase relations in boron and predictions of the physical properties of the *HPHT* boron allotrope were carried out in framework of "first principles" calculation based on the density functional theory (DFT).

## 1.6.1  High pressure techniques

### 1.6.1.1      Large volume press

In large volume press a set of 6 steel anvils is driven by the force of a hydraulic press. A cubic cavity is filled by 8 tungsten carbide (WC) cubes (Figure 1.6.1.1.1). The truncated corners of WC cubes form an octahedral pressure chamber. A capsule with sample is placed inside an octahedron (Figure 1.6.1.1.2.). The applied force, the octahedral edge length (OEL) and the length of cubes truncation edge (TEL) define the maximum experimental pressure.

The assemblies with OEL/TEL of 14/8 and 18/11 were used to reach the pressures of 12 GPa and 14 GPa, and 12 GPa, 20 GPa. To reduce heat loss by radiation, an octahedron is made of MgO doped with 5% of $Cr_2O_3$. A cylindrical $LaCrO_3$ resistance heater is separated from the octahedron by $ZrO_2$ sleeve. In order to avoid the contamination from the heater, a sample capsule is isolated by a MgO sleeve. As a capsule material, foils of Ta and In, and metallic tubes of Cu, Au, and Pt as well as BN were used in our experiments. Depending on size of assemblies the capsules with ~5.5 $mm^3$ and ~11 $mm^3$ were prepared.

Pressures were calibrated using known phase transitions of common minerals. In all experimental runs the pressure and temperature uncertainties were estimated to be 1 GPa and 50 K, respectively. The details of multi-anvil technique are widely described in a number of publications (Kawai and Endo 1970; Kawai, Togaya et al. 1973; Rubie, Karato et al. 1993; Rubie 1999).



**Figure 1.6.1.1.1.** 18/11 assemblage for Zwick 5000-ton press at Bayerisches Geoinstitut, Germany: second-stage anvils made of eight WC cubes, position of the octahedron surrounded by the pyrophyllite gaskets in the pressure chamber.
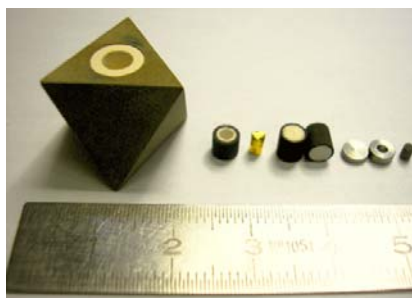


**Figure 1.6.1.1.2.** An octahedron assembly: (MgO+5% $Cr_2O_3$) octahedron; cylindrical $LaCrO_3$ heater with $ZrO_2$ sleeve; Au-capsule; molybdenum (disc and ring); pyrophyllite inset.

In this study, synthesis procedures were carried out using 6-8-type multi-anvil Sumitomo 1200-ton and Zwick 5000-ton presses mounted at Bayerisches Geoinstitut (BGI), Bayreuth Germany. After the gradual compression of samples to the desire pressures, the temperature was increased stepwise at rate of 200 K/min to maximum value depending on capsule materials. Samples were kept under desire temperature for several minutes. The temperature quenching was done by switching off the power and the

quench rate is in the order of 1000 °C/s. Afterwards, decompression for 15-18 hours was started.

### 1.6.1.2        Diamond anvil cell technique

The diamond anvil cell (DAC) technique was applied to investigate the equation of state (EOS), to define the stability origin and to study structural changes of *HPHT* boron polymorph under high pressures. The DAC technique is applicable for various high pressure studies (Hazen 1982, Eremets 1996, Hemley 1998). Diamonds are transparent in the wide range of electromagnetic radiation, from infrared to γ-ray regions, and they keep stable *P-T* conditions for a long time. In the DAC, sample is clamped between polished culets of two diamonds. The pressure that can be reached is determined by the diamond culet size, the maximum pressure of more than 100 GPa was achieved with use of 120 microns in diameter diamond culets. A sample together with a pressure transmitting medium and ruby as a pressure calibrant were loaded in the hole in the Re gasket served as a pressure chamber. The cross-section of DAC is schematically presented in Figure 1.6.1.2.1. The pressure calibration was done by ruby fluorescence method (Mao, Xu et al. 1986). Ruby has a strong fluorescence lines which positions strongly depend on pressure (Figure 1.6.1.2.2).



**Figure 1.6.1.2.1.** Four-pin type diamond anvil cell (left), enlarge view of pressure chamber (re gasket placed between two diamonds) (right).

Chemically inert materials with low absorption and low shear strength in order to provide a hydrostatic condition can be used as a pressure transmitting media. In this study

noble gases of neon and helium were used. Helium has small scattering factor and small thermal conductivity and maintain (quasi)-hydrostatics up to 50-70 GPa (Miletich 2000). During heating under high pressure He incorporates into the hollow carbon cage molecules. This leads to diamond destruction from inside. Thus, laser heating in high pressure experiments was done with use of Ne as pressure transmitting medium.
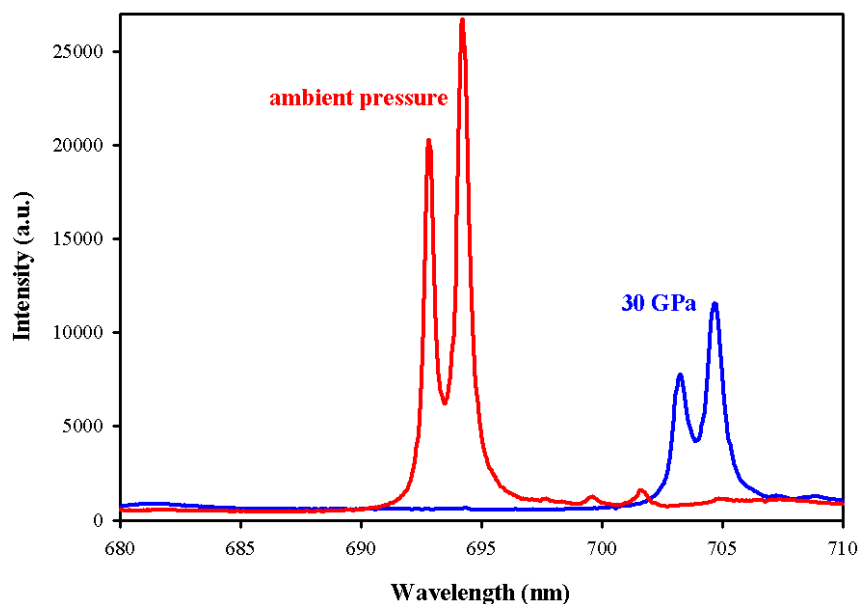


**Figure 1.6.1.2.2.** An example of a shift of ruby fluorescence line with pressure measured by Raman.

## 1.6.2  Methods of sample characterization

## 1.6.2.1  X-ray diffraction

The X-ray diffraction (XRD) is one of the most important and powerful tools for a crystal structure determination and identification of phases and phase mixtures. Also, conducting diffraction experiments at variable pressures and temperatures, the compressibility and thermal expansion of phases can be measured.

X-rays impinging on inorganic materials are scattered in various directions by the atomic electrons. The superposition of the individual waves yields the diffracted beam.

Considering a periodic sequence of atoms (with period *a*), the interference between waves generated by neighboring atoms will be constructive if the Laue equation will be fulfilled:

$$a(cos\alpha_1 - cos\alpha_2) = h\lambda,$$

where $\alpha_1$ is the angle of incidence, i.e. angle between the primary beam and a line defined by the atoms, $\alpha_2$ is the angle between the diffracted beam and this line, $\lambda$ is the wavelength of the radiation and *h* is an integer number.

This equation yields a family of cones coaxial with the line of points as possible location of diffracted radiation. For three dimensional periodic structures tree similar equations have to be fulfilled simultaneously, i.e. diffracted beams are the common intersections of the three Laue cones. This condition is only met when X-rays from very specific directions fall upon the crystal. For this reason, it is necessary to move a single crystal in a space in order to observe its diffraction pattern.

In comparison with formerly used film methods, nowadays, the measurements of the intensities of reflections are much faster and more accurate using an automatic diffractometer. For single-crystal X-ray diffraction experiments the four-circle instruments are common in use (Figure 1.6.2.1.1). The crystal is placed on the goniometer head with the vertical rotation $\varphi$ axis. The "kappa-circle" serves as support for an arm carrying the goniometer head, and it is tilted at 50° to the horizontal. The goniometer head and the "æ-circle" are mounted on an $\omega$-circle, lying in the horizontal plane. Rotational axes of the three computer controlled "circles" of the apparatus intersect with one another; and a crystal must be centered at that point. Then, the single crystal can be oriented relatively to the incident X-ray beam. The forth circle brings the counter to the position for measuring the reflection in the horizontal plane. In such geometry called æ-geometry there is unhindered access from above, and no restrictions on $\omega$.

The direct results of the experimental measurements for a crystal structure are: 1). the unit cell parameters, 2). the space group (or at least a small selection of possibilities), 3). and the intensity data. The final purpose of the structure solution is the location of the

atoms in the unit cell which is realized by a number of methods using modern, very sophisticated software.
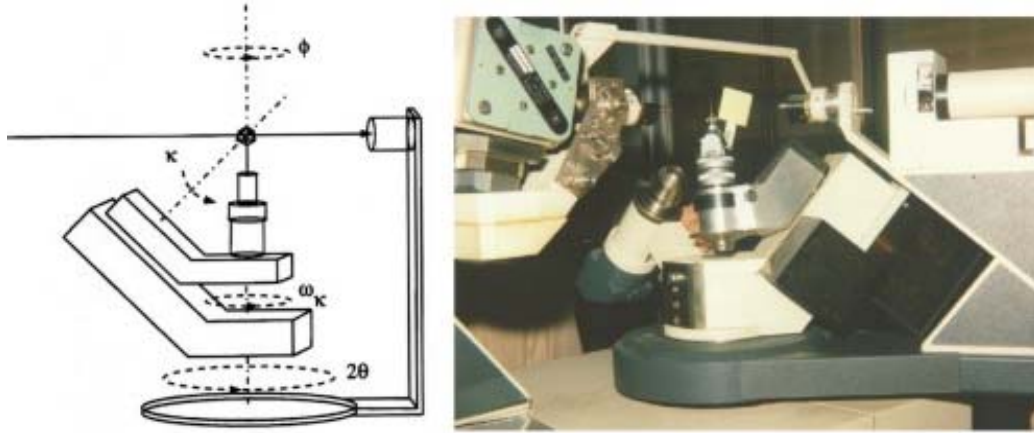


**Figure 1.6.2.1.1.** Scheme of a four-circle goniometer with Kappa geometry

The single crystal methods provide the best possibility for the solution and refinement of crystal structures, but single crystals in many cases are not available. Furthermore, single crystal analysis does not provide information about crystalline material. Microstructural properties and imperfections (dislocations and all kinds of disorder) are not commonly characterized by single crystal analysis. Studies of macroscopic stresses as well as the texture of polycrystalline sample are performed by powder diffraction.

The powder diffraction method was developed in 1916 by Debye and Scherrer. Since atoms in a crystal are periodically arranged, they form families of lattice planes defined by the Miller indices (*hkl*). The X-ray diffraction can be described as a reflection of X-rays by sets of the lattice planes. The condition for constructive interference is described by the Bragg equation:

$$2d\sin\theta = n\lambda,$$

where *d* is the lattice spacing, $\theta$ is the angle of incidence of the X-ray beam, so called Bragg angle, $\lambda$ is the wavelength of the incident X-ray beam and *n* is an integer.

In practice of powder diffraction, the angle between the incident and diffracted X-ray beams *2θ* is measured. The *d*-spacings of the lattice planes, (*hkl*) indices of the reflecting planes and intensities of the diffracted beams are characteristic for a material.

The polycrystalline sample is illuminated by a monochromatic X-ray radiation, and planes of differently oriented crystals, for which Bragg condition is met, reflect. For more than 50 years this method was considered only as qualitative phase analysis due to the loss of angular information: accidental and systematic peak overlap caused by projection of three-dimensional reciprocal space onto one-dimensional *2θ* axis.

The solution of this problem was found by development of the Rietveld method. This technique for crystal structure refinement allows using of entire powder pattern instead of analyzing individual reflection separately. Parameters such as atomic positions, lattice parameters, and experimental factors affect peak-shape and background. For modeling of X-ray diffraction pattern these parameters are varied using least-squares approach, until the agreement between calculated and measured diffraction profiles will be achived. The method was quickly extended from neutron data to in-house X-ray powder diffraction, synchrotron powder diffraction and data from pulsed sources, and to refinements of incommensurate and magnetic structure.

The line-profile fitting of whole-patterns gives better profile description of Bragg-peak intensities resulting in more accurate structure refinements. Experimental effects like multiple scattering, scattering from the sample environments, and fluorescence can also be corrected. The background of the corrected data encodes the local structure information, how it deviates from the average crystal structure in the form of defects and correlated lattice dynamics (phonons). Thus, the powder diffraction pattern contains information additional to the pure crystal structure.

Nowadays, with data quality from synchrotron X-ray sources combined with modern analysis methods one cannot only refine, but also solve crystal structures from powder diffraction data. Determination of even complex crystal structures is becoming a routine method of powder diffractometry. The success depends on choice of measurement device, pattern profile description and structure solving algorithms. For example, using maximum entropy methods combined with high-resolution synchrotron data, details like rotational disorder can be extracted from powder diffraction. Also,

parallel data collection approaches such as 1D and 2D detectors make non-ambient parametric studies possible. Highly monochromatic parallel beam synchrotron radiation reaches an accuracy in the atomic parameters, which allows the interpretation of bonding conditions and reaction mechanism.

A synchrotron is circular particle accelerator producing synchrotron radiation. In an evacuated, ring-shape container charged particles (usually electrons) are forced on a circular orbit by external magnets and accelerated to nearly the speed of light by alternating electric field. Electrons emit very intense electromagnetic radiation with a continuous spectrum from the far infrared to the γ-ray region, called synchrotron radiation. Synchrotron radiation has extremely low beam divergence, strong polarization, and it is emitted in very short pulses, typically less than a nano-second.

With synchrotron radiation it becomes possible to study very small specimens and collection of the data performs in a very short time. The combination of high pressure cells with synchrotron radiation facilities has revolutionized the high-pressure research. X-ray diffraction at high pressures permits investigation of structural properties of solids and covers studies of the crystal structure, the equations of state and phase transitions.

The principle problem of powder diffraction at high pressure is that the distribution of the crystallite orientations in a sample is typically non-random. The texture formation can be thus excluded in single-crystal high pressure diffraction experiments. Such experiments require long time of data collection due to a small amount of the material. Also, for single-crystal experiments conducted with monochromatic radiation, it is necessary to move DAC providing more reflecting planes.

Combination of single-crystal and powder X-ray diffraction methods at high pressure gives comprehensive information on the material under investigation. Principles of powder X-ray diffraction (XRD) in DACs are presented in numerous reviews (see for instance, Fei 2000, Macmahon 2004).

The in-house X-ray powder diffraction studies were conducted using high-brilliance diffractometer installed at Bayerishes Geoinstitut. This system consists of three main components: RIGAKU FR-D high brilliance source, OSMIC Inc. Confocal Max-Flux optics, and SMART APEX 4K CCD detector. The FR-D high brilliance X-ray Mo

rotating anode generator operates at 3.3 kW. The initial elliptical spot, with the FWHM of the vertical axis of ~200 μm and in horizontal direction of ~100 μm, is focused by the Confocal Max-Flux (CMF) optics to a diameter of FWHM of ~40 μm. Thin film multilayers yield a large capture angle and, correspondingly a large flux. The monochromaticity of the beam provides high intensity with small background. Mirrors of CMF optics can be manually placed with the "side-by-side" scheme to optimize the parameters of flux, spectrum and divergence. The SMART APEX CCD detector with sensitivity of ~170 electrons per photon allows data collecting from both powder and single crystal samples.

Although boron is a weak scatterer, the *in-house* powder X-ray diffraction data collected from polycrystalline samples were good enough for the phase identification. For the structure solution from powder X-ray diffraction data and its refinement using the Rietveld method, as well as for investigation of boron behavior under high pressures, use of X-ray synchrotron radiation was a must.

A careful determination of the crystal structure of the high pressure high temperature boron polymorph ($B_{28}$) and investigation of its high-pressure behavior was carried out at the Swiss-Norwegian Beam Lines (SNBL) and the ID-09 beam line, respectively, of European Synchrotron Radiation Facility (ESRF, Grenoble, France).

The X-ray single crystal characterization and the refinement of the crystal structure of *HPHT* boron was carried out at 293 K using a monochromatic beam (0.7146 Å) and MAR345 detector installed at SNBL. The crystal-to-detector distance was 100 mm. 300 frames with exposure time of 5 seconds have been collected. Integration of the intensity and corrections for Lorentz factor and polarization effects were done using CrysAlis software (Oxford Diffraction 2006). The absorption correction and scaling of frames for the residual intensity of the synchrotron beam were performed using SADABS (Sheldrick 1997 (a)). The structure was solved and refined using SHELX program (Sheldrick 1997(b)). Details the data collection and structural refinement are listed in Table 1.6.2.1.1.

In order to find out the stability range of the high-pressure orthorhombic boron and its detailed high-pressure crystalchemistry, XRD measurements were performed with use of the monochromatic X-ray beams with wavelengthes of 0.42 Å and 0.31 Å, and

MAR345 image plate detector and MAR CCD detector installed at ID-09 beam line at ESRF and at IDD-13 beam line at APS, respectively. Either isometric pieces of polycrystalline *HPHT* boron (from experimental run S4120, 14 GPa and 1500 °C, see Table 2.1.2) or single crystals of this phase (from experimental run Z612, 20 GPa and 1600 °C, see Table 2.1.2) were loaded into diamond anvil cells with culets of 300 μm or 250 μm in diameter. Rhenium metal gaskets were indented to the thickness of about 50 μm and holes with diameters of 100 μm were drilled in the center. As pressure transmitting mixture of NaCl and Ar, or Ne or He were loaded. Ruby balls were used as a pressure calibrants. One- and double-side NIR laser heating was conducted at ESRF, and APS. The obtained powder and single-crystal diffraction patterns were integrated using the Fit2D software.

**Table 1.6.2.1.1.** Results of the single crystal analysis of $B_{28}$ obtained at the SNBL

| Parameters | Experimental run Z612 |
|---|---|
| a (Å) | 5.0576(4) |
| b (Å) | 5.6245(8) |
| c (Å) | 6.9884(10) |
| V (Å$^3$) | 198.80(4) |
| Space group | Pnnm |
| *Number* of independent reflections | 233 |
| *Number* of reflections with $F_0 > 2\sigma(F_0)$ | 222 |
| $R_{int}$ | 0.0196 |
| $R_1$ | 0.0387 |
| GoF | 1.100 |
| *No* Refined parameters | 37 |

*where $R_{int} = \sum|F_0 - F_c^2(mean)|/\sum F_0^2$ is the discrepancy factor; $R_1 = \sum||F_0| - |F_c||/\sum|F_0|$ is the final agreement index.

## 1.6.2.2    **Spectroscopic techniques.**

## **Vibrational spectroscopy.**

Raman spectroscopy and infrared (IR) spectroscopy are two forms of vibrational spectroscopy. As the name suggests these form of spectroscopy are tied up with changes in the vibrational state of molecules.

## 1.6.2.2.1    Raman Spectroscopy.

Under illumination by a monochromatic light of energy less than that required to promote a molecule into an excited electronic state, the molecule (atoms of a substance) absorbs the light and a vertual excited state is created. This virtual state is of very short lifetime and the majority of light is re-emitted at the same energy: this is called Rayleigh scattering. The energy of a small portion of the re-emitted light differs from the incident radiation ($v$) by energy gaps that correspond to some vibrational modes. Atomic species could be transformed into higher/lower energy level simultaneously emitting a quant of light. The non-Rayleigh light occurs both at a lower energy, because a vibrational promotion has occurred, and at higher energy, where the energy difference derives from a loss of vibrational energy of the molecule. The low ($v$-$v_l$) and high ($v$+$v_l$) frequency components of a scattered light are called Stokes and anti-Stokes lines, respectively, (Figure 1.6.2.2.1.1).
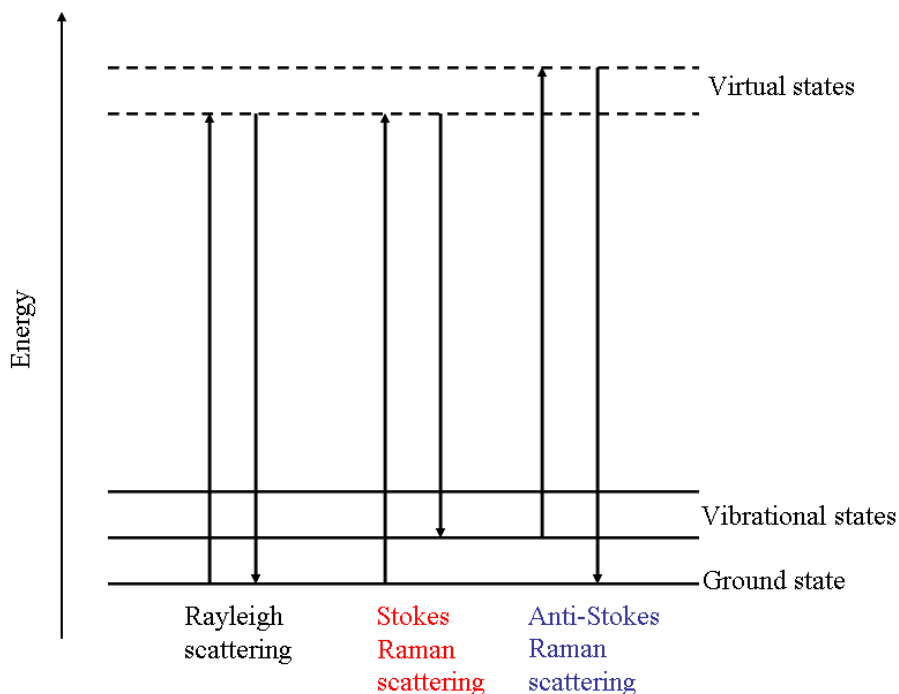


**Figure 1.6.2.2.1.1.** Scheme of photon transitions in molecules under illumination of the monochromatic light.

Even at room temperature the excited vibrational states are less occupied than the ground

vibrational state, and it is therefore more likely that promotion of a ground state molecule into a vibrationally excited state will occur rather than the reverse. The peaks observed at higher frequency ($v+v_l$) than the incident radiation (anti-Stokes lines) are less intense. In practice, due to the Stokes lines are more intense, the Raman shifts of those lines with respect to the Rayleigh line is measured (Figure 1.6.2.2.1.2).
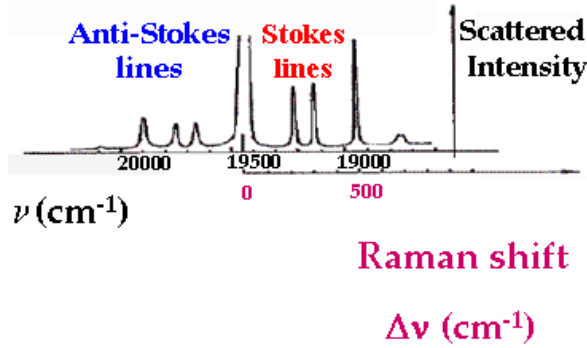


**Figure 1.6.2.2.1.2.** An example of a vibrational spectrum.

The Raman shifts, i.e. bands in a Raman spectrum represent the interaction of the incident light with a certain vibration of the nuclei. The vibrations of the nuclei depend on their sizes and masses, valences, and the forces between atoms, and the symmetry of a crystal structure. These factors affect the number of Raman bands, their relative intensities, their widths and polarizations.

The Raman scattering phenomenon can be described from electrodynamics. Due to interaction with the light wave the electrical dipole moment (*P)* appears on a molecule:

$$\vec{P} = \alpha \vec{E} ,$$

where $\vec{E}$ is the electrical field strength, and $\alpha$ is the polarizability of the molecule.

If the molecule vibrates, $\alpha$ is not a constant but depends on distance between atoms *r*:

$$\alpha = \alpha_0 + \left( \frac{\partial \alpha}{\partial Q} \right) Q + ..., \text{ with } Q = \Delta r.$$

If the angular frequency of the exciting light wave is $\omega$ and *E=Acosωt* (*A* is the

amplitude), and vibration frequency of a molecule is $\Omega$ and $Q=Q_0 \cos \Omega t$, thus,

$$P = A\alpha_0 \cos \omega t + \frac{1}{2}\left(\frac{\partial \alpha}{\partial Q}\right)Q_0 A \cos(\omega + \Omega)t + \frac{1}{2}\left(\frac{\partial \alpha}{\partial Q}\right)Q_0 A \cos(\omega - \Omega)t .$$

The first term contains a spectrum component with light wave frequency, and other terms correspond to anti-Stokes and Stokes, respectively.

Polyatomic molecules or crystals have several types of vibrations. The classification of vibrations is based on group theory. To determine whether the vibration is active in Raman spectra, the selection rule must be applied to each normal vibration. According to quantum mechanics a Raman transition from one state to another, and therefore a Raman shift, can be activated optically only in the presence of non-zero polarizability derivative with respect to the normal coordinate (that is, the vibration or rotation):

$$\left|\frac{\partial \alpha}{\partial Q}\right| > 0 .$$

Raman-active modes can be found for molecules or crystals that show symmetry by using the appropriate character table for that symmetry group. The spectral information arising from polarized Raman analysis gives insight into molecular orientation and vibrational symmetry. The polarization of the Raman scattered light can be measured using (plane) polarized laser excitation and a polarization analyzer. The geometry of the scattering experiment, including the polarizations and the directions of propagation of incident and analyzed scattered light with respect to the crystallographic orientation of the sample is given by Porto notation (Damen, Porto et al. 1966). Thus, for full information on the polarization behavior of Raman bands single crystals should be preliminary pre-oriented with respect to their crystallographic axes. Raman spectra would be obtained for those bands which show the same polarization behavior. The polarization and directional dependence of Raman-active modes is described by the Raman tensors. Spectra acquired with the analyzer set at both perpendicular and parallel to the excitation plane can be used to calculate the depolarization ratio.

Raman spectra are very specific for materials and can be used for the identification and structural characterization of unknown phases. The high pressure behavior of a phase can be monitored by Raman spectroscopy. If Raman spectra are recorded at various pressures and Raman modes are assigned, one can deduce structural changes on the basis of the observed changes in the spectra.

In this work the assignment of Raman modes of the *HPHT* boron phase was done using Raman spectra obtained at ambient conditions. Investigation of the high pressure behavior of the Raman modes (up to ~100 GPa) of $B_{28}$ was carried out on polycrystalline samples using a DAC technique.

Raman spectra were collected using a LABRAM Raman system with a He-Ne laser (632 nm) for excitation. The spectrometer was calibrated using the diamond phonon peak at 1332 cm$^{-1}$. At ambient conditions the instrumental resolution is 2 cm$^{-1}$. The Raman spectra were processed using the PeakFit™ program. The Savitsky-Golay data-smoothing method was applied and peak profiles were described by Voigt functions.

### 1.6.2.2.2    Infrared spectroscopy

Infrared spectroscopy was one of the first spectroscopic techniques to be widespread in its use. In infrared spectroscopy the IR radiation is absorbed by the material, exciting a vibrational mode. Contrary to Raman spectroscopy, a vibration is infrared (IR)-active if the dipole moment is changed during the vibration. The infrared spectrum of a sample is obtained when IR radiation passes through a thin sample of a compound. It is measured which energies of the applied infrared radiation are transmitted by the sample. A monochromatic beam can change in wavelength over time, or a Fourier transformation can be applied to measure all wavelengths at once. The analysis of the absorption characteristics reveals details of the structure of the compound.

In order to determine the band gap of the high pressure high temperature boron phase, the near infrared and optical absorption measurements on a doubly polished slice of the sample with a thickness of 10 μm were performed using a Bruker IFS 120 Fourier transform spectrometer coupled with an all-reflecting Bruker microscope.

A tungsten source was used to collect both near infrared (from 1000 to 10000 cm$^{-1}$) and optical (from 9000 to 25 000 cm$^{-1}$) spectra. The measurement in the near IR region was carried out with a Si-coated $CaF_2$ beam splitter and a narrow-band HgCdT detector. For collecting of optical spectra a quartz beam splitter with dielectric coating and a Si diode detector were used. The spot size on the sample was 400 micrometers. 200 scans were accumulated for each spectrum. Near IR and optical spectra were merged together.

### 1.6.2.3        Electron microscopy techniques

### 1.6.2.3.1        Scanning electron microscopy (SEM)

For verifying morphology of the synthesized samples and for qualitative determination of chemical composition of the present phases a scanning electron microprobe (SEM) analysis was done. The samples were preliminary polished and coated by carbon. A focused electron beam with energy range of 0.2-30 keV scans the surface of the sample. Due to interaction of the electron beam and the matter the signal is produced and detected synchronous to scanning process. By modulation of a cathode-ray tube (CRT) the signal is converted to a virtual image. The signal and resolution basically depend on material. Different types of signals can be generated due to interaction between electron beam and a sample. In this investigation backscattered (BSE) and secondary (SE) electrons were detected.

Backscattered electrons (BSE) are electrons which are scattered on atoms inside the sample and then re-exit its surface. In the energy dispersive spectra of BSE there is a peak close to energy of the primary beam. This energy corresponds to energy of electrons which are backscattered elastically or almost elastically. Such electrons are dominated the BSE signal and their intensity strongly depends on average atomic number ($Z$) of a certain phase and crystal orientation. Thus, the BSE images are useful for visualization of contrast from different chemical phases present in the sample.

The secondary electrons (SE) are electrons of primary beam which lost their energy due to inelastic scattering or electrons that appear from the sample due to

interaction with BSE. These electrons are obtained at low energy side of the spectrum (< 50 eV). Because of their low energy only electrons from a sample surface can come out. Thus, SE are suitable for imaging of a surface morphology determining the contrast.

In this work, SEM analysis was done by SEM LEO Gemini 1530 equipped with Schottky emitter, and use of EBSD technique and energy dispersive X-ray (EDX) analysis.

### 1.6.2.3.2    Electron microprobe analysis (EMPA)

The quantitative chemical analysis of all synthesized products was carried out with Jeol JXA-8200 spectrometer under conditions of 20 keV for acceleration voltage and of 20 nA for acceleration current and in wavelength dispersive mode (WDX). Focused electron beam with size of about several microns was used for samples investigations. For calibration BN, Pt, Au, carbon, MgO were used as standards. All samples and standards were carbon coated with thickness of ~10 nm. Counting time for each element was 20 s at the peak position and 10 s at each background position. ZAF corrections method was applied. For each sample about 100 data points were collected.

### 1.6.2.3.3    Transmission electron microscopy (TEM)

The transmission electron microscope uses a high energy electron beam transmitted through a very thin sample to image and analyze the microstructure of materials with atomic scale resolution. The electrons are focused with electromagnetic lenses and the image is recorded on film. The electrons are accelerated at several hundred kV, giving wavelengths much smaller than that of light. However, the resolution of the electron microscope is limited by electromagnetic lenses aberrations. Even for very thin samples individual atoms are not seen. The brightfield/darkfield imaging modes of the microscope, which operate at intermediate magnification, combined with electron diffraction also give information about the morphology, crystal phases, and defects in a material. The TEM is useful technique for forming a focused electron probe of very fine

features in the sample for microdiffraction or analysis of X-rays for compositional information similar to EMPA and SEM analysis discussed above. The spatial resolution for this compositional analysis in TEM is much higher, on the order of the probe size. But, the signal is much smaller and therefore less quantitative.
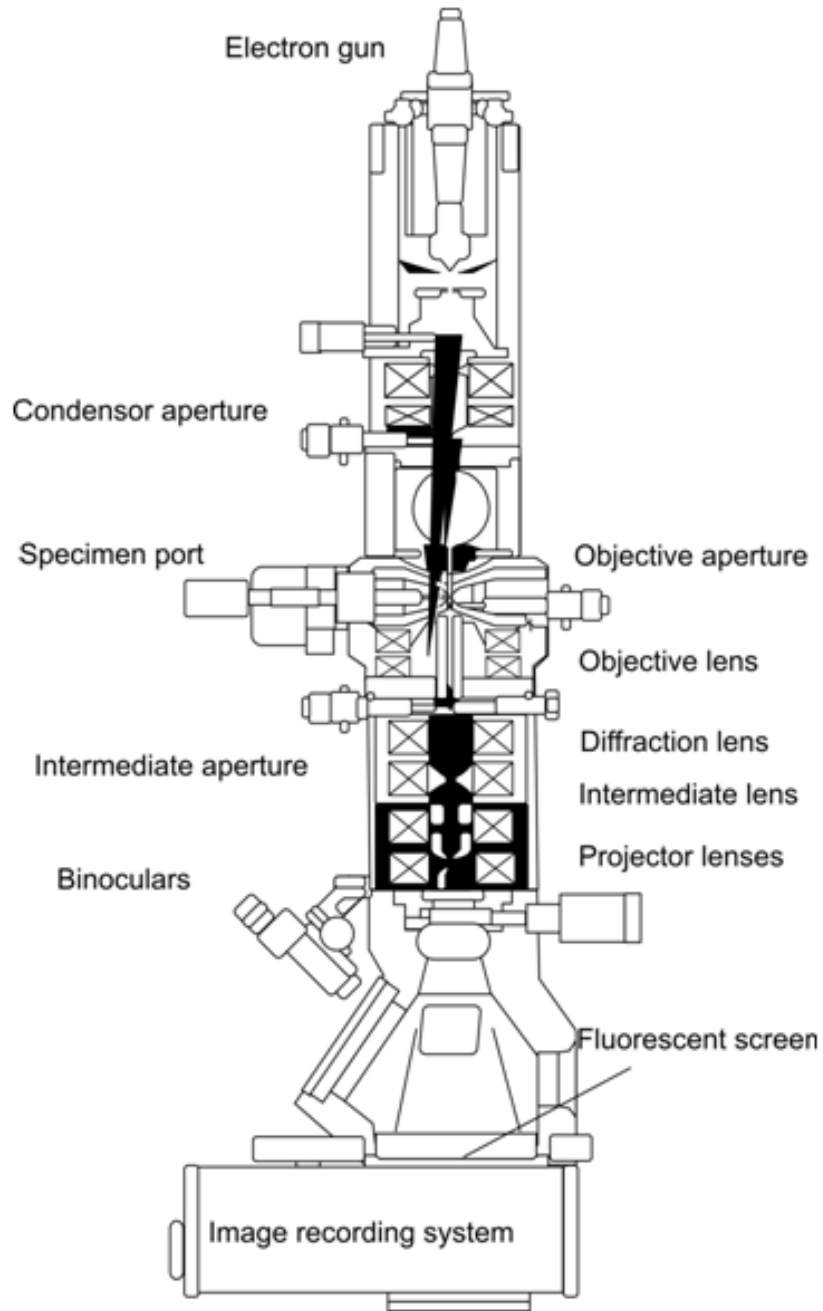


**Figure 1.6.2.3.3.** Scheme of optics in a basic TEM.

In present work, the confirmation the purity of the synthesized sample and its structural determination was carried out by means of a Philips CM20 FEG analytical transmission electron microscope, operating at 200 kV.

## 1.7 Theoretical methods

Stability of a phase and its thermodynamic properties are determined by a thermodynamic potential which at fixed external conditions (temperature ($T$) and volume ($V$)) is the Helmholtz free energy of the system, $F_{syst}$. The stable phase has the minimal free energy among all possible structural configurations. The thermodynamic properties of the stable phase can be calculated from a volume dependence of the free energy. For example, pressure at a given volume is defined as the first order energy derivative with respect to the volume, bulk modulus is described by the second order derivative, etc. First-principles calculations of properties of a material require a solution of the Schrödinger equation for the electronic subsystem:

$$H\Psi(r_1,\sigma_1,r_2,\sigma_2,...,r_{Ne},\sigma_{Ne},R_1,R_2,...,R_{N_N})=E_{el}\Psi(r_1,\sigma_1,r_2,\sigma_2,...,r_{Ne},\sigma_{Ne},R_1,R_2,...,R_{N_N})$$

where many-electron wave function $\Psi$ depends on coordinates $r_i$ and spins $\sigma_i$ of all $N_e$ electrons and coordinates $R_\alpha$ of all $N_N$ ions in the system, and the Hamiltonian in atomic units ($\hbar^2=2m=e^2/2=1$, where $\hbar$ is the Planck constant, $m$ the electron mass, and $e$ the electron charge), $H=-\sum_i\nabla_i^2+v(r_1,\sigma_1,r_2,\sigma_2,...,r_{Ne},\sigma_{Ne},R_1,R_2,...,R_{N_N})$, is defined by the many-electron potential $v$.

Free energy can be written as $F=E_{el} + E_{ion} + F_{lv}$, where $E_{ion}=\sum'_{R_\alpha,R_\beta}\dfrac{Z_{R_\alpha R_\beta}}{|R_\alpha - R_\beta|}$, and $F_{lv}$ is the free energy of lattice vibrations, and stroke in sum $\sum'$ means summation on $R_\alpha \neq R_\beta$.

In real systems the number of atoms is of order $10^{23}$ and the number of electrons is one order of magnitude higher, thus, any direct solution of Schrödinger equation seems to be impossible. Fortunately it is not necessary. In practice, a number of approximations

are used. The first important approximation is known as Born-Oppenheimer's approximation. It employs the fact that ions are much heavier than electrons, so the electron subsystem can always be considered as being in equilibrium with respect to the ions, i.e. the electron distribution in the system is always adjusted to the momentary configuration of the ions.

Also, the real wave function $\Psi(r)$ can be factorized on some basis set of functions $\phi_j$ $(r)$: $\psi(r) = \sum C_j \phi_j(r)$. Due to the crystal symmetry the number of atoms in a system involved in the Schrödinger equation decreases to a number of atoms in the unit cell. So the wave function can be written in the Bloch formulation (Ashcroft 1976): $\psi(r+T) = \exp(ikT)u(r)$, where $T=R_\alpha-R_\beta$ is a translation of crystal lattice, $u(r)=u(r+T)$ is a periodic function with a period of the crystal, and $k$ is a vector in the reciprocal space (also called a quasi-momentum). Wave functions rapidly oscillate in the atomic core region, but such oscillations are not involved into determination of the energy spectrum of the valence electrons. Thus, a real potential can be substituted by a so-called pseudopotential (Harrison 1966) whose wave functions coincide with the wave functions of a real atom over some radius $R_c$ and are smooth inside the atomic core region: $\phi_V^{PS} = \phi_V + \sum_c a_{Vc}\phi_c$, thus $\left[ H + \sum (\varepsilon_V - \varepsilon_c) \mid \phi_c >< \phi_c \mid \right]\phi_V^{PS} = \varepsilon_V^{PS}\phi_V^{PS}$. The difference between the pseudopotential, pseudowavefunction and corresponding exact functions are schematically shown in Figure 1.7.1. The common requirements for construction of pseudofunctions are: 1) they must be described with a minimal number of plane waves; 2) their spatial logarithmic derivatives must agree with those for real functions; 3). the first-order energy derivatives of a real and a pseudo functions have to be coincided. A number of pseudopotentials such as norm-conserving pseudopotentials (Hamann 1979); pseudopotentials based on analytical representation in the sphere with $R_c$ radius (Kerker 1980); transformation of semi-local into non-local potentials (Bylander, Kleinman et al. 1982); and ultra-soft potentials (Vanderbilt 1990) were described. In the present work, calculations of the *HPHT* boron were performed via the projector augmented-wave (PAW) method (Blochl 1994). In this method, the linear transformation of pseudowave functions in real functions is used and the PAW functional for the total

energy is sequentially converted into the Kohn-Sham functional described below. The exact and the pseudowave functions are tied linearly:

$$| \psi_n >= | \widetilde{\psi}_n > + \sum (| \phi_i > - | \widetilde{\phi}_i >) < \widetilde{p}_i | \widetilde{\psi}_i >,$$

where $\widetilde{\psi}_n$ is a pseudofunction, and index $i$ corresponds to a complex of indexes: atomic position, angular and magnetic quantum numbers, etc.; and $\widetilde{p}_i$ is a projector-function.
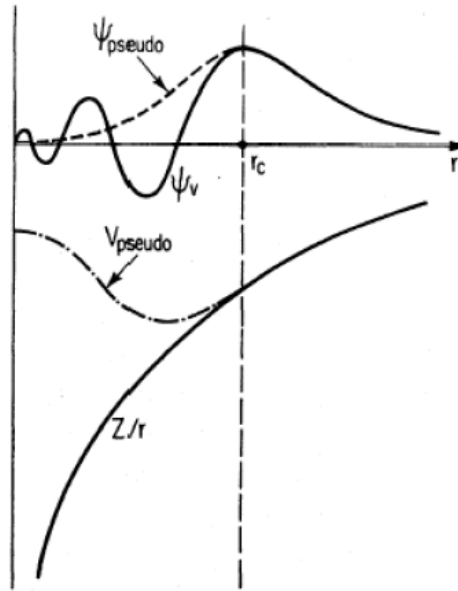


**Figure 1.7.1.** Illustration of substitution of a real wave function and a potential by pseudofunctions.

The electron density can be written as $n(\vec{r}) = \widetilde{n}(\vec{r}) + n^1(\vec{r}) - \widetilde{n}^1(\vec{r})$, the first term is a pseudoelectron density calculated directly from pseudowave functions; and next two terms correspond to the exact and pseudodensities calculated using a radial scale (with radius $r_{rad}$) constructed around each atom.

Next step in solving of Schrödinger equation is the transition from many-electron wave function $\Psi(r_1, \sigma_1, r_2, \sigma_2, ..., r_{Ne}, \sigma_{Ne}, R_1, R_2, ..., R_{N_N})$ to a single electron model based on the density functional theory (Hohenberg and Kohn 1964; Kohn and Sham 1965). The

Hamiltonian can be presented as $H=T+U+V$, where T is the kinetic energy operator, U describes electron-electron interaction, and V corresponds to an external potential $v$. If this potential is known, the density is also defined. The Hohenberg-Kohn theory says that such potential $v$ is unique for the corresponding density, and accordingly can be described as the density functional, thus, density ($\rho$) defines all other ground state properties. The functional for $\rho$ corresponding to the ground state density is equal to the ground state energy whose value is minimal:

$$E_v[\rho] = \int v(r)\rho(r)d^3(r) + F[\rho],$$

where functional $F[\rho]$ is a sum of kinetic and electron-electron energy; written with bracket-description $F[\rho] = \langle \psi \,|\, T + U \,|\, \psi \rangle = \int \psi(r)^*(T+U)\psi(r)d^3(r)$.

Thus, the ground state energy can be written as $E_v[\rho] = T_s[\rho] + \int v(r)\rho(r)d^3(r) + \int \frac{\rho(r)\rho(r')}{|r-r'|} + E_{xc}[\rho]$. The last term includes all many electrons effects. A self-consistent solution of a system of single electron equations (Kohn-Sham variation algorithm):

$$
\begin{aligned}
H\Psi &= (-\nabla^2 + v_{eff})\Psi = E\Psi \\
\rho &= \sum_{occ} \Psi * \Psi \\
v_{eff} &= v_H(\rho) + v_{xc}(\rho) + v_{ext}(\rho)
\end{aligned}
$$

defines electron density of the ground state. Effective potential $v_{eff}$ consists of the Hartree potential $v_H = v_{ee}$, exchange-correlation potential $v_{xc}(\rho) = \frac{\delta E_{xc}[\rho]}{\delta \rho}$, and the external Coulomb interaction due to the ions.

For describing the exchange-correlation effects the approximation of the local density (LDA) (Hohenberg and Kohn 1964; Kohn and Sham 1965) is applicable: $E_{xc}(\rho) = \int \varepsilon_{xc}[\rho(r)]\rho(r)d^3(r)$, where $\varepsilon_{xc}[\rho(r)]$ is the density of exchange-correlation energy of a uniform electron gas with density $\rho(r)$. If the density of the exchange-

correlation energy is not homogeneously distributed around the atom the gradients of density: $E_{xc}(\rho) = \int \rho(r)\varepsilon_{xc}[\rho(r), \nabla\rho(r)]d\ (r)$. Such an approximation is called the Generalized Gradient Approximation (GGA) (Perdew, Burke et al. 1996).

# 2    SYNOPSIS (Scope of articles)

Figure 2. summarizes experimental and theoretical results on high-pressure high-temperature behavior of boron discussed in previous chapter.

Experimentally it was found that at room temperatures $\alpha$-boron is stable to pressure of 80 GPa (dot-line connecting red circles) (Kaneshige 2007), while $\beta$-boron is stable to at least 97 GPa (red hatched area) (Sanz, Loubeyre et al. 2002), and at 100 GPa it turns amorphous (Sanz, Loubeyre et al. 2002) (green diamond). Non-hydrostatic compression above 20 GPa favors a displacing structural change in $\beta$-boron leading to formation of different rhombohedral structure with larger unit cell than in $\beta$-boron (blue diamonds) (Sanz, Loubeyre et al. 2002).

Heating at high pressures drastically affect phase relations of boron (Ma, Prewitt et al. 2003), but experimental results are not in agreement with each other. The synthesis experiments performed by R.H. Wentorf at 10-15 GPa and 1773-2293 K (green hatched area in Figure 2.) resulted in the formation of yet unknown phase (Wentorf 1965). Under compression at higher temperatures (2280 K at 11.7 GPa and 3500 K at 30 GPa) transition $\beta$-boron→T-192 boron (blue area in Figure 2.) occurs, but the reversibility of this phase transition was not demonstrated (Ma, Prewitt et al. 2003). Different theoretical studies predicted structural change of $\alpha$-B in to phase with $\alpha$-Ga structure (Haussermann, Simak et al. 2003) (green triangle in Figure 2.) or in (Zhao and Lu 2002) to (*bct*) structure (green-edge triangle), accompanied by insulator-metal transition at 74 GPa and 210 GPa, respectively. In the pressure range of 19-89 GPa the $\gamma$-B phase was proposed to be stable (blue line) (Oganov 2009).

Theoretical and experimental studies argue over the conditions at which the transition to metallic state occurs. Experiments on compression at room temperature of $\alpha$-boron indicated a transition to a metallic state at 112 GPa (blue-edge circle) (Kaneshige 2007). Metallization of $\beta$-boron occurs at higher pressure of ~160 GPa, and with further compression to 175 GPa it transforms into a superconducting phase at 6 K (Eremets, Struzhkin et al. 2001). The critical temperature of the transition increases with pressure increase and reaches 11.2 K at 250 GPa (green dash-line connecting two green-edge circles) (Eremets, Struzhkin et al. 2001).
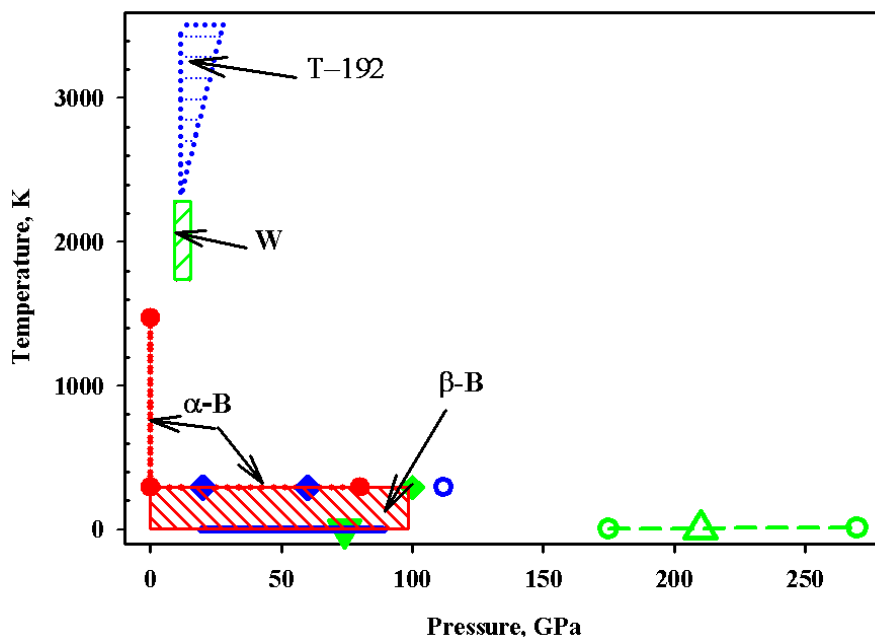
**Figure 2.** High pressure high temperature phase diagram of boron summarizing experimental and theoretical studies. Experiments: red circles (Ogitsu, Gygit et al. 2009) and red hatching (Sanz, Loubeyre et al. 2002) (stability of $\alpha$- and $\beta$-B, respectively); green diamond (Sanz, Loubeyre et al. 2002) (amorphization of $\beta$-B); green hatching area (Wentorf 1965) (unknown phase, result of synthesis experiments performed by R.H. Wentorf); blue area (Ma, Prewitt et al. 2003) (appearance of tetragonal T-192 boron phase); blue-edge circle (Kaneshige 2007) and green-edge circles connected by green dash line (Eremets, Struzhkin et al. 2001) (metallization of $\alpha$- and $\beta$-B, respectively). Theory: green triangle down (Haussermann, Simak et al. 2003) ($\alpha$-Ga); green-edge triangle (Zhao and Lu 2002) (B in *bct* structure); blue line (Oganov 2009) ($\gamma$-B).

There are controversies between experimental and theoretical studies of phase relation in boron at high pressure; none of theoretically proposed *HP* boron phase was obtained yet. The high pressure high temperature part of phase diagram of boron is poorly investigated, and, in fact, studies are restricted with consideration of pressure range to 30 GPa at temperatures above 1500 K.

The goal of my study was systematic investigation of boron behavior at high pressures and temperatures combining experiments in large-volume presses and diamond anvil cells and methods of detail material characterization (including X-ray powder and single-crystal diffraction, Raman spectroscopy, SEM, and TEM), as well as first principal theoretical methods.

In framework of present study, series of high pressure (up to 20 GPa) high temperature (up to 1900 °C) synthesis experiments were conducted using various types of boron precursors and assemblages for large-volume presses. The synthesis products were investigated and led to finding high-pressure high-temperature (*HPHT*) boron phase with yet unknown structure. The structure was solved from X-ray powder diffraction data and refined using single crystal synchrotron diffraction data. *In situ* high pressure laser heating experiments were performed for determination of the boundary of phase transition between *β*-and *HPHT* boron phases. We also develop method of single-crystal growth of *HPHT* boron phase. Physical properties (compressibility, electrical conductivity, mechanical properties, etc.) as well as behavior of the material at high pressure were performed on polycrystalline and on single-crystal samples implying various methods. We demonstrate that high pressure high temperature boron phase is superhard, has low compressibility, optically transparent, and semiconducting.

## 2.1 Synthesis procedure of HPHT boron

In order to understand behavior of boron under high pressure and high temperature (*HPHT*) series of synthesis experiments were carried out using multianvil apparatuses (Sumitomo 1200-ton and Zwick 5000-ton presses) operated at BGI. Various types of boron precursors of different chemical purity and grain sizes were used for *HPHT* synthesis (see Table 2.1.1).

Boron powders were loaded into BN, Au, Pt or In capsules. The size of the capsule tied with the size of the assembly (OEL/TEL) (see section 1.6.1.1) defines the maximum pressure which can be attained during synthesis. Capsules with diameter of 2.0 mm (2.6 mm) and the height of 2.7 mm (3.5 mm) for 14/8 and 18/11 assemblies, respectively, were prepared for *HPHT* synthesis experiment performed at 12 GPa, 14 GPa, and 20 GPa. The samples were heated betwee 2-7 minutes at maximum pressure, then, quenching was done by switching off power. The heating temperature was chosen depending on the capsule material. The details of experimental conditions are listed in Table 2.1.2.

The quenched samples were analyzed with respect to structure, texture and

chemical composition.

The in-house X-ray powder diffraction studies were conducted using high-brilliance diffractometer (see section 1.5.2.1) installed at BGI. Depending on the purity of the starting material the X-ray diffraction spectra of the synthesized samples shown in Figure 2.1.1 differ from one another.

**Table 2.1.1.** Starting materials for *HPHT* synthesis experiments

| Powder | Purity | Company |
|---|---|---|
| *β*-boron | 99.6% | Goodfellow Inc. |
| *β* -boron | 99.995 % | Chempur Inc. |
| *β*-boron, isotope $^{10}$B | 99.95% | Sigma-Aldrich Inc. |
| *β*-boron, isotope $^{11}$B | 99.7% | Sigma-Aldrich Inc. |
| *A*-boron | 97% | Inorganic Chemestry Institute, Kiev, Ukraine |
| amorphous | 95-97% | Chempur Inc. |
| amorphous | 98% | Goodfellow Inc. |

**Table 2.1.2.** Conditions of experiments on synthesis of the orthorhombic *HPHT* boron phase

| Experiment | Starting material | Conditions | | | |
|---|---|---|---|---|---|
| | | Capsule material | Temperature (°C) | Pressure (GPa) | Heating time (min) |
| S4096 | *β*-boron | BN | 1800 | 14 | 3 |
| S4120 | *β*-boron | Au | 1650 | 14 | 3 |
| Z628 | *β*-boron | In | 1600 | 20 | 5 |
| S4285 | *β*-boron, isotope $^{10}$B | Au | 1500 | 14 | 7 |
| S4141 | Amorphous boron | Au | 1500 | 14 | 5 |
| S4202 | *α*-boron | Au | 1650 | 14 | 6 |
| S4228 | *β*-boron, isotope $^{11}$B | Au | 1650 | 14 | 4 |
| Z612 | *β*-B | Pt | 1600 | 20 | 5 |

The X-ray diffraction patterns of the samples synthesized from highly purified (> 99.7 %) *β*-boron powders resemble those reported by R.H. Wentorf (Wentorf 1965) (Figure 2.1.2). For some period of time the phase obtained by R.H. Wentorf (Wentorf 1965) was considered pure high pressure boron polymorph and was included into Powder Diffraction Database (PDD, #00-017-0788). However, the structure of this new *HPHT* boron form was not determined. Since some lines in Wentorf's X-ray diffractogram could

be explained as those from boron suboxides or/and carbides this phase was later discarded from the consideration as a truly existing boron phase.
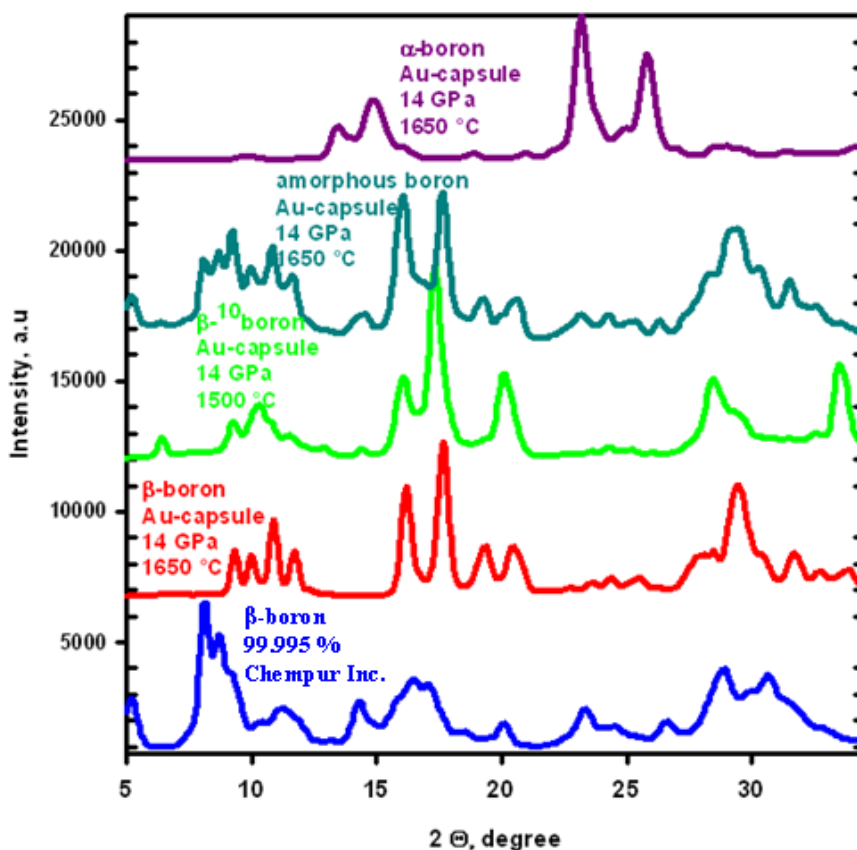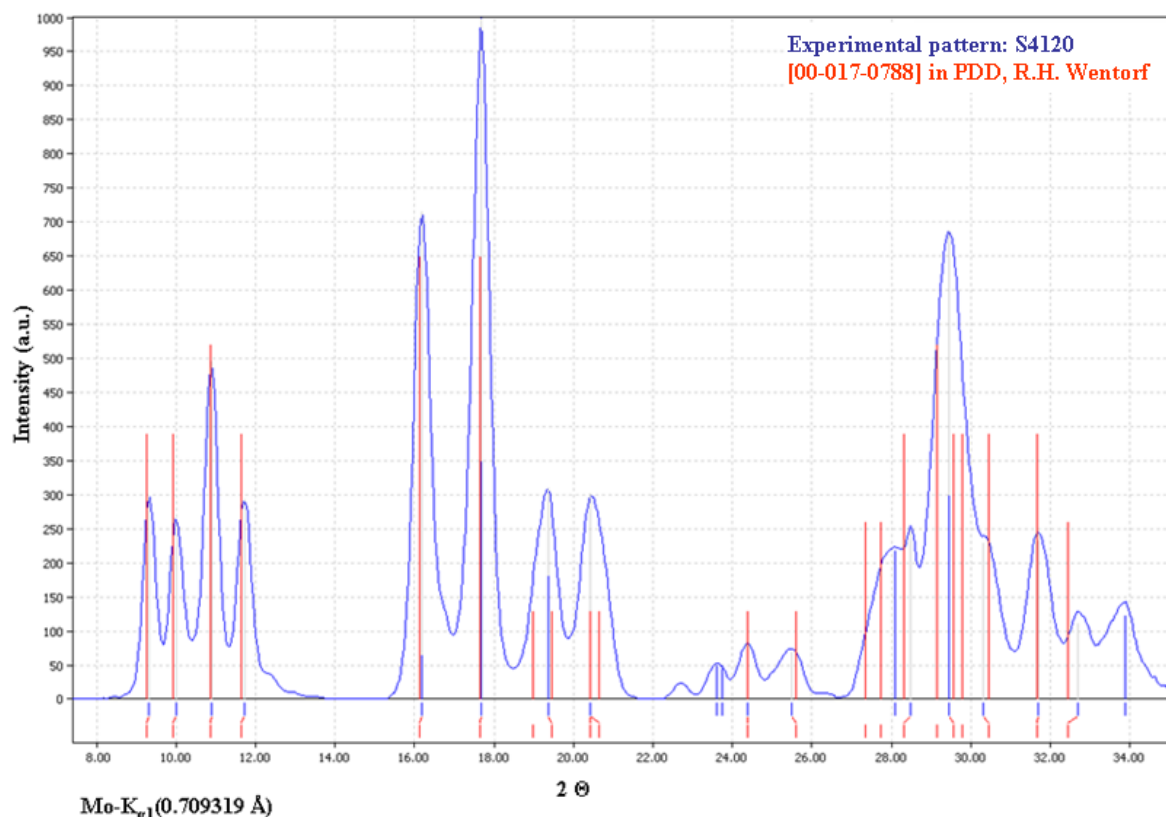


**Figure 2.1.1.** In-house X-ray diffraction patterns from the samples synthesized from various boron precursors.

Following discussion will concern studies of the samples synthesized from the most pure *β*-boron powder (99.995 %) available to us. Analyses of chemical composition of the sample were performed at BGI by different experimental techniques such as electron microprobe (EDX simultaneously with SEM, section 1.5.4.1, and WDX, section 1.5.4.2) and electron-energy loss spectroscopy. All measurements proved homogeneity of the synthesized sample and its purity from any contaminations other than the capsule material.

The *d*-spacings measured at BGI by selected area electron diffraction method implicated in TEM are in agreement with in-house X-ray diffraction data and also with

data published by R.H. Wentorf (Wentorf 1965) (Table 2.1.3). This indicates that the boron phase synthesized for the first time by R.H. Wentorf in reality is pure *HPHT* polymorph of elemental boron.



**Figure 2.1.2.** Comparison between X-ray diffraction patterns obtained from the sample S4120 (blue) synthesized at 14 GPa and 1500 °C (Table 2.1.2) and data obtained by R.H. Wentorf (in red) (Wentorf 1965).

**Table 2.1.3.** The *d*-spasings obtained by SAED and X-ray diffraction methods

| from TEM, Å | from X-ray diffraction, Å | (Wentorf 1965) |
|:-:|:-:|:-:|
| 5.6 | - | - |
| 5.1 | - | - |
| 4.3 | 4.36 | 4.4 |
| 4.1 | 4.07 | 4.1 |
| 3.8 | 3.74 | 3.75 |
| 3.3 | 3.47 | 3.5 |

## 2.2 Growth of single crystals of HPHT boron

Synthesis experiment conducted at 20 GPa and 1600 °C using $\beta$-boron loaded into Pt capsule (experiment Z612, Table 2.1.2) resulted in the formation of mixture of polycrystalline *HPHT* boron and single-crystals of this phase. The discussion of possible experimental options for growth of single crystals of *HPHT* boron needs special attention.

The systematic investigation of synthesis conditions for single crystal growth of *HPHT* boron phase were performed. Information on starting materials and experimental conditions is given in Table 2.2.1. The character feature of all performed synthesis experiments is that they were conducted with use of different metallic capsules (Cu, Au, Pt) and also with various precursors, mixture of $\beta$-boron and metallic powders of Pt or Cu.

**Table 2.2.1.** Summary of synthesis experiments of single crystal growth of HPHT boron phase.

| Experiment | Starting material | Conditions | | | |
|---|---|---|---|---|---|
| | | Capsule material | $T$ (°C) | $P$ (GPa) | Heating time (min) |
| S4439 | 95 at.% $\beta$-B + 5 at.% Cu | Au | 1500 | 12 | 7 |
| S4409 | 90 at.% $\beta$-B + 10 at.% Cu | Au | 1500 | 12 | 6 |
| S4442 | 85 at.% $\beta$-B + 15 at.% Cu | Au | 1700 | 12 | 2 |
| S4445 | 80 at.% $\beta$-B + 20 at.% Cu | Au | 1500 | 12 | 3 |
| S4457 | $\beta$-B | Cu | 1250 | 12 | 3 |
| S4390 | 98.5 at.% $\beta$-B + 1.5 at.% Pt | Au | 1500 | 12 | 2 |
| S4490 | 95 at.% $\beta$-B + 5 at.% Pt | Au | 1500 | 12 | 3 |
| S4486 | 90 at.% $\beta$-B + 10 at.% Pt | Au | 1500 | 12 | 3 |
| S4480 | 85 at.% $\beta$-B + 15 at.% Pt | Au | 1500 | 12 | 3-4 |
| S4400 | 80 at.% $\beta$-B + 20 at.% Pt | Au | 1500 | 12 | 6 |
| Z612 | $\beta$-B | Pt | 1600 | 20 | 5 |
| Z657 | $\beta$-B | Pt | 1900 | 14 | - |
| S4477 | $\beta$-B | Au | 1500 | 12 | 4 |
| S4492 | $\beta$-B | Au | 1800 | 12 | - |

All experiments indicated that crystals of *HPHT* boron phase were formed from the boron-metal solution during cooling. The maximal length of grown HPHT crystals achieved ~100 µm (in experiment S4492, Table 2.2.1). The size of crystals of *HPHT* phase does not depend on size of pressure chamber and duration of heating, but on amount of molten material, i.e. amount of solution of molten metallic flux and boron.

*HPHT* boron crystals predominantly grow in the inner part of the metallic capsule

where the area of surface of *β*-boron granules attached to the metallic capsule is maximal. In the case of use of as precursors the mixtures of *β*-boron with metallic additives (loaded into Au capsule) or loading of pure *β*-boron into Pt or Cu capsules the formation of additional (to HPHT boron) metal-borides phases as well as compounds of Au with corresponding metals from starting materials is inevitable. However, in experiment S4477 (Table 2.2.1), where *β*-boron granules were loaded into Au capsule, the product of the synthesis was free from any borides. The rest of non-molten *β*-boron also transformed into *HPHT* phase but due to recrystallization.



40x7x5 µm

**Figure 2.2.1.** Single crystal of *HPHT* boron phase synthesized at 20 GPa and 1600 °C in Pt capsule (experiment Z612, Table 2.1.2).

## 2.3  Determination of the structure of HPHT boron

In transmitted light thin sections of the synthesized polycrystalline boron samples are transparent with characteristic deep red color (Figure 2.3.1 a). Upon rotations through 90 degree in transmitted polarized light some nontransparent grains turn transparent indicating changing of polarization plane. Existence of different polarization planes is also confirmed by observations in reflected light (Figure 2.3.1 b) where differently colored grains observed. Based on optical observations in reflected and transmitted lights the symmetry of this *HPHT* boron phase was concluded to be not higher than orthorhombic.

Despite that boron is a weak scatterer, the in house collection of the X-ray powder diffraction data from the *HPHT* boron of acceptable quality could be acquired. X-ray data collection, which require intense radiation source, was carried out at of European synchrotron Radiation facility (ESRF, Grenoble, France) at Swiss-Norwegian Beam Lines (SNBL). Spectra of the polycrystalline sample of *HPHT* boron were collected

using monochromatic beam of 0.7 Å and MAR 345 detector. The description of structure determination of *HPHT* boron polymorph from single-crystal X-ray diffraction experiment is explained in section 1.6.2.1. The indexing of the difractogram of this new boron polymorph was turned out by using CMPR software in framework of orthorhombic symmetry as was suggested by optical analysis. Defined lattice parameters together with intensities were used for structure solution performed by Endeavour © software. Finally structure of *HPHT* boron polymorph was refined from powder diffraction data using GSAS program.
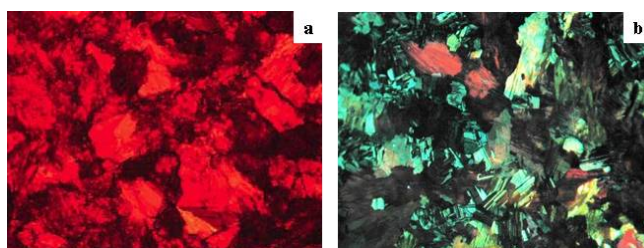


**Figure 2.3.1.** Section of ~10 μm of the *HPHT* boron phase (S4120, Table 2.1.2) in transmitted (a) and reflected (b) lights.
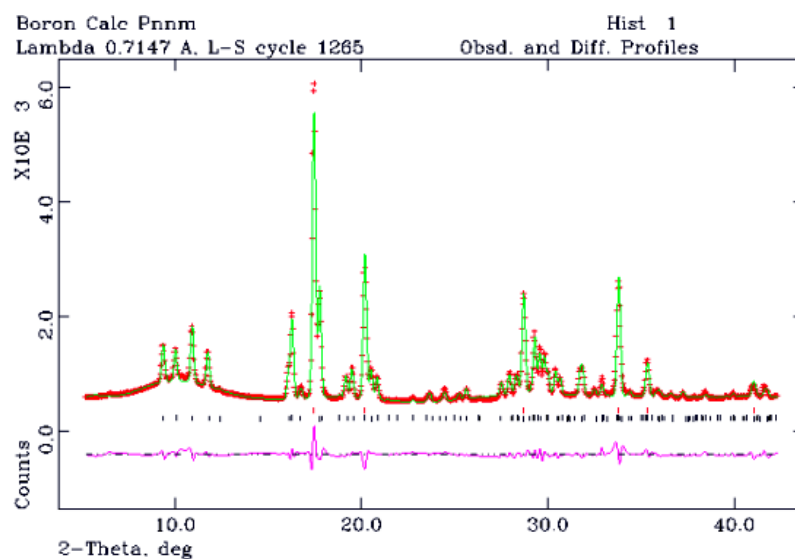


**Figure 2.3.2.** (a) Diffraction pattern of *HPHT* boron phase synthesized at 14 GPa and 1650 °C (experiment S4120, Table 2.1.2). The refinement of this phase was done by GSAS software. The result of the refinement is given in Table 2.3.1, see text below. Upper red ticks indicate the gold peaks (residuals of capsule material) and the lower black ticks mark the *HPHT* boron phase. Broad feature at ~10° is due to a glass capillary.

Independingly structure was solved from single crystal data. The result of the refinement from both powder and single crystal data as well as structural parameters obtained from first principles calculations performed via VASP code (Kresse and Furthmuller 1996) are given in Table 2.3.1.

**Table 2.3.1.** Structure of orthorhombic (space group *Pnnm*, Z=28) *HPHT* boron at ambient conditions, obtained from powder and single-crystal X-ray diffraction data and from *ab initio* calculations.

|  | **Powder Diffraction** | **Single-crystal Diffraction** | **Ab initio** |
|---|---|---|---|
| $a$, Å | 5.0563(4) | 5.0576(4) | 5.0434 |
| $b$, Å | 5.6126(5) | 5.6245(8) | 5.6121 |
| $c$, Å | 6.9710(7) | 6.9884(10) | 6.9248 |
| $V$, Å$^3$ | 197.83(4) | 198.80(4) | 196.0 |
| B1 | 0.162(2), 0.599(2), 0.794(9) | 0.1539(3), 0.5938(2), 0.7924(2) | 0.1528, 0.5925, 0.7908 |
| B2 | 0.645(2), 0.725(2), 0.5 | 0.6469(4), 0.7284(4), ½ | 0.6479, 0.7288, 0.5 |
| B3 | 0.335(2), 0.505(2), 0.0 | 0.3362(4), 0.5076(4), 0 | 0.3356, 0.5080, 0.0 |
| B4 | 0.837(2), 0.719(1), 0.870(1) | 0.8391(3), 0.7189(3), 0.8737(2) | 0.8393, 0.7189, 0.8743 |
| B5 | 0.669(2), 0.986(2), 0.0 | 0.6690(4), 0.9823(4), 0 | 0.6701, 0.9793, 0.0 |
| R-factors | wRp = 6.5 %, Rp = 5.5 % | $R_1$ = 3.73 %, w$R_2$ = 11.5 % | |

The structural analysis reveals that orthorhombic HPHT boron with P*nnm* (58) space group consists of 28 atoms per unit cell, thus, we called this boron allotrope B$_{28}$. The structure of B$_{28}$ phase in *bc* projection is shown in Figure 2.3.3. The structure of *HPHT*-B can be described as a tetragonal body-centered packing of columns. In this case, the icosahedra exhibit short exohedral contacts (1.659 Å), which results in chains parallel to the a-axis. Each chain is surrounded by four more chains, with the centers of the icosahedra being displaced from each other by half the diameter of an icosahedron. This arrangement results in each icosahedron forming eight more exohedral bonds which are significantly longer (1.826 Å). The boron atom in the B$_2$ dumbbells in the octahedral voids forms bonds with three boron atoms of the icosahedron: a short one (1.668 Å) and two longer ones (1.927 Å) directed towards an icosahedron of a neighboring chain (in the [010] direction). Thus, 16 bonds result for each icosahedron: two plus eight within the packing of columns (chain) and two plus four to the B$_2$ dumbbells.
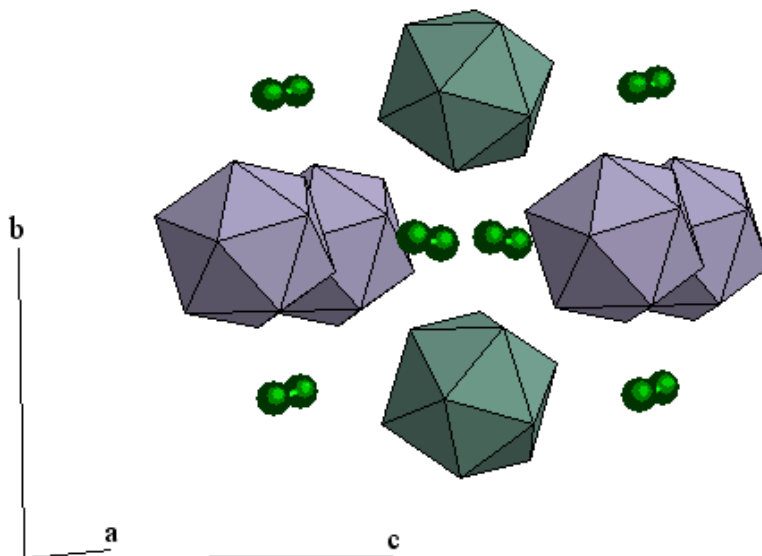
**Figure 2.3.3.** The structure of the orthorhombic $B_{28}$ phase shown in the *bc* projection. Boron atoms forming dumbbells are shown by larger green spheres.

The difference Fourier maps reveal the presence of residual electron density peaks between atoms linked the $B_2$ dumbbells and $B_{12}$ icosahedra as well as within the dumbbell (0.4 e/$Å^3$ and 0.53 e/$Å^3$ respectively). Similar to this, theoretical calculations suggested strong hybridization of considered bonds with the maximum value of electron localization function of 0.9 obtained in the dumbbells-icosahedra bonds. This leads to conclusion that type of bonding in the $B_{28}$ boron is strongly covalent explaining its physical properties.

## 2.4  $B_{28}$ stability field

Theoretical consideration of various boron structures ($\alpha$-, $\beta$-, $\alpha$-Ga type and $B_{28}$ structures of boron) conclude that $B_{28}$ phase is more stable than $\alpha$-B structure above ~20 GPa, and at 88 GPa it transforms into $\alpha$-Ga modification.

The in-situ high pressure X-ray diffraction experiments on polycrystalline samples of $B_{28}$ were conducted at ID09 beam line at ESRF (see section 1.6.2.1) with using of one- and double-side NIR laser heating. The transformation from $\beta$-B to $B_{28}$

phase was obtained at 8.5 GPa and ~1200 K (Figure 2.4.1), but with reheating the sample below 7 GPa it transforms back to structure of $\beta$-boron. The boundary between these two phases shifted with pressure increasing, and at 10 GPa the transition temperature could reach ~2200 K.
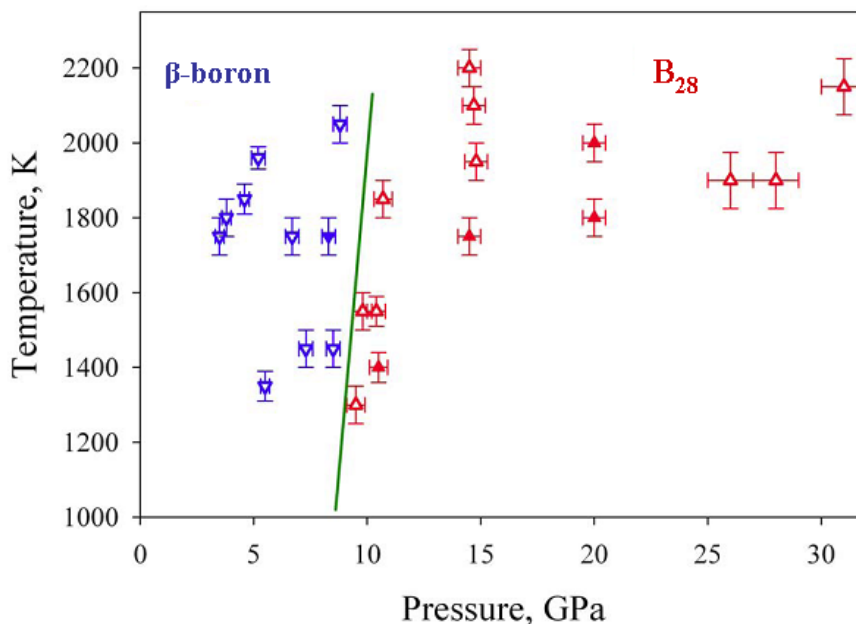


**Figure 2.4.1.** Phase relations between β-boron (blue inverse triangles) and $B_{28}$ phase (red triangles) based on the results of the multi-anvil quenched (solid symbols) and *in situ* DAC (open symbols) experiments. The line is a tentative phase boundary between β-boron and the orthorhombic phase.

## 2.5   Physical properties of $B_{28}$

### 2.5.1  Electrical properties

At ambient conditions resistivity of pure $B_{28}$ phase is in the order of $10^6$ Ohm cm. The conductivity of $B_{28}$ increases under higher temperatures like for semiconductors.

The activation energy was defined to be 1.9(2) eV. The value of band gap calculated from first principles is 1.7 eV. Absorption measurements in near-infrared and optical regions (see section 1.6.2.2.2) reveal the band gap of $B_{28}$ equal to 2.1 eV. Above

the absorption edge the optical spectra are too noisy and determination of type of band gap (direct/indirect) of $B_{28}$ can not be performed. However, theoretically the indirect band gap was predicted. Also, *ab*-initio calculations suggested the closure of band gap of $B_{28}$ with pressure increasing and, for example, at pressure of 23 GPa the energy band gap decreases by 5.88 %.

### 2.5.2  Compressibility and hardness of $B_{28}$

The highest density (2.54 g/cm$^3$) of $B_{28}$ phase among known boron modifications (2.29-2.35 g/cm$^3$ for *β*-B, and 2.46 g/cm$^3$ for *α*-B) and covalent type of bonding influence on compressibility and hardness of this material. From X-ray diffraction data collected on compression up to 30 GPa bulk modulus ($B_0$) and pressure derivative (*B'*) of $B_{28}$ (at fixed molar volume 197.44(2) Å$^3$) was determined to be 227(2) GPa and 2.2(2), respectively. *Ab*-initio simulations performed in framework of Perdew-Burke-Ernzerhof approximation to exchange-correlation energy give $B_0$=221.7(7) GPa and *B'*=3.6(3), $V_0$=195.97(6) Å$^3$.

Both experimental and theoretical observations show that the least compressible direction in $B_{28}$ structure is *a* axis along which there are shortest contacts between $B_{12}$ icosahedra and $B_2$ dumbbells.

The theoretical analysis of relative changing of interatomic distances in $B_{28}$ with pressure (Figure 2.5.2.1) shows that the bonds within the dumbbells and between atoms linked dumbbells and icosahedra are easier compressed. The average interatomic distances within the $B_{12}$ icosahedra are the largest, although, they found to be less compressible. The most incompressible bonds are those formed by atoms of nearest icosahedra. Possible explanation may be that internal stresses could be reduced by decreasing of $B_2$ dumbbell bonds, thus, comparable to them B-B bonds within the icosahedra become "less sensitive" to structure volume change.

Presence of additional atoms formed $B_2$ dumbbells, making $B_{28}$ structure compact, influence on hardness of the material. The Vikers micro-hardness of orthorhombic $B_{28}$ phase was determined to be 58(5) GPa that is two times higher than reported hardness for *β*-boron (25-30 GPa).
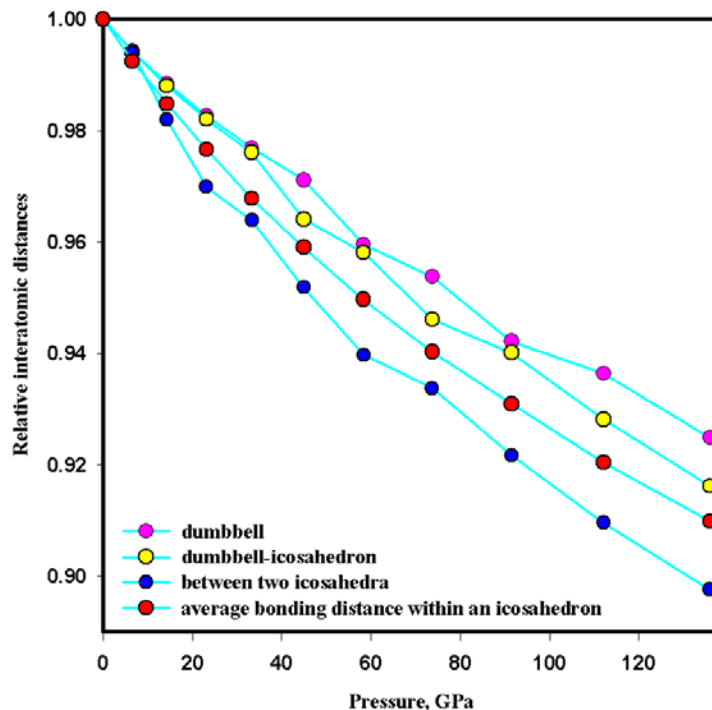
**Figure 2.5.2.1** Relative changing of interatomic distances with pressure obtained from *ab* initio calculations of $B_{28}$: bonds within the dumbbells (pink spheres), between atoms linked an icosahedron and a dumbbell (yellow spheres), between the nearest atoms of two icosahedra (blue spheres); and average distance within an icosahedron (red spheres).

### 2.5.3  Vibrational properties of $B_{28}$

Raman spectroscopic studies of the synthesized samples reveal that its vibrational properties differ from those of any known boron modification.The symmetry of vibrational modes can be defined based on group theory. In order to assign modes the polarized Raman experiments were carried out on single-crystals synthesized in experimental run Z612 (see Table 2.1.2). Crystals were polished and preoriented with respect to directions of main crystallographic axes.

Due to low intensities of some peaks or possibly their merging, unfortunately, not all of 42 Raman active modes were detected in our experiment. However, the majority of Raman peaks visible in our experiment were unambiguously attributed to a certain type of atomic movements by comparison with atomic vibrations known for $\alpha$-B and highly ordered pnictides (Figure 2.5.3.1). Thus, presented on Figure 2.5.3.1 $A_g$ (380 cm$^{-1}$) and

$B_{1g}$ (388 cm$^{-1}$) modes could be attributed to icosahedron-dumbbell and dumbbells vibrations, correspondingly. The mode appeared at 319 cm$^{-1}$ is believed to arise due to librational vibration of $B_{12}$ icosahedra.The modes obtained in the range between 507 cm$^{-1}$ and 1200 cm$^{-1}$ correspond most probably to inter- and intra-icosahedral vibrations.
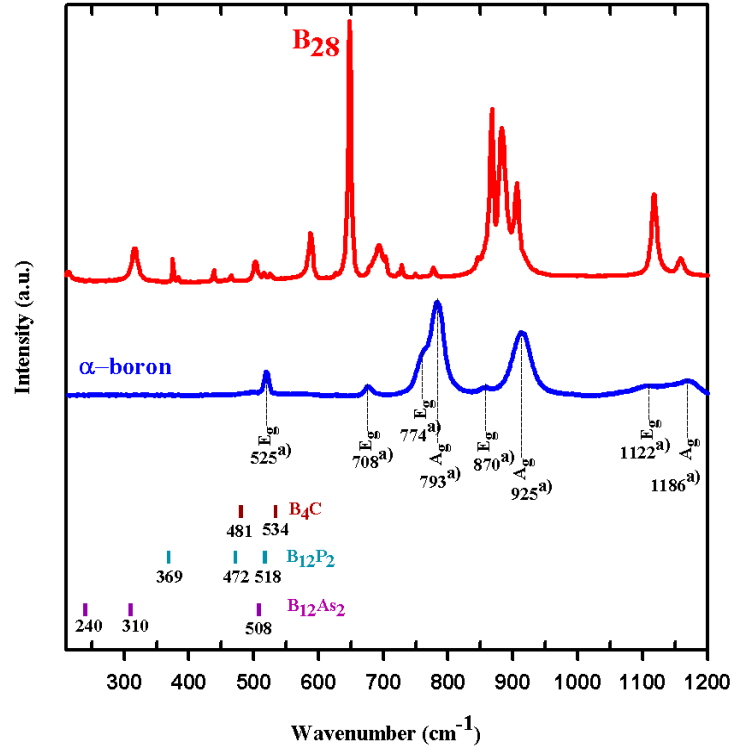


**Figure 2.5.3.1.** Comparison of the Raman spectra collected at ambient conditions of polycrystalline orthorhombicB$_{28}$ (red curves) with that of $\alpha$-boron (blue curve). The positions of low-frequency lines of boron-rich compounds (B$_4$C, B$_{12}$P$_2$ and B$_{12}$As$_2$) are shown as tick marks.

The high pressure behavior of Raman spectra of B$_{28}$ was studied on polycrystalline samples and can be interpreted in term of mode-Grueneisen parameter, defined as

$$\gamma_{\omega i} = \partial \ln \omega_i / \partial \ln V = -(B_0/\omega_i)\partial\omega_i/\partial P,$$

where $\omega_i$ is the phonon frequency, $B_0$ is the bulk modulus (227 GPa at ambient conditions), $V$ is the molar volume and $P$ is the pressure.

The pressure dependence of modes is shown in Figure 2.5.3.2. The observed Raman modes (Table 2.5.3.1) can be classified into three groups. To a first group with high Grueneisen parameter of 2.8 the $B_{2g}$ mode at 319(3) cm$^{-1}$ was atributed. This mode is the most sensitive to volume change and does not strengthen interatomic contacts. To the second group almost immovable ($\gamma$=0.03-0.2) and narrow bands obtained in frequency range of 380-470 cm$^{-1}$ belong. These modes appear because of rotations of $B_{12}$ icosahedra or icosahedra and $B_2$ dumbbells around *b* and *c* axis involve changes in distances of shortest B-B contacts between icosahedron and/or icosahedron-dumbbell. Modes observed between 507 cm$^{-1}$ and 1200 cm$^{-1}$ with Grueneisen parameter variations of 0.42 - 1.05 attributed to a third group.
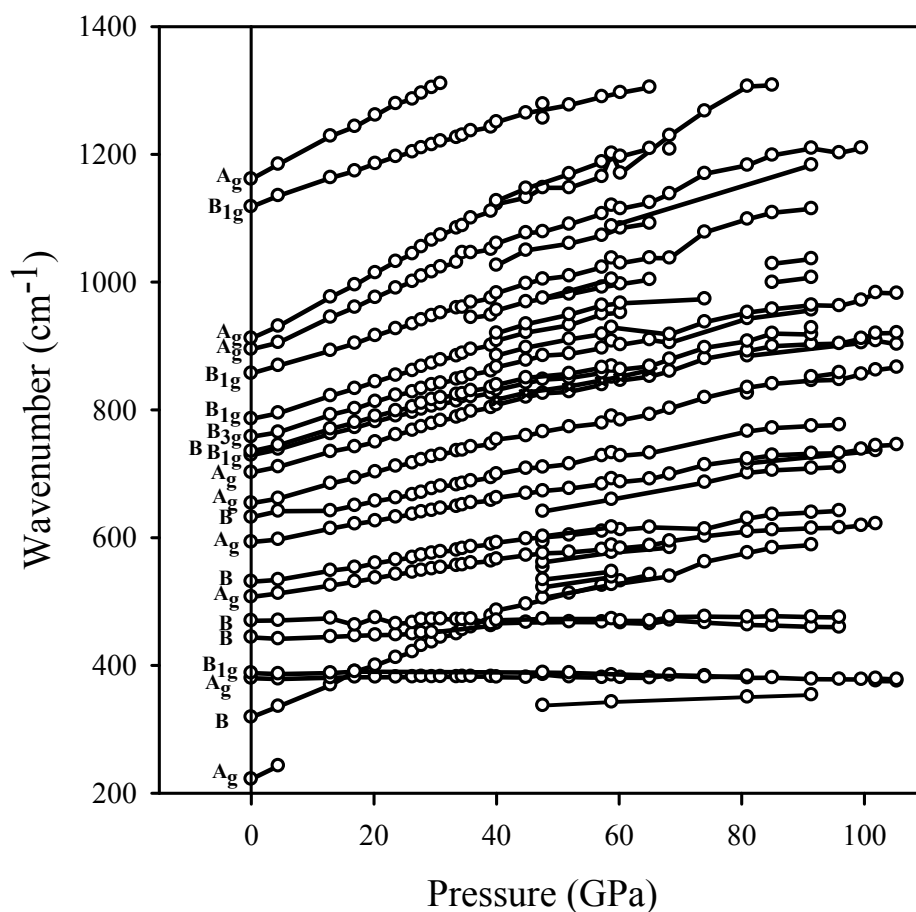


**Figure 2.5.3.2.** High pressure behavior of Raman modes.

Under pressure the majority of Raman modes are monotonically shifted to a higher wavenumbers. At pressures higher than 40(1) GPa an inflection in modes behaviour (Figure 2.5.3.2) is observed. Under further compression to ~ 40-45 GPa several modes split (although the total number of registered modes was always below the number of 42 allowed modes in orthorhombic $B_{28}$). Modes at low wavenumber region of the spectra, $A_g$ at 380 cm$^{-1}$ and $B_{2g}$ or $B_{3g}$ at 470 cm$^{-1}$, become soft with Grueneisen parameters of ~-0.03.

**Table 2.5.3.1.** Assignment of experimental and theoretical phonon frequencies at ambient conditions with experimentally determined mode-Grueneisen parameters ($\gamma_{exp}$).

| Experiment | | | | Theory | |
|---|---|---|---|---|---|
| $\omega_{exp}$(cm$^{-1}$) | Assignment | $\gamma_{exp}$ below 39 GPa | $\gamma_{exp}$ above 39 GPa | $\omega_{th}$(cm$^{-1}$) | Assignment |
| 217(2) | $B_{2g}, B_{3g}$ | | | | |
| 222(2) | $A_g$ | | | | |
| 319(3) | $B_{2g}, B_{3g}$* | 2.76 | 1.04 | 303 | $B_{2g}$ |
| 380(1) | $A_g$ | 0.07 | -0.03 | 387 | $A_g$ |
| 388(2) | $B_{1g}$ | 0.17 | | 389 | $B_{3g}$ |
| 440(2) | $B_{2g}, B_{3g}$ | 0.20 | -0.02 | 454 | $B_{3g}$ |
| 460(2) | $B_{1g}$* | | | 464/475 | $B_{3g}/B_{1g}$ |
| 470(2) | $B_{2g}, B_{3g}$ | 0.03 | | 464/475 | $B_{3g}/B_{1g}$ |
| 507(2) | $A_g$ | 0.65 | 0.34 | 536 | $A_g$ |
| 531(2) | $B_{2g}, B_{3g}$ | 0.68 | | 537 | $B_{2g}$ |
| 593(3) | $A_g$ | 0.67 | 0.41 | 611 | $A_g$ |
| 632(2) | $B_{2g}, B_{3g}$ | 0.53 | 0.42 | 585/575 | $B_{2g}/B_{3g}$ |
| 654(2) | $A_g$ | 0.84 | 0.47 | 687 | $A_g$ |
| 686(3) | $B_{1g}, B_{2g}, B_{3g}$* | | | 658 | $B_{1g}$ |
| 702(3) | $A_g$* | 0.85 | 0.50 | 732 | $A_g$ |
| 712(3) | $B_{2g}, B_{3g}$ | | | 714/719 | $B_{3g}/B_{2g}$ |
| 729(2) | $B_{1g}$ | 0.78 | 0.40 | 726 | $B_{1g}$ |
| 735(2) | $B_{1g}, B_{2g}, B_{3g}$* | 0.79 | 0.42 | 735 | $B_{2g}$ |
| 758(2) | $B_{3g}$ | 0.82 | 0.45 | 765 | $B_{3g}$ |
| 786(2) | $B_{1g}$ | 0.87 | 0.54 | 781,784 | $B_{1g}, B_{1g}$ |
| 857(3) | $B_{1g}$ | 0.81 | 0.52 | 862 | $B_{1g}$ |
| 878(2) | $B_{1g}, B_{3g}$* | | | 884 | $B_{3g}$ |
| 895(2) | $A_g$ | 1.05 | 0.55 | 887 | $A_g$ |
| 912(2) | $A_g$ | 1.26 | 0.66 | 920 | $A_g$ |
| 929(2) | $A_g$ | | | 970? | $A_g$ |
| 952(2) | $B_{2g}, B_{3g}$* | | | 959 | $B_{2g}$ |
| 1095(2) | $B_{1g}, B_{2g}, B_{3g}$* | | | | |
| 1118(2) | $B_{1g}$ | 0.98 | 0.40 | 1118 | $B_{1g}$ |
| 1138(2) | $B_{1g}$ | | | 1138 | $B_{1g}$ |
| 1161(2) | $A_g$ | 0.42 | | 1189 | $A_g$ |
| 1189(2) | $A_g$ | | | 1194 | $A_g$ |
| 1218(2) | $A_g$ | | | | |

*Peaks which are visible also in forbidden scattering geometries.

Laser annealing at 1500-1800 K at pressures above 40 GPa does not affect Raman spectra and changes are fully reversible on decompression suggesting that orthorhombic $B_{28}$ may undergo phase transition at high pressures.

# 3    LIST OF MANUSCRIPTS AND STATEMENT OF AUTHOR'S CONTRIBUTION

**[1].** E. Yu. Zarechnaya, L. Dubrovinsky, N. Dubrovinskaia, N. Miyajima, Y. Filinchuk, D. Chernyshov, and V. Dmitriev. Synthesis of an orthorhombic high pressure boron phase. *Sci. Technol. Adv. Mater, 9:044209-044212, 2008.*

Samples of a polycrystalline high pressure boron phase $B_{28}$ were synthesized by E. Yu. Zarechnaya (E.Z.) and N. Dubrovinskaia (N.D.). Raman spectroscopy and in-house X-ray diffraction experiments were conducted by E.Z. and analyzed by E.Z., L. Dubrovinsky (L.D.), and N.D. Synchrotron powder X-ray diffraction was performed by Y. Filinchuk (Y.F.), D. Chernyshov (D.C.), and V. Dmitriev (V.D.). Structure solution from synchrotron powder diffraction data was realized by E.Z., L.D., and N.D. N. Miyajima (N.M.) performed HRTEM analysis. E.Z. did final interpretation of the results and wrote the manuscript.

**[2].** E. Yu. Zarechnaya, L. Dubrovinsky, N. Dubrovinskaia, Y. Filinchuk, D. Chernyshov, V. Dmitriev, N. Miyajima, A. El Goresy, H. F. Braun, S. Van Smaalen, I. Kantor, A. Kantor, V. Prakapenka, M. Hanfland, A. S. Mikhaylushkin, I. A. Abrikosov, S. I. Simak. Superhard semiconducting optically transparent high pressure phase of boron. *Phys. Rev. Lett., 102: 185501-185504, 2009.*

Experiments on synthesis of the HPHT phase of boron in form of polycrystalline material as well as single crystals were performed by E.Z. and N.D. SEM and microprobe analysis were performed by E.Z. and L.D. Materials characterization using Raman spectroscopy and in-house X-ray diffraction was done by E.Z. Data analysis was performed by E.Z., L.D. and N.D. TEM analysis and EELS were performed by N.M. Optical observations of polycrystalline sample of orthorhombic boron in transmitted and reflected light and suggestion on symmetry of the material were done by A. El Goresy and E.Z. DACs for in-situ HP experiments were prepared by E.Z. In-situ HP X-ray diffraction experiments at European Synchrotron Radiation Facility (ESRF, Grenoble, France, ID-09) and at

Argonne Advanced Photon Source (APS, Chicago, USA, IDD-13) for the determination of the stability range and compressibility of HPHT boron phase were performed by E.Z., L.D., N.D, M.Hanfland, I. Kantor, A. Kantor, and V. Prakapenka. Single crystal X-ray diffraction at ambient pressure were performed at ESRF (SNBL) by Y.F., D.C., and V.D. Maximum entropy method was applied to the single crystal X-ray diffraction data by S. Van Smaalen. Characterisation of electrical and mechanical properties of $B_{28}$ was carried out by E.Z., N.D., L.D., and H. Braun. *Ab initio* calculations were performed by E.Z., A. Mikhaylushkin (A.M.), I.A. Abrikosov (I.A), and S.I. Simak (S.I.). E.Z. did final interpretation of the results and wrote the manuscript.

**[3].** E. Yu. Zarechnaya, N. Dubrovinskaia, and L. Dubrovinsky. Polarized Raman spectroscopy of high-pressure orthorhombic boron phase. *High Pressure Research 29:530-535, 2009.*

Single crystals for polarized Raman measurements were selected and preliminary characterized using SEM and Raman spectroscopy by E.Z. Polarized Raman measurements on these initially pre-oriented crystals was performed by E.Z. and L.D. Analysis of the results and the mode assignment was performed by E.Z., L.D. and N.D. E.Z. did final interpretation of the experiental observations and wrote the manuscript.

**[4].** E. Yu. Zarechnaya, N. Dubrovinskaia, L. Dubrovinsky, Y. Filinchuk, D. Chernyshov, V. Dmitriev. Growth of single crystals of $B_{28}$ at high pressure and high temperatures. Journal of Crystal Growth (in press).

E.Z. propose idea of systematic investigation of experimental conditions and planning along with N.D. and L.D. high pressure high temperature experiments on synthesis of single crystals of $B_{28}$ phase. E.Z. did synthesis experiments using a multi anvil apparatus, obtained *in-house* X-ray diffraction and performed the phase analysis of the synthesis products. Microprobe and SEM of the synthesis products was performed by E.Z. and L.D. The quality of grown crystals of $B_{28}$ phase was checked at ESRF (SNBL) by Y.F,

D.C., and V.D. E.Z. The analysis of the experimental results and their interpretation was undertaken by E.Z. The manuscript was written by E.Z.

**[5].** E. Yu. Zarechnaya, N. Dubrovinskaia, R. Caracas, M. Merlini, M. Hanfland, Y. Filinchuk, D. Chernyshov, V. Dmitriev, L. Dubrovinsky. Pressure-induced isostructural phase transformation in $\gamma$-$B_{28}$. *Nature (submitted).*

Single crystals of $\gamma$-$B_{28}$ were synthesized by E.Z. and N.D. High-pressure Raman spectroscopy experiments were conducted and analyzed by E.Z., L.D., N.D., and V.D. Single crystal high-pressure X-ray diffraction experiments were conducted by E.Z., N.D., L.D., M. Merlini (M.M.), and M.H. Structural refinement was performed by M.M.; Y.F. and D.C. helped in analysis of X-ray diffraction data. R. Caracas performed *ab initio* calculations of Raman and IR spectra. E.Z., L.D. and N.D. interpreted results. E.Z. wrote the manuscript.

# 4   MANUSCRIPTS

## 4.1   Synthesis of an orthorhombic high pressure boron phase

Evgeniya Yu Zarechnaya[1], Leonid Dubrovinsky[1], Natalia Dubrovinskaia[2], Nobuyoshi Miyajima[1], Yaroslav Filinchuk[3], Dmitry Chernyshov[3] and Vladimir Dmitriev[3]

*[1] Bayerisches Geoinstitut, Universität Bayreuth, 95440 Bayreuth, Germany; [2] Institute of Earth Sciences, Universität Heidelberg, Im Neuenheimer Feld 236, 69120 Heidelberg, Germany; [3] Swiss Norwegian Beam lines at ESRF, 38043 Gernoble, France*

### 4.1.1. Abstract

The densest boron phase ($2.52$ g cm$^{-3}$) was produced as a result of the synthesis under pressures above 9 GPa and temperatures up to ~1800 °C. The x-ray powder diffraction pattern and the Raman spectra of the new material do not correspond to those of any known boron phases. A new high-pressure high-temperature boron phase was defined to have an orthorhombic symmetry (*Pnnm* (No. 58)) and 28 atoms per unit cell.

### 4.1.2. Introduction

Boron is one of the nonmetal elements which has been widely studied due to its complex polymorphism. Boron's three valence electrons are too localized to make it metallic and insufficient in number to form a simple covalent structure. As a result, boron atoms form $B_{12}$ icosahedra linked together in a variety of ways. Only $\alpha$- (rhombohedral, within a 12-atom unit cell) and $\beta$- (high-temperature form, rhombohedral, structure is not fully understood and consists of 105 or 108 atoms in the unit cell) crystalline modifications of elemental boron are currently established as pure boron forms [1–3].

Elemental boron can be prepared as an amorphous material of different purity by various techniques [4, 5]. It was proposed that $\beta$-boron is stable up 30 GPa and 3500 K, and at higher temperatures and pressures, a phase transition to the tetragonal 'T-192' structure occurs [3, 6]. The existence of 'tetragonal boron T-50' as a true modification of pure elemental boron or as boron-rich nitride or carbide has been a subject of controversy [7, 8]. On compression up to 100 GPa of a single crystal at room temperature the amorphization of $\beta$-boron was observed [9]. Resistivity measurements demonstrate metallization of boron and occurrence of superconducting state at about 160 GPa [10]. However, the structural model of metallic boron is unknown. Thus, the behavior of boron at high pressure remains poorly understood. Here, we report a new pure boron modification synthesized at pressures up to 20 GPa and temperatures up to ~1800 °C using a multianvil apparatus.

## 4.1.3. Experiments

As starting materials for synthesis we used $\beta$-boron (Sigma-Aldrich Inc, 99.95 and 99.7% purity; Goodfellow Inc, 99.6% purity; Chempur Inc, 99.995% purity), $\alpha$-boron (Inorganic Chemistry Institute, Kiev, Ukraine, 98% purity), and amorphous boron (Chempur Inc, 95–97% purity).

High-pressure high-temperature (HPHT) experiments were carried out using 6–8-type multianvil Sumitomo 1200-ton and Zwick 5000-ton presses. Starting materials were loaded into BN, Au, Pt or In capsules of ~2.6mm (~2 mm) in diameter and of ~2.7mm (~3.5 mm) in height. The temperature reached 1500 °C in experiments with Au capsules and 1800 °C for BN capsules. The cell assembly included truncated WC cubes, MgO+ 5wt.%$Cr_2O_3$ octahedra and $LaCrO_3$ heaters. The pressure and temperature uncertainties were estimated as 1 GPa and 50 °C, respectively. After gradual compression of the samples to desired pressures the temperature was increased stepwise with a speed of about 200 °C/min$^{-1}$ to the desired value. Duration of heating was up to 10 min in different runs. The temperature quenching was done by switching off the power. The chemical composition, structure and texture of the quenched samples were studied with the scanning electron microscopy (SEM, LEO-1530) and electron energy loss

spectroscopy (EELS, Gatan 666 PEELS in a Philips CM20 FEG analytical transmission electron microscope, operated at 200 kV).

Raman scattering was excited with a He–Ne laser (632.8 nm, power 100 mW) and detected with a LabRam spectrometer at resolution of 2 $cm^{-1}$.

The in-house x-ray powder diffraction studies were conducted using a high-brilliance diffractometer ($MoK_\alpha$ radiation) equipped with the Osmic focusing x-ray optics and the Bruker Apex CCD detector. At SNBL (ESRF, France) powder x-ray data were collected using a monochromatic beam (0.7 Å) and a MAR345 detector.

## 4.1.4. Results and discussion

Experiments in large-volume presses at pressures above 10 GPa and temperatures above 1500 °C starting from boron precursors with purity higher than 99.7% result in formation of an optically homogeneous reddish material. Energy dispersive x-ray spectroscopy (not shown) and EELS reveal that the samples synthesized from crystalline $\beta$-boron powders are not contaminated by any impurity other than the capsule material (Figure 4.1.4.1). SEM images of the sample surfaces in backscattered electrons indicate homogeneity of the synthesized HPHT samples. High resolution transmission electron microscopy (HRTEM) images can be interpreted in terms of a combination of boron spheres (Figure 4.1.4.1). The diameter of the spheres (3.29–3.68 Å) is comparable with that of the circumscribed circle around the $B_{12}$ icosahedron (3.34 Å, see Figure 4.1.4.3). The x-ray powder diffraction pattern (Figure 4.1.4.2(a)) and the Raman spectrum (Figure 4.1.4.2(b)) of the new material are drastically different from those of any established boron phase. Nevertheless, the powder diffraction pattern of the phase we synthesized closely resembles that reported by Wentorf [11]. The structure of the material reported in [11] was unknown, and we did not find any further confirmation of its existence in the literature. For some time, the data from Wentorf's paper [11] were included into the Powder Diffraction Files (#00-017-0788), but later the file was deleted and no reason was provided. Positions of some lines reported by Wentorf [11] could be explained as those from boron suboxides or/and carbides and it was probably a motivation for discarding this material as pure boron. However, we establish here that the HPHT phase is pure

boron and it can be synthesized from various precursors, in different environment, and at different conditions (Table 4.1.4.1). Thus, we confirm the existence of the pure boron phase first reported by Wentorf [11].

(a)
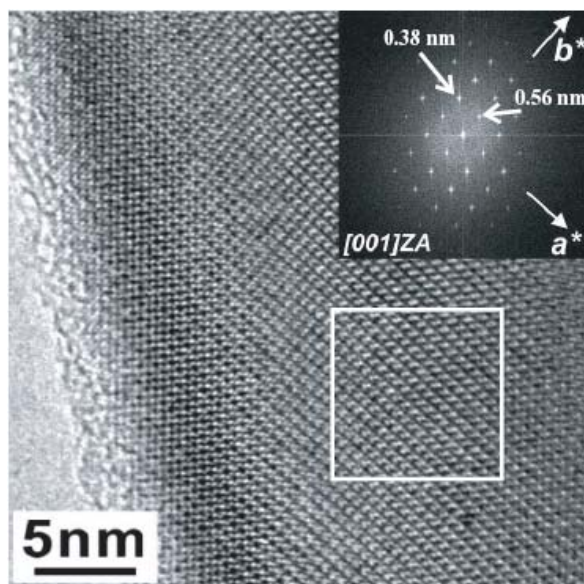


(b)
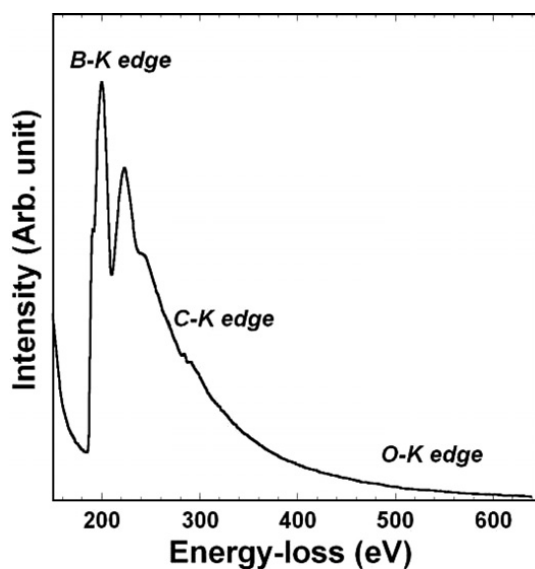


**Figure 4.1.4.1.** (a) High-resolution TEM image of the orthorhombic high-pressure high-temperature boron phase (sample S4120, see Table 4.1.4.1.). Inset is a fast Fourier transform (FFT) pattern from the area marked by the white rectangle. ZA refers to zone axis. (b) A core-loss EELS spectrum, confirming the purity of the boron phase. The spectrum has been gain-normalized and deconvoluted using the low-loss spectrum.

(a)
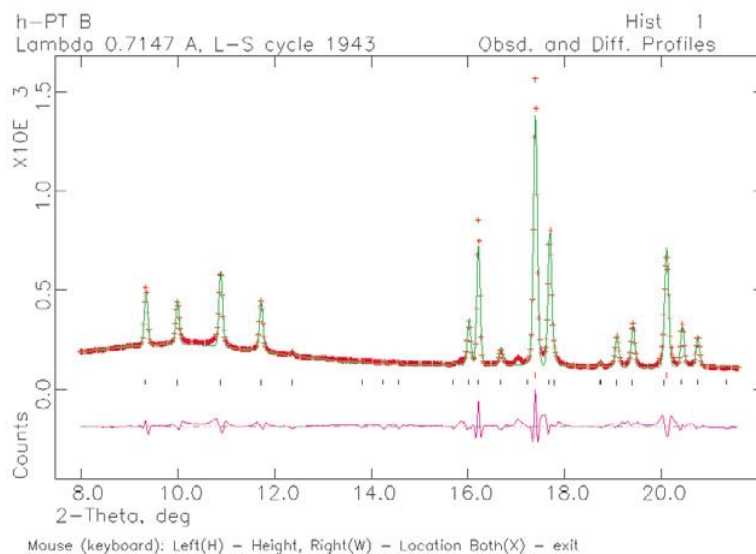


(b)
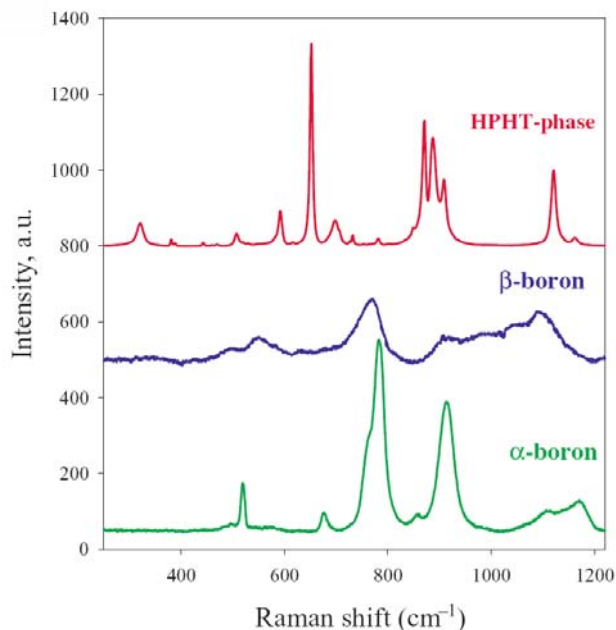


**Figure 4.1.4.2.** (a) Diffraction pattern of the boron phase synthesized at 14 GPa and 1650 °C (S4120 as denoted in Table 4.1.4.1). It was refined using the GSAS package (18) ($\lambda$ = 0.7147 Å, wRp = 6.5%, Rp = 5.5%; space group *Pnnm*, $a$ = 5.0563(4) Å, $b$ = 5.6126(5) Å, $c$ = 6.9710(7) Å, B1 (0.152(2), 0.599(2), 0.794(9)), B2 (0.645(2), 0.725(2), 0.5), B3 (0.335(2), 0.505(2), 0.0), B4 (0.837(2), 0.719(1), 0.870(1)), B5 (0.669(2), 0.986(2), 0.0). Upper red ticks indicate the gold peaks (residuals of capsule material) and the lower black ticks mark the HPHT boron phase. Broad feature at ~10° is due to a glass capillary. (b) Raman spectra of the boron phase (sample S4120 of Table 4.1.4.1) synthesized at 14 GPa and 1650 °C in comparison with the spectra of the known $\alpha$ and $\beta$ phases.

**Table 4.1.4.1.** Summary of experiments on synthesis of the orthorhombic HPHT boron phase.

| Experiment | Starting material | Conditions | | | | Characterization |
|---|---|---|---|---|---|---|
| | | Capsule material | Temperature (°C) | Pressure (GPa) | Heating time (min) | |
| S4096 | $\beta$-boron | BN | 1800 | 14 | 3 | Orthorhombic HPHT phase, pure |
| S4120 | $\beta$-boron | Au | 1650 | 14 | 3 | Orthorhombic HPHT phase, pure |
| Z612 | $\beta$-boron | Pt | 1600 | 20 | 5 | Orthorhombic HPHT phase+PtB |
| Z628 | $\beta$-boron | In | 1600 | 20 | 5 | Orthorhombic HPHT phase, pure |
| S4285 | $\beta$-boron, isotope $^{10}$B | Au | 1500 | 14 | 7 | Orthorhombic HPHT phase, pure |
| S4141 | Amorphous boron | Au | 1500 | 14 | 5 | Orthorhombic HPHT phase+boron oxides+unknown phases |
| S4202 | $\alpha$-boron | Au | 1650 | 14 | 6 | Orthorhombic HPHT phase+unknown phase |
| S4228 | $\beta$-boron, isotope $^{11}$B | Au | 1650 | 14 | 4 | Orthorhombic HPHT phase, pure |

By indexing the powder x-ray diffraction data and using Endeavour$^{©}$ software, the structure of quenched samples was solved in the framework of an orthorhombic unit cell ($a$ = 5.0563, $b$ = 5.6126(5) and $c$ = 6.9710(7) Å, and $V$ = 197.83(3) Å$^3$). The suggested structure of the HPHT boron with a space group Pnnm (No. 58) contains 28 atoms in a unit cell. The *bc* projection (Figure 4.1.4.3) shows that the structure is built of B$_{12}$ icosahedra linked into a three-dimensional network. Nearly rectangular channels running along the *a*-axis are filled with boron chains, composed of B$_2$ dumbbells and aligned almost parallel to the a-axis. Replacing the geometrical centers of icosahedra by one sort of atoms and the middle of dumbbells by another sort of atoms leads to an *Immm* structure, which is a distorted derivative of the NaCl structure type.

In the *Pnnm* structure, the centre of the B$_2$ dumbbell is at $\frac{1}{2}00$, and of B$_{12}$—at $\frac{1}{2}0\frac{1}{2}$. The distances B–B within the B$_{12}$ icosahedron (1.75–1.95 Å) are slightly longer than those within the dumbbell (1.73 Å). The shortest distances in the structure are those between atoms linking (1) the two icosahedra—1.64 Å, (2) the icosahedron and the dumbbell—1.63 Å, and (3) the two boron atoms within a dumbbell—1.73 Å. Chemical bonds in the B$_2$ dumbbell and between an icosahedron and a dumbbell are strongly covalent, as evident from the presence of residual electron density peaks (0.53 and 0.40 eÅ$^{-3}$ respectively) in the difference Fourier maps.
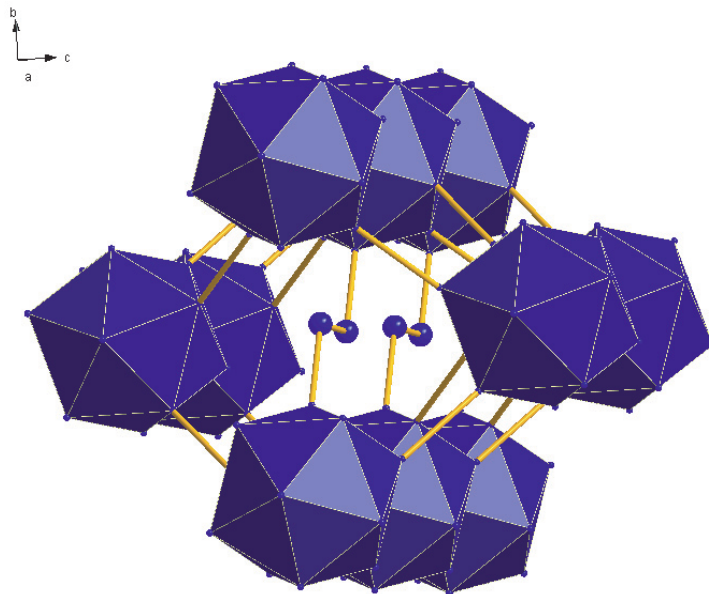
**Figure 4.1.4.3.** The structure of the high-pressure high-temperature orthorhombic boron phase shown in the *bc* projection. Boron atoms forming dumbbells are shown by larger blue spheres.

## 4.1.5. Conclusions

We demonstrate that the boron phase first reported by Wentorf [11] is pure boron and can be synthesized directly form different precursors at pressures above 9 GPa. Our study shows that this phase has a new orthorhombic structure consisting of $B_{12}$ icosahedra and boron chains. The orthorhombic high-pressure high-temperature boron phase has the density of 2.52 g $cm^{-3}$ which is the highest among any other known boron modifications.

## References

[1] Will G and Kiefer B 2001 *Z. Anorg. Allg. Chem.* **627** 2100

[2] Will G and Ploog K 1974 *Nature* **251** 406

[3] Brazhkin V V, Taniguchi T, Akaishi M and Popova S V 2004 *J. Mater. Res.* **19** 1643

[4] Katada K 1966 *Japan J. Appl. Phys.* **5** 582

[5] Gillespie J S 1988 *J. Am. Chem. Soc.* **88** 2423

[6] Ma Y, Prewitt Ch T, Zou G, Ho-kwang M and Hemley R J 2003 *Phys. Rev.* B **67** 174116

[7] Naslain R 1977 *Boron and Refractory Borides* ed V I Matkovich (Berlin: Springer)

[8] Hoard J L, Sullenger D B, Kennard C H L and Highes R E 1970 *J. Solid State Chem.* **1** 268

[9] Sanz D N, Loubeyre P and Mezouar M 2002 *Phys. Rev. Lett.* **89** 245501

[10] Eremets M I, Struzhkin V V, Ho-kwang M and Hemley R J 2001 *Science* **293** 272

[11] Wentorf R H 1965 *Science* **147** 49

## 4.2   Superhard Semiconducting Optically Transparent High Pressure Phase of Boron

E. Yu. Zarechnaya[1], L. Dubrovinsky[1], N. Dubrovinskaia[2,3], Y. Filinchuk[4], D. Chernyshov[4], V. Dmitriev[4], N. Miyajima[1], A. El Goresy[1], H. F. Braun[5], S. Van Smaalen[3], I. Kantor[6], A. Kantor[6], V. Prakapenka[6], M. Hanfland[7], A. S. Mikhaylushkin[8], I. A. Abrikosov[8], S. I. Simak[8]

*[1]Bayerisches Geoinstitut, Universität Bayreuth, 95440 Bayreuth, Germany; [2]Mineralphysik, Institut für Geowissenschaften, Universität Heidelberg, 69120 Heidelberg, Germany; [3]Lehrstuhl für Kristallographie, Physikalisches Institut, Universität Bayreuth, 95440 Bayreuth, Germany; [4]Swiss Norwegian Beam lines at ESRF, 38043 Gernoble, France; [5]Experimentalphysik V, Physikalisches Institut, Universität Bayreuth, 95440 Bayreuth, Germany; [6]GeoSoilEnviroCARS, University of Chicago, 5640 South Ellis, Chicago, IL 60637, United States; [7]ESRF, Boîte Postale 220, 38043 Grenoble, France; [8]Department of Physics, Chemistry and Biology, Linköping University, SE-581 33 Linköping, Sweden*

An orthorhombic (space group *Pnnm*) boron phase was synthesized at pressures above 9 GPa and high temperature and it was demonstrated to be stable at least up to 30 GPa. The structure, determined by single-crystal X-ray diffraction, consists of $B_{12}$ icosahedra and $B_2$ dumbbells. The charge density distribution obtained from experimental data and *ab initio* calculations suggest covalent chemical bonding in this phase. Strong covalent interatomic interactions explain the low compressibility value (bulk modulus is $K_{300}$=227 GPa) and high hardness of high-pressure boron (Vickers hardness $H_V$=58 GPa), after diamond the second hardest elemental material.

Pure boron is one of the most enigmatic elements. Boron's three valence electrons

are too localized to make it metallic but insufficient in number to form a simple covalent structure. As a compromise, boron atoms form quasimolecular $B_{12}$ icosahedra that become building blocks of boron and boron-rich crystalline phases [1]. Several dozens of possible crystalline boron phases have been proposed in literature, but most of them proved to be borides or to be stabilized by small amount of impurities. Only α- (high-temperature form, rhombohedral, 12 atoms per a unit cell) and β-boron (rhombohedral, structure is not fully understood and consists of 105 or 108 atoms in the unit cell) are established as pure boron crystalline forms [2-4]. The existence of "tetragonal boron" as a modification of pure elemental boron or as boron-rich nitride or carbide has been a subject of controversy [5,6]. In addition, elemental boron exists in amorphous forms of different purity prepared by various techniques [7,8]. On compression of a β-boron single crystal at room temperature to 100 GPa, amorphization was observed [9]. Energy-dispersive X-ray powder diffraction experiments in laser-heated diamond anvil cells (DACs) suggest that β-boron is stable up to 30 GPa and 3500 K, and above these conditions a phase transition to the tetragonal "T-192" structure occurs [10]. Resistivity measurements demonstrate metallization of boron and the occurrence of a superconducting state at about 160 GPa [11]. However, the crystal structure of metallic boron is not known. Theoretical studies predict the transformation of α-boron into a phase with the α-Ga structure, accompanied by an insulator-metal transition [12].

In 1965 R.H. Wentorf [13] reported the synthesis of a new boron form at pressures above 10 GPa and temperatures above 1500 °C. The existence of this material [15] was not confirmed until recently when Zarechnaya et al. [14] reproduced the synthesis of the high-pressure boron phase and solved its structure from powder X-ray diffraction data. The high-pressure boron form has orthorhombic symmetry and its unit cell contains 28 atoms, so we designate it as $B_{28}$. Here we report the results of single-crystal X-ray diffraction studies of $B_{28}$ which, along with the results of our theoretical *ab initio* calculations, allow us to unambiguously conclude that the nature of chemical bonding in this phase is covalent. Additionally we demonstrate that $B_{28}$ is a wide band gap semiconductor, superhard, has low compressibility, and it is stable at least to 30 GPa at high temperatures.

Although polycrystalline $B_{28}$ is known [13] and has just attracted substantial attention [14,15,16], so far single crystals of this phase were not synthesized. Using a large-volume press, at 20 GPa and 1700 K we have grown elongated prismatic dark-red crystals with sizes of about 6x6x25 $\mu m^3$. The crystals are mixed with platinum boride PtB, which appeared due to a reaction of boron with a platinum capsule (see Ref. 17, Methods). We confirmed the purity of $B_{28}$ crystals by chemical analysis, collected single-crystal X-ray diffraction data (Ref. 17, *Single-crystal diffraction*), and refined the crystal structure (Table 4.2.1).

**Table 4.2.1.** Crystal structure data of orthorhombic $B_{28}$ (space group *Pnnm*, Z=28) at ambient conditions, obtained from powder and single-crystal x-ray diffraction data and from *ab initio* calculations.

|  | **Powder Diffraction [14]** | **Single-crystal Diffraction** | ***Ab initio* calculations** |
|---|---|---|---|
| *a* | 5.0563(4) | 5.0576(4) | 5.0434 |
| *b* | 5.6126(5) | 5.6245(8) | 5.6121 |
| *c* | 6.9710(7) | 6.9884(10) | 6.9248 |
| *V* | 197.83(4) | 198.80(4) | 196.0 |
| **B1 8h** | 0.162(2), 0.599(2), 0.794(9) | 0.1539(3), 0.5938(2), 0.7924(2) | 0.1528, 0.5925, 0.7908 |
| **B2 4g** | 0.645(2), 0.725(2), 0.5 | 0.6469(4), 0.7284(4), 1/2 | 0.6479, 0.7288, 0.5 |
| **B3 4g** | 0.335(2), 0.505(2), 0.0 | 0.3362(4), 0.5076(4), 0 | 0.3356, 0.5080, 0.0 |
| **B4 8h** | 0.837(2), 0.719(1), 0.870(1) | 0.8391(3), 0.7189(3), 0.8737(2) | 0.8393, 0.7189, 0.8743 |
| **B5 4g** | 0.669(2), 0.986(2), 0.0 | 0.6690(4), 0.9823(4), 0 | 0.6701, 0.9793, 0.0 |
| **R-factors** | wRp=6.5%, Rp=5.5.% | $R_1$=3.73%, $wR_2$=11.5% | |

There is remarkable agreement between structural parameters (Table 4.2.1) obtained from single crystal and powder X-ray diffraction data and those from our *ab initio* calculations [18]. The *bc* projection (Fig. 4.2.1a) shows that the structure is built of $B_{12}$ icosahedra and $B_2$ dumbbells linked together, thus forming a three-dimensional network. According to single-crystal X-ray diffraction data, the distances B-B within a $B_{12}$ icosahedron (1.766(3)-1.880(3) Å) are slightly longer than those within a dumbbell (1.721(4) Å). The shortest distances in the structure are those between atoms linking (1) two icosahedra – 1.659(4) Å, (2) an icosahedron and a dumbbell – 1.669(3) Å, and (3) two boron atoms within the dumbbell – 1.721(4) Å. Chemical bonds within $B_2$ dumbbells and $B_{12}$

icosahedra, as well as between an icosahedron and a dumbbell are strongly covalent, as is evident from the presence of residual electron density peaks (0.53 e/Å$^3$ and 0.40 e/Å$^3$ respectively) in the difference Fourier maps. Enhanced electron densities of similar magnitudes have been obtained in the same bonding regions using the Maximum Entropy Method [19] applied to the single-crystal X-ray diffraction data, thus confirming the strong covalent bonding character of these contacts.

*Ab initio* calculations also suggest strong charge density redistributions due to interactions of the boron atoms constituting the $B_{28}$-phase which lead to an increase of the charge density around the lines connecting boron atoms, i.e. to formation of covalent or polar covalent bonds. Also, the calculated electronic density of states projected onto $B_2$ dumbbells and $B_{12}$ icosahedra (Fig. 4.2.2) shows very strong hybridization, typical for the predominantly covalent bonds. Moreover, the calculated Electron Localization Function (ELF) [20,21] between the boron atoms (Fig. 4.2.1b) has a high value (about 0.9 at its maximum in the dumbbells-icosahedra bond), a characteristic feature of strong covalent bonding. Oganov et al. [16] reported results of theoretical studies on the orthorhombic $B_{28}$ high-pressure phase suggesting that the material is an ionic boron boride, $(B_2)^{\delta+}(B_{12})^{\delta-}$. Our experimental single crystal structural data and theoretical results do not confirm this model.

Calculated from structural data, the density of the $B_{28}$ phase is 2.54(1) g/cm$^3$ which is about 1% higher than densities of known (α-, β-, "tetragonal") boron modifications [1-4]. This is not surprising, because only $B_{28}$ contains additional B atoms in an inter-icosahedral space (although in β-boron there are probably interstitial defect atoms). The increased density of $B_{28}$ indicates that it may be stable at high pressure. Figure 4.2.3 summarizes the results of the multi-anvil quenched and *in situ* DAC experiments dedicated to studies of the relative stability of β-boron and $B_{28}$. At pressures below ~8.5 GPa only β-boron was observed in good agreement with previous reports [4,13,14]. At higher pressures we observed a formation of the orthorhombic phase found both in quenched products and *in situ* experiments by means of Raman spectroscopy and X-ray diffraction. If the $B_{28}$ phase synthesized in a DAC at pressures above 10 GPa is re-heated by laser at pressures below 7 GPa, it completely transforms back to β-boron thus confirming reversibility of the phase transition (Fig. 4.2.3).
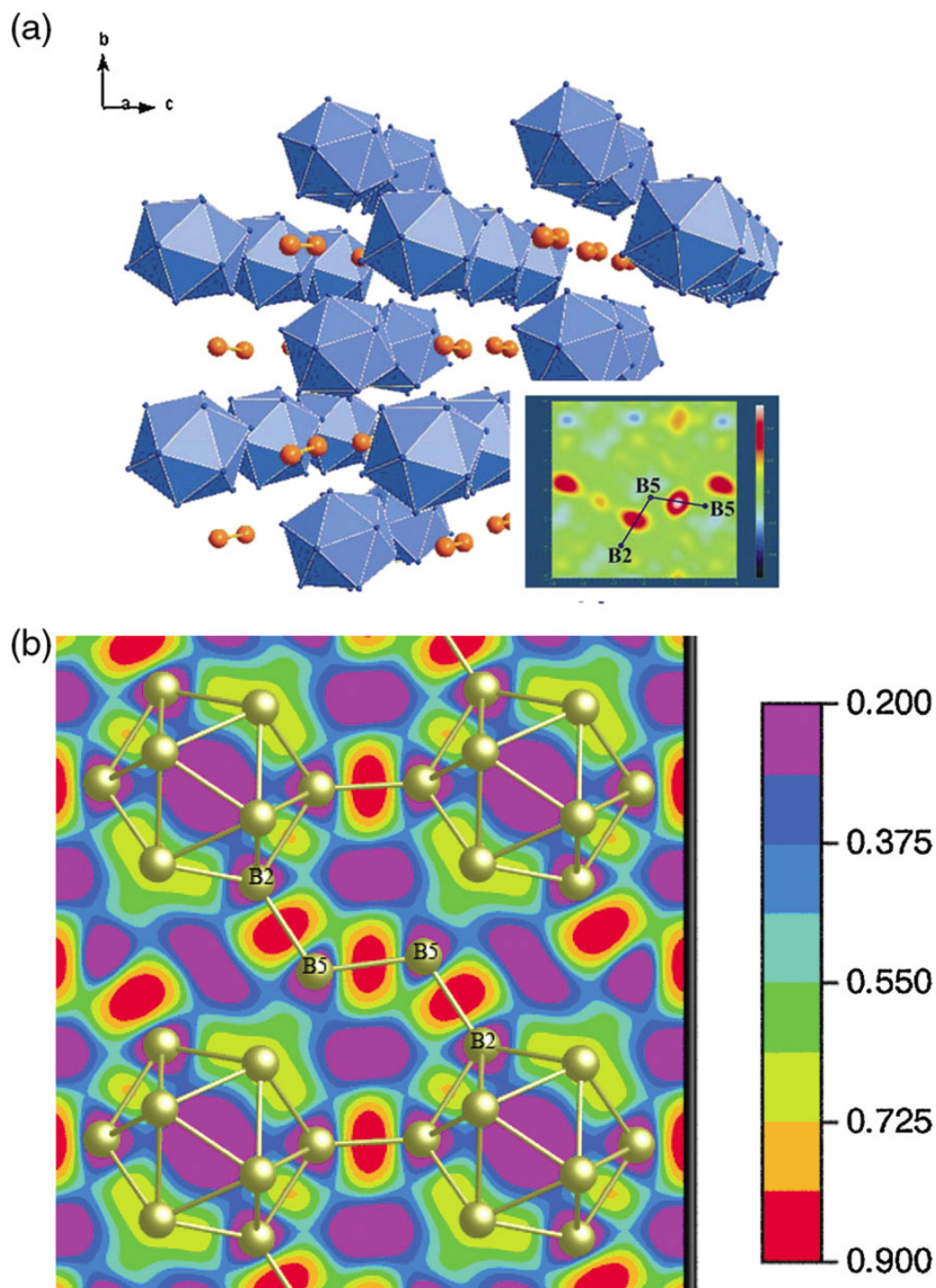
**Fig. 4.2.1.** (a) The structure of $B_{28}$ shown in the *bc* projection. The inset shows difference electron density plots around the atoms B5 (dumbbell) and B2 and B5 (dumbbell-icosahedron contact) extracted from experimental single-crystal X-ray diffraction data. The maximum electron density is centered in the middle of the bond, suggesting covalent bonding between the $B_2$ dumbbell and the $B_{12}$ icosahedron. (b) The calculated electron localization function in the plane through the dumbbell and dumbbell-icosahedra contacts.
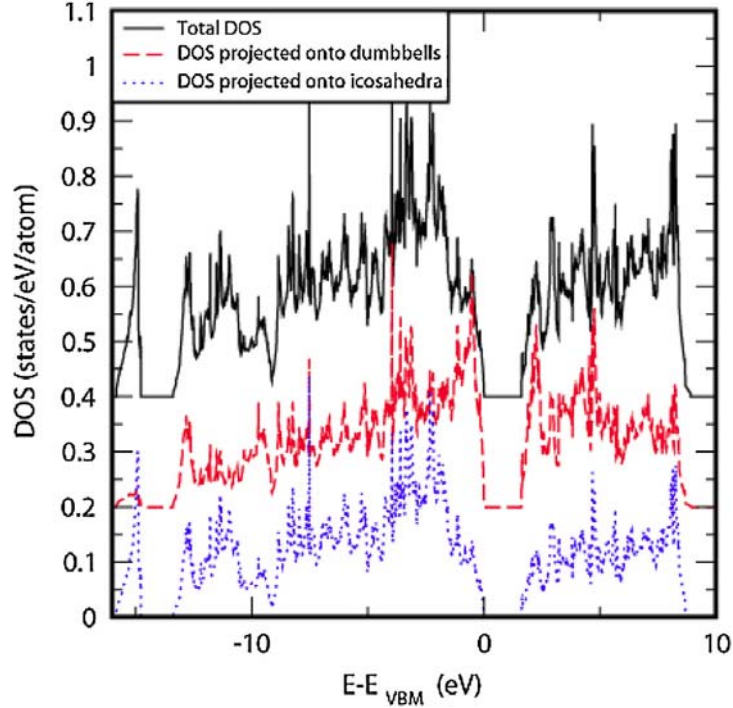
**Fig. 4.2.2.** (color online). Calculated total density of states (solid black line) as well as local density of states at boron atoms in the dumbbells ($B_2$) (dashed red line) and at boron atoms in the icosahedra ($B_{12}$) (dotted blue line). The energy is given with respect to the valence band maximum (VBM). For clarity, the three graphs are shifted with respect to each other by a constant shift.

In agreement with experiment, *ab initio* calculations suggest that orthorhombic boron is more stable than α-boron at pressures above about 20 GPa and on further compression it might transform into the α-Ga-type phase at about 88 GPa.

The higher density and strong covalent bonding in $B_{28}$ suggest that it could be less compressible than other known boron phases. The compression experiment (inset in Fig. 4.2.3) up to ~30 GPa in a DAC with Ne as a pressure transmitting medium and a powder of $B_{28}$ pre-synthesized in a multi-anvil press gave values of the bulk modulus of $K_{300}$=227(2) GPa and its pressure derivative K'=2.2(2) (the molar volume was fixed at the value of $V$=197.44(3) Å$^3$/unit cell measured at ambient conditions). *Ab initio* simulations (Fig. 4.2.3, inset) give $K_0$=221.7(7) GPa, K'=3.6(3), $V_0$=195.97(6) A$^3$. The value of K' we obtained experimentally is notably lower, but in accordance with the data of Sanz et al. [9] for β-boron. The values of the bulk moduli reported in literature for α-

and β-boron are in the range of 185-213 GPa [9,10,22] that is lower than the value we obtain for the $B_{28}$ phase.
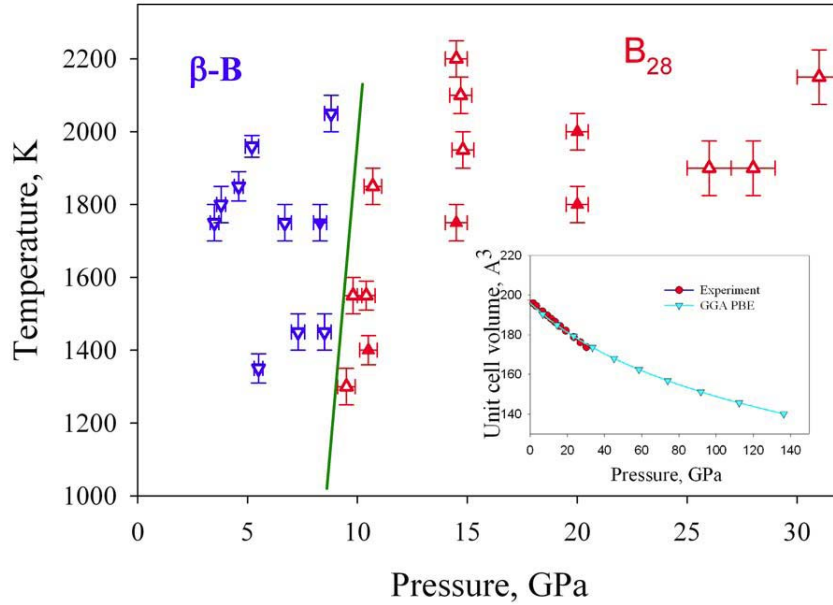


**Fig. 4.2.3.** Phase relations between β-boron (blue inverse triangles) and $B_{28}$ (red triangles) based on the results of the multi-anvil quenched (solid symbols) and *in situ* DAC (open symbols) experiments. The line is a tentative phase boundary between β-boron and the orthorhombic phase. The inset shows the experimental ($K_{300}$=227(2) GPa, K'=2.2(2), $V_0$=197.44(2) $A^3$) and calculated ($K_0$=221.7(7) GPa, K'=3.6(3), $V_0$=195.97 $A^3$) pressure dependence of molar volume of the orthorhombic $B_{28}$ boron phase.

The experimental data are too limited to discuss a mechanism of compressibility, but both high-pressure X-ray powder diffraction and theoretical calculations show (Ref. 17, Fig. S1) that the least compressible direction is the *a* axis, along which there are shortest contacts (and stronger covalent bonding) between $B_{12}$ icosahedra and $B_2$ dumbbells, while compression along *b* and *c* axes (normal to the channels hosting $B_2$ dumbbells) is easier.

In a thin section both polycrystalline samples and $B_{28}$ single crystals are transparent and have a red color (Fig. 4.2.4). The optical absorption edge of the orthorhombic boron phase, measured by the near-infrared and optical absorption spectroscopy is equal to 2.1 eV (Ref. 17*, Methods*). As usual, the first-principles calculations underestimate the band gap, so the obtained theoretical value of 1.7 eV (see

Fig. 4.2.2) is in reasonable agreement with experiment. Assuming that the optical absorption is due to excitations across the band gap we can apply an empirical rule that an indirect edge is generally well approximated by a linear relationship between square root of absorption coefficient and phonon energy [23]. Although this is true in a narrow region (about 0.2 eV) above the absorption edge, the optical spectra (Fig. 4.2.4) are too noisy to draw any firm conclusion regarding the nature (direct or indirect) of the band gap. However, theoretical calculations predict an indirect band gap (Ref. 17, *Fig. S2*).

Pure orthorhombic $B_{28}$ is a poor electrical conductor with a resistivity of the order of 106 Ohm cm at ambient conditions. With increasing temperature, the resistivity decreases indicating semiconducting behavior (Ref. 17, *Fig. S3*). The activation energy (1.9(2) eV) is in reasonable agreement with the value of the band gap energy determined from optical spectroscopy measurements.
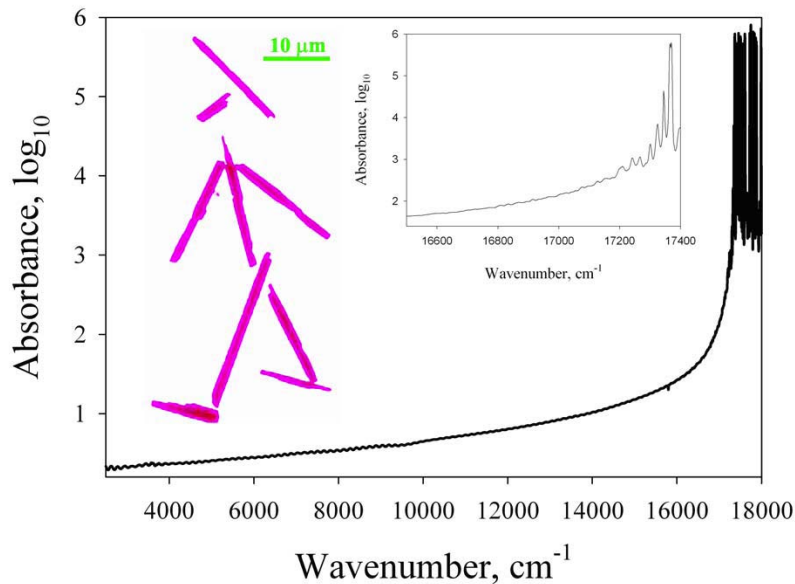


**Fig. 4.2.4.** Absorbance of the orthorhombic $B_{28}$ phase as determined by the near-infrared and optical absorption spectroscopy for a doubly-polished slice of the sample with a thickness of 10 μm. The inset on the right gives an enlarged view of the near-edge spectrum. The inset on the left shows a micro-photograph of single crystals of $B_{28}$ in transmitted light.

Boron is known as a hard material (with the Vickers hardness reported as high as 25-30 GPa [24] for β-boron). We measured the Vickers micro-hardness of the orthorhombic

boron phase in an asymptotic-hardness region (load up to 10 N) as recommended for hard and brittle materials and as described in our previous publications [25,26]. We found that samples with submicron grain sizes synthesized at 14 GPa and 1700 K in an indium medium have a hardness of 58(5) GPa (Ref. 17*, Fig. S4*). This value is in the range of polycrystalline cBN [24] that makes $B_{28}$ to be the second hardest elemental solid after diamond.

Our study demonstrates that the orthorhombic high-pressure high-temperature boron phase, synthesized above 9 GPa, has a new structure type, consists of covalently bonded $B_{12}$ icosahedra and $B_2$ dumbbells, and combines unusual properties – it is a wide band gap semiconductor that is superhard, optically transparent, and thermally stable (above 1000 K in air). We have proved the possibility to grow single crystals of this phase, which opens perspectives for applications of the new material in electronics and optics.

[1] K. C. Buschveck, Boron Compounds, Elemental Boron and Boron Carbides 13, Gmelin Handbook of Inorganic Chemistry (Springer-Verlag, Berlin, 1981).

[2] G. Will and B. Kiefer, Z. Anorg. Allg. Chem. 627, 2100 (2001).

[3] G. Will and K. Ploog, Nature (London) 251, 406 (1974).

[4] V.V. Brazhkin, T. Taniguichi, M. Akaishi, and S.V. Popova, J. Mater. Res. 19, 1643 (2004).

[5] R. Naslain, in Boron and Refractory Borides, edited by V. I. Matkovich (Springer-Verlag, Berlin, 1977).

[6] J. L. Hoard, D. B. Sullenger, C.H. L. Kennard, and R. E. Highes, J. Solid State Chem. 1, 268 (1970).

[7] K. Katada, Jpn. J. Appl. Phys. 5, 582 (1966).

[8] J. S. Gillespie, J. Am. Chem. Soc. 88, 2423 (1966).

[9] D. N. Sanz, P. Loubeyre, and M. Mezouar, Phys. Rev. Lett. 89, 245501 (2002).

[10] Y. Ma, Ch. T. Prewitt, G. Zou, Ho-kwang Mao, and R. J. Hemley, Phys. Rev. B 67, 174116 (2003).

[11] M. I. Eremets, V.V. Struzhkin, Ho-kwang Mao, and R. J. Hemley, Science 293, 272 (2001).

[12] U. Häussermann, S. I. Simak, R. Ahuja, and B. Johansson, Phys. Rev. Lett. 90, 065701 (2003).

[13] R. H. Wentorf, Science 147, 49 (1965).

[14] V. L. Solozhenko, O. O. Kurakevych, and A. R. Oganov, J. Superhard Mater. 30, 428 (2008).

[15] E.Yu. Zarechnaya, L. Dubrovinsky, N. Dubrovinskaia, N. Miyajima, Y. Filinchuk, D. Chernyshov, and V. Dmitriev, Sci. Tech. Adv. Mater. 9, 044209 (2008).

[16] During the review process of our manuscript, the following paper appeared: A. R. Oganov et al., Nature (London) 457, 863 (2009).

[17] See EPAPS Document No. E-PRLTAO-102-018921 for additional information on experimental and theoretical methods and results. For more information on EPAPS, see http://www.aip.org/pubservs/epaps.html.

[18] Ab initio simulations were performed using the projector augmented waves method as implemented in the VASP package; see G. Kresse and J. Furthmuller, Phys. Rev. B 54, 11 169 (1996). We used generalized gradient approximations, up to 12x12x12 k-points mesh. The energy cutoff was set to 600 eV.

[19] S. van Smaalen, L. Palatinus, and M. Schneider, Acta Crystallogr. Sect. A 59, 459 (2003).

[20] A. D. Becke and K. E. Edgecombe, J. Chem. Phys. 92, 5397 (1990).

[21] A. Savin et al., Angew. Chem., Int. Ed. Engl. 31, 187 (1992).

[22] R. J. Nelmes et al., Phys. Rev. B 47, 7668 (1993).

[23] R. Zallen and M. P. Moret, Solid State Commun. 137, 154 (2006).

[24] L. I. Berger, Semiconductor Materials (CRC Press, Boca Raton, FL, 1996), p. 472.

[25] V.V. Brazhkin, N. Dubrovinskaia, M. Nicol, N. Novikov, R. Riedel, V. Solozhenko, and Y. Zhao, Nature Mater. 3, 576 (2004).

[26] N. Dubrovinskaia, V. Solozhenko, N. Miyajima, V. Dmitriev, O. Kurakevych, and L. Dubrovinsky, Appl. Phys. Lett. 90, 101912 (2007).

*Supplementary Materials*

<u>Methods</u>

As starting materials for synthesis we used β-boron (Sigma-Aldrich Inc., 99.95% and 99.7% purity, $^{10}$B and $^{11}$B BCR$^®$ certified reference materials; Goodfellow Inc., 99.6% purity; Chempur Inc., 99.995 % purity), α-boron (Inorganic Chemestry Institute, Kiev, Ukraine, 98% purity; the sample provided by Dr. I. Goncharenko, approximately 97% purity), and amorphous boron (Chempur Inc., 95-97% purity; Goodfellow Inc., 98% purity).

*Multianvil Experiments*

Experiments were carried out using the 6/8-type multianvil Sumitomo 1200-ton and Zwick 5000-ton presses. Starting materials were loaded into BN-, MgO-, Au-, Pt- or In-capsules with a diameter of ~2.6 mm or ~2 mm and a height ~2.7 mm or ~3.5 mm. The temperature reached 1500 °C (in experiments with Au capsules) and 2000 °C (in MgO capsules) in different experiments. The 14/8 and 18/11 cell assemblies, composed of MgO (+ 5 wt. % $Cr_2O_3$) octahedra and $LaCrO_3$ heaters, were used. The pressure and temperature uncertainties were estimated to be 1 GPa and 50 K, respectively. After gradual compression of the samples to the desired pressures (up to 14 GPa in 14/8 assembly and up to 20 GPa in 18/11 assembly) the temperature was increased stepwise with a rate of about 200 K/min to the desired value. Duration of heating was up to 10 min in different runs. The samples were quenched by switching off the power supply. Samples were slowly decompressed during 1000 min.

*Diamond anvil cell experiments*

In-situ studies of phase transitions in β-boron were conducted at ID09 beam line at the ESRF (the wavelength of the monochromatic X-ray beam was 0.42 Å, MAR345 image

plate detector) and at IDD-13 beam line at APS (the wavelength of the monochromatic X-ray beam was 0.31 Å, MAR CCD detector).

In different runs the sample was clamped between diamond anvils with culets of 300 μm or 250 μm in diameter. Rhenium gaskets were indented to the thickness of about 50 μm and holes with diameter of 100 μm were drilled in the center. Small isometric pieces of crystalline β-boron (Chempur [©]) or the high-pressure phase synthesized in a multi-anvil apparatus were loaded into the holes along with ruby balls served as pressure markers. As a pressure transmitting medium NaCl, Ar, or Ne were loaded. One- and double-side laser heating was conducted at BGI, ESRF, and APS.

*Characterization of quenched samples at ambient conditions*

The quenched samples were studied using optical observations, the Raman and IR spectroscopy, and the X-ray diffraction.

For optical and IR observations thin sections of the HPHT phase were double-side polished to the thickness of about 10 μm.

The in-house X-ray powder diffraction studies were conducted using high-brilliance diffractometers (Mo $K_\alpha$ radiation) equipped with Osmic focusing X-ray optics and Bruker Apex CCD detector. At SNBL (ESRF, France) powder X-ray data were collected using monochromatic beam (0.7146 Å) and MAR345 detector.

Chemical composition and texture of the quenched samples were studied by means of a LEO-1530 scanning electron microscope (SEM) as well as by electron energy-loss spectroscopy (PEELS Gaten 666) in a Philips CM20 FEG analytical transmission electron microscope (ATEM), operating at 200 kV (Fig. S5).

In order to determine the band gap of the HPHT boron phase, the near infrared and optical absorption spectrum of a doubly polished slice of the sample with a thickness of

10 μm was investigated by Prof. H. Keppler (BGI, Bayreuth University, Germany). Measurements were carried out with a Bruker IFS 120 Fourier transform spectrometer coupled to an all-reflecting Bruker microscope. Near infrared spectra from 1000 to 10000 cm$^{-1}$ were measured with a tungsten source, a Si-coated $CaF_2$ beam splitter and a narrow-band MCT detector. Optical spectra were measured from 9000 to 25 000 cm$^{-1}$ with a tungsten source, a quartz beam splitter with dielectric coating and a Si diode detector. The spot size on the sample was 400 micrometers. 200 scans were accumulated for each spectrum and the two spectra were merged together.

*Single-crystal diffraction:*

A crystal of ~6x6x25μm size has been selected from the bulk sample and measured at the Swiss-Norwegian Beam Lines (SNBL) at the European Synchrotron Radiation Facility (ESRF). Diffraction data were collected at 293 K using the MAR345 Image Plate detector, 0.7706 Å wavelength and the crystal-to-detector distance of 100 mm. 300 frames with exposure time of 5 seconds have been collected. All diffraction intensities could be indexed by assuming four intergrown domains. The first domain, responsible for more than a half of the sample's scattering power, was indexed in a primitive orthorhombic lattice. Each of the three other domains had a primitive hexagonal cell with $a = 3.372(2)$, $b = 4.052(2)$ Å, inherent to the known PtB structure. All four domains were accounted for during the intensity integration using CrysAlis software [1]. Due to a good instrumental resolution and small mosaicity of the crystals only a few overlapping peaks were omitted, and a highly redundant dataset (~97% completeness, in average 10 equivalents or repetitive measurements per unique reflection) was obtained for the first domain. The data were corrected for Lorentz factor and polarization effects. Absorption correction and scaling of frames for the decaying intensity of the synchrotron beam were performed using SADABS [2]. The structure was solved and refined anisotropically (atomic displacement are listed in Table S1) using SHELX [3]. PLATON [4] did not detect higher metric or crystallographic symmetry, or any potentially unoccupied void.

Crystal data: formulae B, $M = 10.811$ g/mol, orthorhombic, space group *Pnnm*, $a = 5.0576(4)$, $b = 5.6245(8)$, $c = 6.9884(10)$ Å, $V = 198.80(4)$ Å$^3$, $Z = 28$, $\rho c = 2.528$ g/cm$^3$, $\mu = 0.093$ mm$^{-1}$, $T = 293$ K, $R$int $= 0.0196$ and $R\sigma = 0.0097$ over 2323 measured reflections. For 37 refined parameters: $R_1 = 0.0373$ and w$R_2 = 0.1135$ for 222 independent reflections with $I > 2\sigma$ (*I*); $R1 = 0.0387$ and w$R_2 = 0.1150$ for all 233 independent reflections, $GoF = 1.100$, $\Delta\rho$max/min $= 0.53(7)/-0.21(7)$ e/Å$^3$.
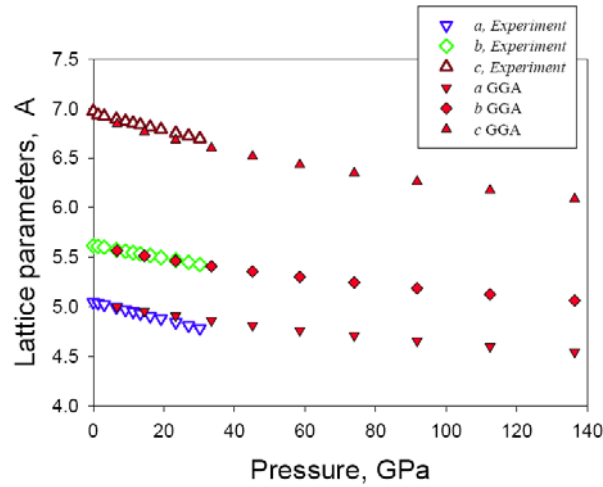


**Fig. S1.** Pressure dependence of lattice parameters of the orthorhombic B$_{28}$ boron phase.
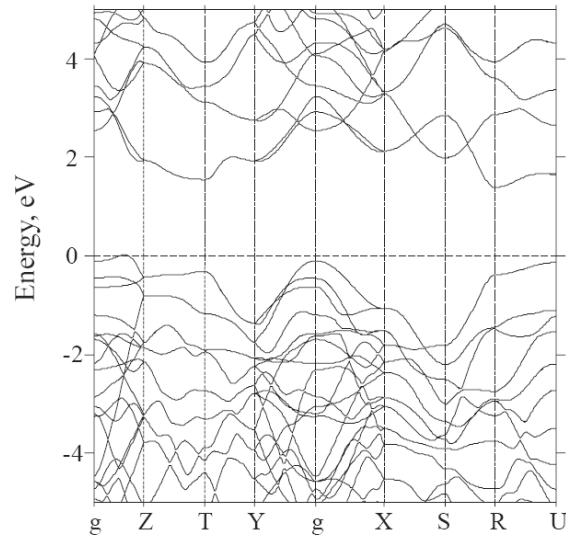


**Fig. S2.** Calculated band structure of the orthorhombic B$_{28}$ boron. *Ab initio* calculations predict an indirect band gap.
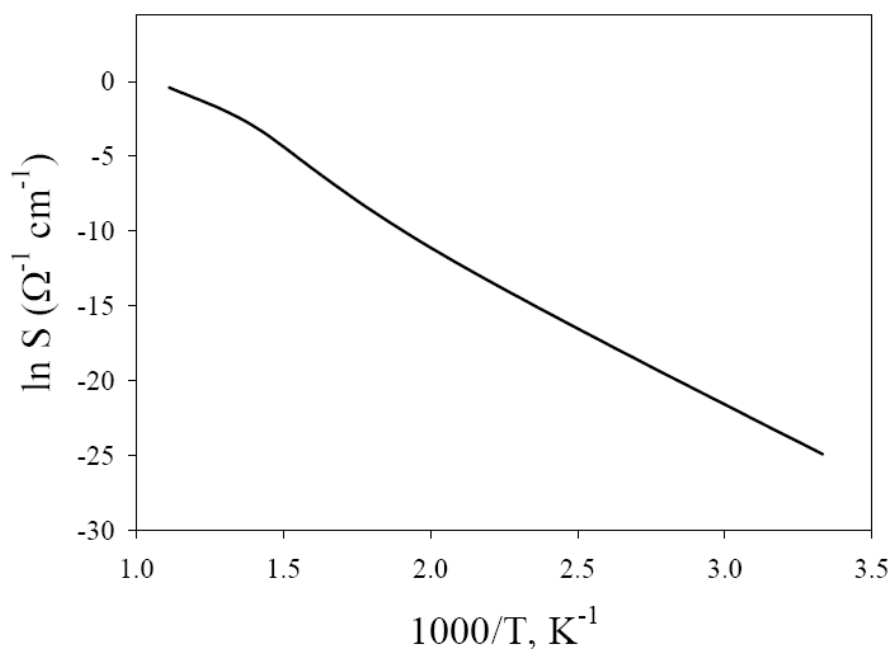
**Fig. S3.** Changes in conductivity of orthorhombic $B_{28}$ boron as a function of temperature.
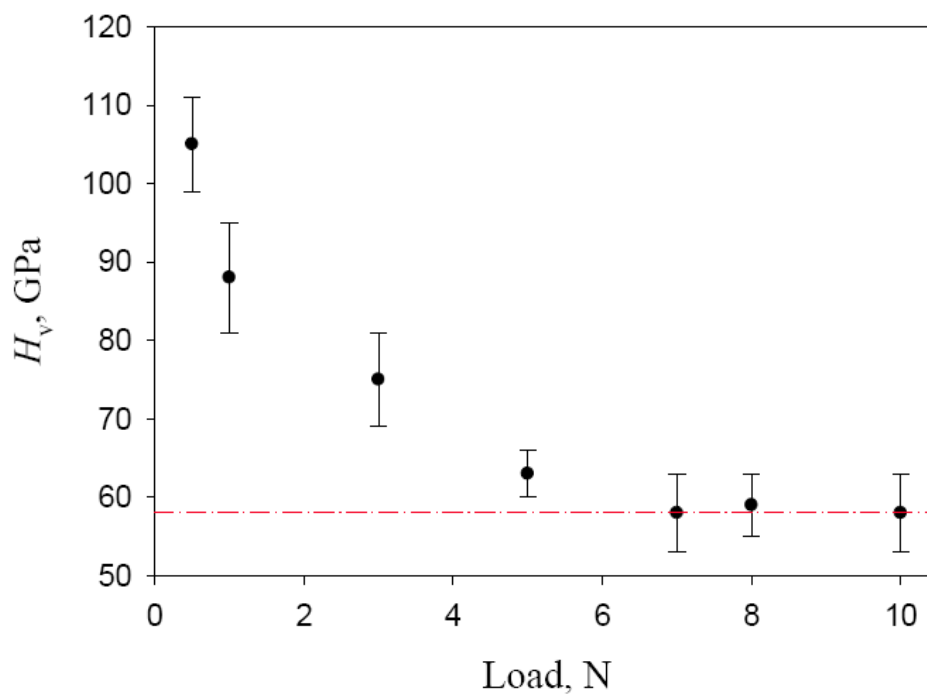


**Fig. S4.** The load dependence of the Vickers hardness for the orthorhombic boron phase measured with a microhardness tester (M-400-G2, LECO Corporation). At least five indentations were made for each data point to provide good statistics. As recommended for hard and brittle materials, hardness is reported in the asymptotic-hardness region (dot-dashed red line).
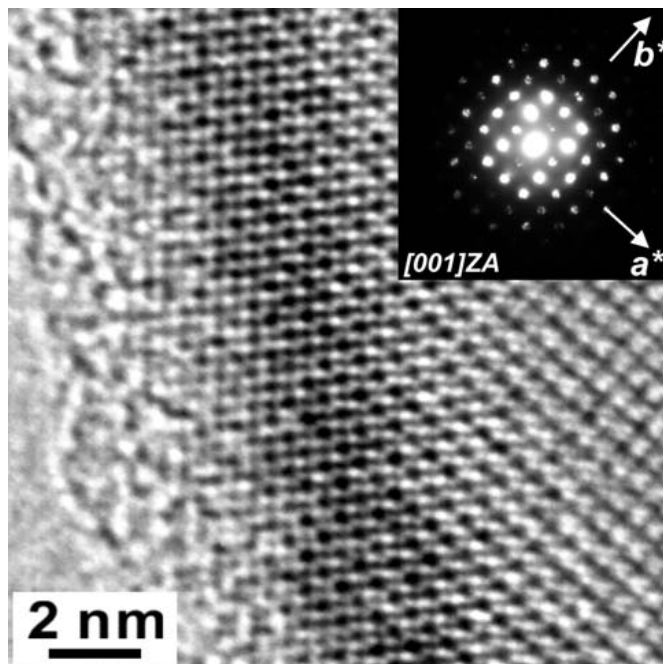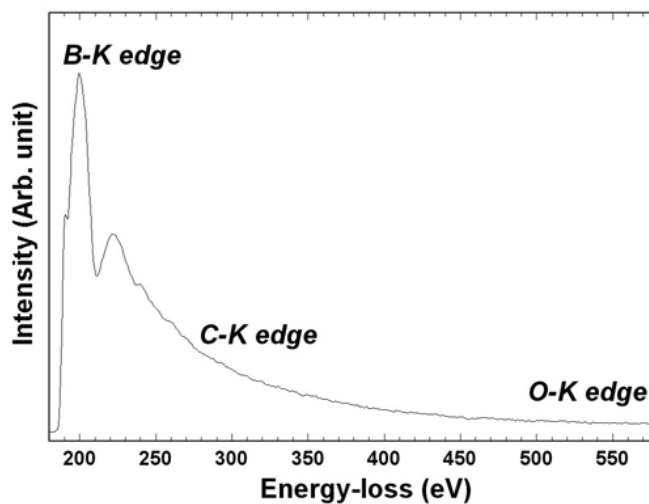
**Fig. S5a**



**Fig. S5b**

**Fig. S5.** (a) High resolution TEM image of the orthorhombic $B_{28}$ phase. Inset is a selected area electron diffraction pattern. (b) The core-loss EELS spectrum, confirming purity of the boron phase. The spectrum has been gain-normalized and deconvoluted by the Fourier-ratio method (R. E. Egerton, Electron Energy-Loss Spectroscopy in the Electron Microscope. Plenum Press, New York, 1996, pp485) using the low-loss spectrum.

**Table S1.** Anisotropic and equivalent isotropic atomic displacement parameters in the HPHT boron structure obtained from the room temperature single-crystal diffraction data.

| Atom | $U_{11}$ | $U_{22}$ | $U_{33}$ | $U_{23}$ | $U_{13}$ | $U_{12}$ | $U_{eqv}$ |
|------|----------|----------|----------|----------|----------|----------|-----------|
| **B1** | 0.0049(9) | 0.0058(8) | 0.0054(8) | 0.0004(5) | 0.0006(5) | 0.0003(4) | 0.0054(5) |
| **B2** | 0.0044(10) | 0.0064(11) | 0.0053(11) | 0.000 | 0.000 | -0.0008(6) | 0.0054(6) |
| **B3** | 0.0049(10) | 0.0052(10) | 0.0054(10) | 0.000 | 0.000 | -0.0002(6) | 0.0052(6) |
| **B4** | 0.0042(9) | 0.0050(8) | 0.0054(8) | -0.0006(5) | -0.0003(4) | -0.0002(4) | 0.0049(5) |
| **B5** | 0.0073(10) | 0.0073(10) | 0.0093(11) | 0.000 | 0.000 | 0.0006(7) | 0.0080(6) |

## 4.3 Polarized Raman spectroscopy of high-pressure orthorhombic boron phase

E. Yu. Zarechnaya[1], N. Dubrovinskaia[2,3], and L. Dubrovinsky[3]

[1]*Bayerisches Geoinstitut, Universität Bayreuth, 95440 Bayreuth, Germany;* [2]*Mineralphysik, Institut für Geowissenschaften, Universität Heidelberg, 69120 Heidelberg, Germany;* [3]*Lehrstuhl für Kristallographie, Physikalisches Institut, Universität Bayreuth, 95440 Bayreuth, Germany*

### 4.3.1. Abstract

We synthesized the single crystals of the orthorhombic (space group *Pnnm*) boron $B_{28}$ phase in a multi-anvil press and studied them by means of polarized Raman spectroscopy. Among all possible 42 Raman-active modes, we observed and assigned 32.

### 4.3.2. Introduction

Elemental boron and boron-rich compounds have been given particular scientific and technological attention because of their specific physical properties: high melting temperatures, wide energy band gap, high hardness, strong absorbance of neutrons, etc. The structures of these materials are based on icosahedral units as a common feature. Rhombohedral $\alpha$-boron consists of only $B_{12}$ icosahedra. It does not show any phase transitions on compression to at least 80 GPa at ambient temperatures [1]. Under heating up to 1200 °C at ambient pressure, $\alpha$-boron transforms into $\beta$-boron. Arrangement of B12 icosahedra in $\beta$-boron is complex, and its structure contains partially occupied sites [2]. The $\beta$-boron is less compressible (185–210 GPa [3,4]) in comparison with $\alpha$-boron (213–224 GPa [4]). Resistivity measurements indicate a transformation from $\beta$-boron into the

as yet unknown superconducting phase at about 160 GPa [5]. At pressures above 8.5 GPa and temperatures higher than 1500 °C, pure boron crystallizes in a structure with the *Pnnm* space group [6–9]. It contains 28 atoms in a unit cell (and here will be called $B_{28}$). The structure consists of $B_{12}$ icosahedra linked covalently with each other and $B_2$ dumbbells [7,8]. The presence of the B–B dumbbells in the intericosahedral space becomes a reason for a high value of the bulk modulus (227 GPa) of $B_{28}$ [8]. $B_{28}$ phase was demonstrated to be stable, at least to 30 GPa and 2000 K [8]. However, experimental information about the high-pressure behavior of the boron $B_{28}$ phase is so far limited. Indeed, X-ray diffraction studies are difficult to perform because boron is a weak scatterer. $B_{28}$ gives very distinct and strong Raman spectra at ambient conditions [7,8], and Raman spectroscopy could be the most convenient and useful technique for the investigation of high-pressure behavior of the phase, assuming that Raman modes are assigned. In the present work, we used the polarized Raman spectroscopy of single crystals of $B_{28}$ in order to assign experimentally observed modes.

### 4.3.3. Experimental

As a starting material for the synthesis of single crystals of $B_{28}$, we used *β*-boron (Chempur Inc., 99.995% purity). High-pressure experiments were carried out using 6-8-type multi-anvil Sumitomo 1200-ton and Zwick 5000-ton presses. Starting materials were loaded into Pt capsules of ~1.6mm (~2 mm) in diameter and of ~2.7mm (~3.5 mm) in height for the Sumitomo and Zwick presses assemblies, respectively. The temperature was 1900 K in all experiments. The cell assembly consisted of eight truncated WC cubes with an enclosed MgO + 5wt % $Cr_2O_3$ octahedron as a pressure medium. $LaCrO_3$ heaters were used. The pressure and temperature uncertainties were estimated to be 1GPa and 50 K, respectively. After gradual compression of the samples to desired pressures (up to 14 GPa in a 14/8 assembly and up to 20 GPa in a 18/11 assembly), the temperature was increased stepwise with a speed of about 200K/min to the desired value. The duration of the heating was up to 5 min in various runs. The temperature quenching was completed by switching off the power. Products were treated in a mixture of concentrated HNO3 and HCl at 80 °C for several hours. After the treatment, needle-shaped dark-red $B_{28}$

single crystals were extracted from the suspension and cleaned in distilled water. The chemical composition of the synthesized samples was studied by means of the scanning electron microscopy (LEO-1530). The phase purity was checked by X-ray diffraction [7,8].

A LabRam spectrometer (with a resolution of 2 cm$^{-1}$) and a He–Ne laser (632.8 nm) with a power of 15mW for excitation and 50× objective were used for the polarized Raman scattering experiments. The positions of Raman peaks were determined by fitting the experimental data using PeakFit$^{©}$ V4.12 software. Raman spectroscopy studies were conducted on single crystals (with characteristic dimensions of ∼5×5×25μm$^3$) and polycrystalline aggregates of the $B_{28}$ phase synthesized as described in [7]. Single crystals of $B_{28}$ were first preoriented using X-ray diffraction [8], then polished and used for polarized Raman spectroscopy. Raman spectra were collected in backscattered geometry with polarizers in both cross and parallel polarization configurations with respect to the incident laser polarization vector and described below accordingly to Porto notations [10].

## 4.3.4. Results and discussion

In the unit cell of the orthorhombic ($D_{2h}^{12}$, *Pnnm*) $B_{28}$, atoms occupy two 8 h and three 4 g Wyckoff positions [8]. Each atom in the 8 h position participates in 24 ($3A_g + 3A_u + 3B_{1g} + 3B_{1u} + 3B_{2g} + 3B_{2u} + 3B_{3g} + 3B_{3u}$) and in 4 g site in 12 ($2A_g + A_u + 2B_{1g} + B_{1u} + B_{2g} + 2B_{2u} + B_{3g} + 2B_{3u}$) Γ-point phonon modes. Out of total 84 modes, 42 are Raman active: $12A_g + 12B_{1g} + 9B_{2g} + 9B_{3g}$.

The Raman spectra of the $B_{28}$ single crystals were obtained between 150 and 1200 cm$^{-1}$ at several scattering configurations, as shown in Figure 4.3.4.1. The assignment of the measured Raman active modes is given in Table 4.3.4.1. Six combinations (*xx, yy, zz, xy, xz, yz*) of scattering geometries are necessary to obtain the full information on the polarization behavior of Raman bands [11]. In the case of orthorhombic (*Pnnm*) $B_{28}$ crystals, the Ag modes are allowed only with parallel scattering configurations ((*xx*), (*yy*), (*zz*)), while the $B_{1g}$, $B_{2g}$ and $B_{3g}$ are forbidden in these configurations, but should be clearly visible in the crossed (*xy*), (*xz*) and (*yz*) scattering geometries. However, in some

cases, the mode assessment is difficult. For example, a number of intense modes (at 593, 654, 895, 929, 1189 and 1218 cm$^{-1}$) are visible in all geometries, but they have higher intensities in some or even all parallel scattering configurations, which suggests that these modes have the A$_g$ symmetry. The modes at 878, 1133 and 1138 cm$^{-1}$ are the most intense in (*xy*) scattering geometry, and their intensity decreases in the spectra collected in the (*xz*) and/or (*yz*) configurations, which led to the assessment of these modes to B$_{1g}$ vibrations. In some cases (for example, for weak, poorly resolved and broad lines observed between 686 and 729 cm$^{-1}$ in (*xz*) and (*yz*) geometries), we cannot unambiguously conclude if modes are B$_{2g}$ or B$_{3g}$ or a mixture (Table 4.3.4.1). Finally, in experimentally observed polarized Raman spectra, we were able to determine 12A$_g$ and 12B$_{1g}$ lines, while unique assignment of B$_{2g}$ and B$_{3g}$ modes is problematic.
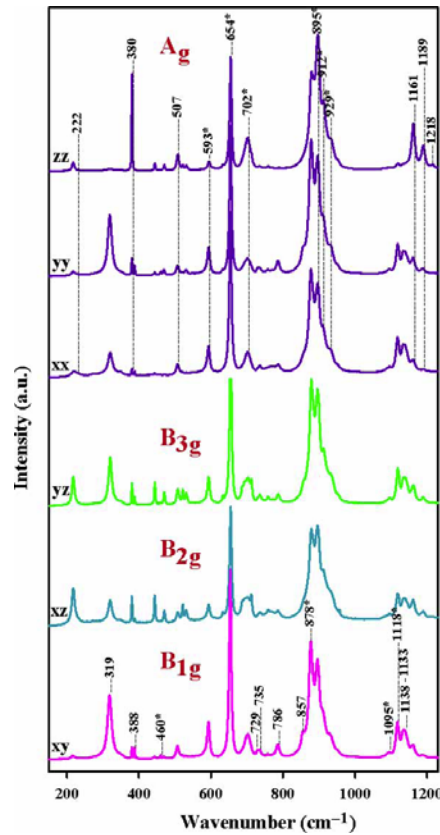


**Figure 4.3.4.1.** Polarized Raman spectra of HPHT B$_{28}$ single crystals obtained at ambient conditions in several scattering geometries. The polarization components are expressed according to Porto's notation [10]. The positions of Raman lines are marked according to Table 4.3.4.1. The ambiguously assigned modes are labeled with stars.

**Table 4.3.4.1.** Assignment of phonon frequencies of $B_{28}$ at ambient conditions.

| $\omega_{exp}(cm^{-1})$ | Assignment |
|---|---|
| 217(2) | $B_{2g}$, $B_{3g}$ |
| 222(2) | $A_g$ |
| 319(3) | $B_{1g}$, $B_{2g}^*$, $B_{3g}^*$ |
| 380(1) | $A_g$ |
| 388(2) | $B_{1g}$ |
| 444(2) | $B_{2g}$, $B_{3g}$ |
| 460(2) | $B_{1g}^*$ |
| 470(2) | $B_{2g}$, $B_{3g}$ |
| 507(2) | $A_{1g}$ |
| 521(2) | $B_{2g}$, $B_{3g}$ |
| 531(2) | $B_{2g}$, $B_{3g}$ |
| 593(3) | $A_g$ |
| 632(2) | $B_{2g}$, $B_{3g}$ |
| 654(2) | $A_g$ |
| 686(3) | $B_{2g}$, $B_{3g}$ |
| 693(3) | $B_{2g}$, $B_{3g}$ |
| 702(3) | $A_g^*$ |
| 712(3) | $B_{2g}$, $B_{3g}$ |
| 729(2) | $B_{1g}$ |
| 735(2) | $B_{1g}$, $B_{2g}^*$, $B_{3g}^*$ |
| 758(2) | $B_{3g}$ |
| 786(2) | $B_{1g}$ |
| 857(3) | $B_{1g}$, $B_{3g}^*$ |
| 878(2) | $B_{1g}$ |
| 895(2) | $A_g$ |
| 912(2) | $A_g$ |
| 929(2) | $A_g$ |
| 952(2) | * |
| 1095(2) | $B_{1g}$, $B_{2g}^*$, $B_{3g}^*$ |
| 1118(2) | $B_{1g}$ |
| 1133(2) | $B_{1g}$ |
| 1138(2) | $B_{1g}$ |
| 1161(2) | $A_g$ |
| 1189(2) | $A_g$ |
| 1218(2) | $A_g$ |

Types of atomic movements associated with certain Raman modes are difficult to determine based only on Raman spectra. However, a similarity in positions of Raman active modes found from a comparison of Raman spectra of boron carbides or pnictides [12] with those of $\alpha$-boron [13] on the one hand, and similarities of spectra of pnictides and $B_{28}$ (Figure 4.3.4.2) on the other hand, provides an opportunity to discuss the possible atomic vibrations associated with the Raman peaks. The Ag (380 cm$^{-1}$) and $B_{1g}$ (388

cm$^{-1}$) modes could be assigned from comparison with highly ordered pnictides ($B_{12}As_2$, $B_{12}P_2$) and boron carbide ($B_4C$) to icosahedron-dumbbell and $B_2$ dumbbells vibrations, correspondingly. By analogy with $\alpha$-boron [13], the mode at 319 cm$^{-1}$ could be due to librations of $B_{12}$ icosahedra. Modes observed between 507 and 1200 cm$^{-1}$ most probably arise from icosahedra vibrations (inter-icosahedral and intra-icosahedral).
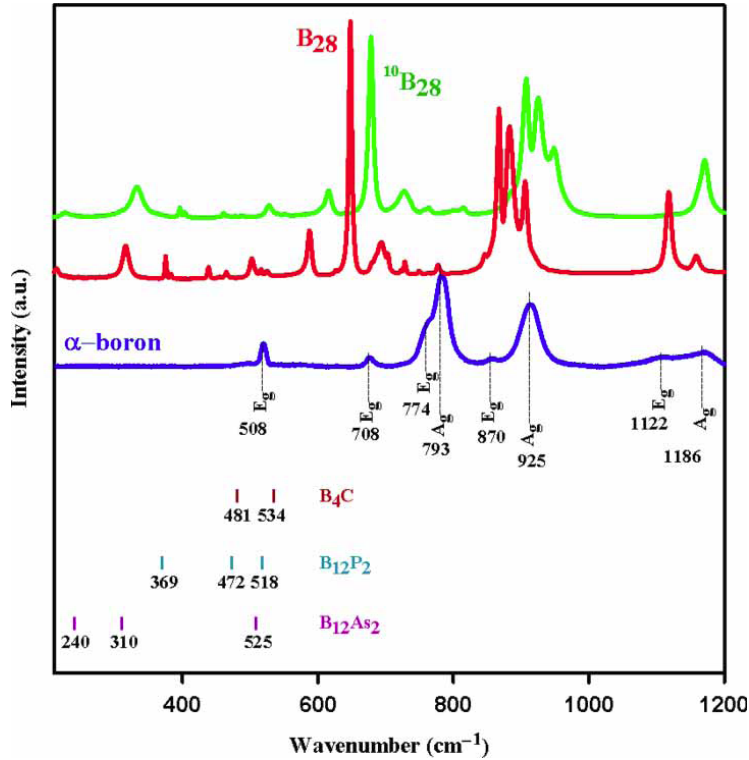


**Figure 4.3.4.2.** Comparison of the Raman spectra of polycrystalline orthorhombic $B_{28}$ (two upper curves) with that of $\alpha$-boron (lower curve) with mode positions from [13]. The spectrum from the $^{10}B_{28}$ sample (upper curve) is shifted proportionally to the square root of the mass ratio (1.039) with respect to that from the $B_{28}$ sample with a natural abundance of isotopes (middle curve) collected at ambient conditions. The positions of low-frequency lines of boron-rich compounds ($B_4C$, $B_{12}P_2$ and $B_{12}As_2$) [12] are shown as tick marks.

## 4.3.5. Conclusions

Boron is a light element and poor X-ray scatterer. It complicates the studies of boron behavior at high pressures. We demonstrated that good quality Raman spectra can be collected from single crystals of high-pressure, high-temperature boron phase $B_{28}$ and,

based on the polarized spectra, made a mode assignment. This result opens the way for a further study of $B_{28}$ lattice dynamics at high pressures.

## Acknowledgements

## References

[1] M. Kaneshige, S. Hirayama, T. Yabuuchi, T. Matsuoka, K. Shimizu, Y. Mita, H. Hyoudo, and K. Kimura, *Measurement of electrical resistance and Raman spectrum of α-boron under high pressure*, J. Phys. Soc. Japan 76 (2007), pp. 19–20.

[2] T. Ogitsu, F. Gygi, J. Reed, Y. Motome, E. Schwegler, and G. Galli, *Imperfect crystal and unusual semiconductor: boron, a frustrated element*, J. Am. Chem. Soc. 131 (2009), pp. 1903–1909.

[3] R.L. Nelmes, J.S. Loveday, D.R. Allan, J.M. Besson, G. Hamel, P. Grima, and S. Hull, *Neutron- and X-ray-diffraction measurements of the bulk modulus of boron*. Phys. Rev. B 47 (1993), pp. 7668–7673.

[4] D.N. Sanz, P. Loubeyre, and M. Mezouar, *Equation of state and pressure induced amorphization of α-boron from X-ray measurements up to 100 GPa*, Phys. Rev. Lett. 89 (2002), pp. 245501–245504.

[5] M.I. Eremets, V.V. Stuzhkin, H.-K. Mao, and R.J. Hemley, *Superconductivity in boron*, Science 293 (2001), pp. 272–274.

[6] R.H. Wentorf, *Boron: Another form*, Science 147 (1965), pp. 49–50.

[7] E.Yu. Zarechnaya, L. Dubrovinsky, N. Dubrovinskaia, N. Miyajima, Y. Filinchuk, D. Chernyshov, and V. Dmitriev, *Synthesis of an orthorhombic high pressure boron phase*, Sci. Technol. Adv. Mater. 9 (2008), pp. 044209-1–4.

[8] E.Yu. Zarechnaya, L. Dubrovinsky, N. Dubrovinskaia, Y. Filinchuk, D. Chernyshov, V. Dmitriev, N. Miyajima, A. El Goresy, H.F. Braun, S. Van Smaalen, I. Kantor, A. Kantor, V. Prakapenka, M. Hanfland, A.S. Mikhaylushkin, I.A. Abrikosov, and S.I.

Simak, *Superhard semiconducting optically transparent high pressure phase of boron*, Phys. Rev. Lett. 102 (2009), pp. 185501-1–4.

[9] A.R. Oganov, J. Chen, C. Gatti, Y.-Z. Ma, Y.-M. Ma, C.W. Glass, Z. Liu, T. Yu, O.O. Kurakevych, and V.L. Solozhenko, *Ionic high-pressure form of elemental boron*, Nature 457 (2009), pp. 863–867.

[10] T.C. Damen, S.P.S. Porto, and B. Tell, *Raman effect on zinc oxide*, Phys. Rev. 142 (1966), pp. 570–574.

[11] L. Nasdala, D.C. Smith, R. Kaindl, and M.A. Ziemann, *Raman spectroscopy: Analytical perspectives in mineralogical research,* EMU Notes Mineral. 6 (2004), pp. 281–344.

[12] D.R. Tallant, T.L. Aselage, A.N. Campbell, and D. Emin, *Boron carbide structure by Raman spectroscopy*, Phys. Rev. B 40 (1989), pp. 5649–5656.

[13] N. Vast, S. Baroni, G. Zerah, J.M. Besson, A. Polian, M. Grimsditch, and J.C. Chervin, *Lattice dynamics of icosahedral α-boron under pressure*, Phys. Rev. Lett. 78 (1997), pp. 693–696.

## 4.4   Growth of single crystals of B$_{28}$ at high pressures and high temperatures

E. Yu. Zarechnaya[1], N. Dubrovinskaia[2,3], L. Dubrovinsky[1], Y. Filinchuk[4], D. Chernyshov[4], V. Dmitriev[4]

*[1]Bayerisches Geoinstitut, Universität Bayreuth, 95440 Bayreuth, Germany; [2]Mineralphysik, Institut für Geowissenschaften, Universität Heidelberg, 69120 Heidelberg, Germany; [3]Lehrstuhl für Kristallographie, Physikalisches Institut, Universität Bayreuth, 95440 Bayreuth, Germany; [4]Swiss Norwegian Beam lines at ESRF, 38043 Gernoble, France*

### 4.4.1. Abstract

A method of the high pressure high temperature synthesis of single crystals of orthorhombic high pressure boron B$_{28}$ from metal solutions is presented. The method is based on the high-pressure multi-anvil technique. The feasibility of single crystal growth was demonstrated in a number of experiments conducted at various pressure-temperature conditions with various precursors including β-boron of 99.99 % purity and various metals (Cu, Au, and Pt) used as fluxes and capsule materials. It was found that after dissolution in metals at high pressures and high temperatures, boron crystallizes in form of single crystals at temperature decrease. The process is accompanied by chemical reactions resulting in formation of borides. The maximum length of the B$_{28}$ crystals achieved ~100 μm.

### 4.4.2. Introduction

Scientific studies of elemental boron have long-time history of more than 200

years [1]. Earlier attempts of chemical extraction of boron from solid substances or acids resulted in formation of different borides or products containing not more than 90% of pure boron [1,2]. The first pure single crystals of α-boron were grown by L.V. McCarty et al. [3]. The pyrolytic decomposition of $BI_3$ on different substrates (Ta, W, and BN) at temperatures of 1073-1273 K resulted in the formation of red crystals of 0.25 mm long [3]. The rhombohedral α-boron was found to be stable at temperatures lower than 1473 K. Under higher temperatures it irreversibly transforms into a more complex rhombohedral structure of β-boron (with 105-108 atoms in a unit cell) [4]. Single crystals of β-boron were obtained as a result of crystallization of the melt [5]. From the reduction of $BBr_3$ by $H_2$ at atmospheric pressure and temperatures as high as 1813 K, the so-called T-192 (or T-II) tetragonal-II boron phase was obtained [6]. The existence of the tetragonal-I (proposed as $B_{50}=B_{48}B_2$) form of pure boron is still under suspicion since reproducible synthesis yielded borides ($B_{50}C_2$ or $B_{50}N_2$) crystallized in the T-I structure [2].

For the first time, a high pressure high temperature (HPHT) modification of boron in powder form was obtained at 10 GPa and 1773 K by R.H. Wentorf [7].
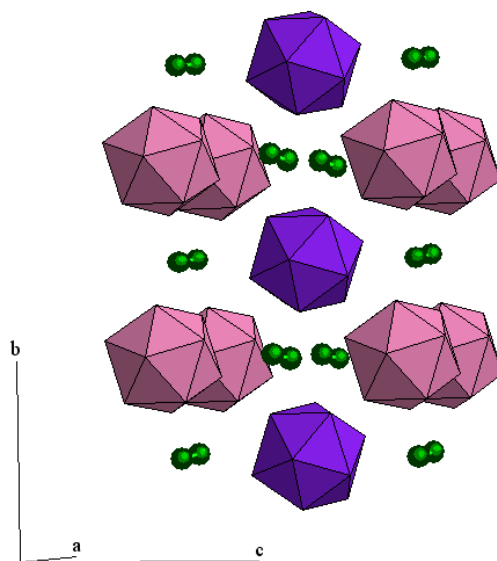


**Figure 4.4.2.1.** The structure of the high-pressure high-temperature orthorhombic boron phase ($B_{28}$) shown in the *bc* projection.

Recently, the existence of this phase was confirmed both experimentally and theoretically [8-10] and its structure was solved in the Pnnm space group. The unit cell of the HPHT allotrope of boron consists of 28 atoms (B$_{28}$) combined into icosahedra covalently linked with additional B$_2$ dumbbells filling the channels along the *a*-axis (Fig. 4.4.2.1). The orthorhombic B$_{28}$ may become a promising material for electronics due to the combination of useful physical properties such as optical transparency, high hardness, and semiconductor behavior. We have already shown a feasibility of synthesis of single crystals of B$_{28}$ [8] at high pressures and high temperatures and report in this paper the results of more systematic investigations on single crystal growth of B$_{28}$ using HPHT technique.

### 4.4.3. Experimental details

High pressure experiments were carried out using 6-8-type multianvil Sumitomo 1200-ton and Zwick/Voggenreiter 5000-ton presses. The cell assembly consisted of eight truncated WC cubes with an enclosed MgO + 5 wt. % Cr$_2$O$_3$ octahedron as a pressure medium. LaCrO$_3$ heaters were used. A cross-section of the HPHT cell is shown in Fig. 4.4.3.1. In experiments conducted in the 1200-ton press the volume of a cylindrical capsule was smaller (~5.5 mm$^3$) than that in the 5000-ton press assembly (~11 mm$^3$).

It was shown [8,9] that the B$_{28}$ phase appears in the HPHT synthesis only if a highly purified boron precursor with a purity better than 99.99% are used. All available for us powders of α-B and especially amorphous boron were contaminated and their use resulted in the formation of complex mixtures of different compounds [8]. In the present study polycrystalline, commercially available β-boron in form of granules with a typical size of ~50-100 μm (Chempur Inc., 99.995 % purity) or mixtures of the β-boron with 5, 10, 15, and 20 at.% of Pt or Cu were used as starting materials for HPHT synthesis. In various runs β-boron granules were loaded into Pt, Cu or Au capsules (Table 1). Mixtures of boron with Pt (99.999 % purity) or Cu (99.995 % purity) powders were loaded into gold capsules (Table 4.4.3.1).

The gradual compression of samples to pressures of 12 GPa, 14 GPa and 20 GPa was performed in 14/8 or 18/11 assemblies [11]. The temperature was increased stepwise
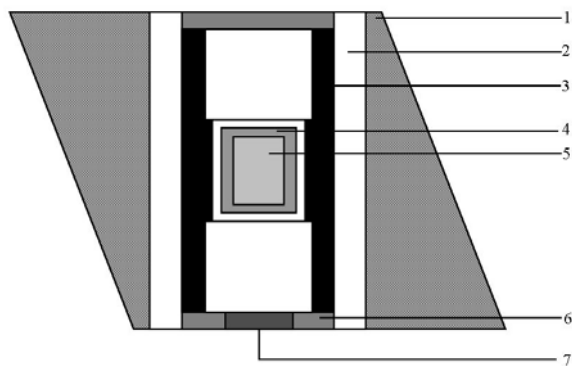
**Figure 4.4.3.1.** Cross-section of the HPHT cell used for the single crystal growth: 1- MgO+5% $Cr_2O_3$ octahedron; 2- $ZrO_2$; 3- $LaCrO_3$ heater; 4- capsule; 5- sample; 6- molybdenum ring; 7- pyrophyllite inset.

with a speed of about 200 K/min. Based on literature data [12, 13] we calculated melting temperatures of metals we used as capsules to be 1678 K and 1571 K at 12 GPa for Au and Cu, respectively, and 2426 K at 14 GPa for Pt. In fact, in our experiments we achieved melting of these metals at 2073 K at 12 GPa (Au), 1523 K at 12 GPa (Cu) and 2173 K at 14 GPa (Pt). In experiments with β-boron mixed with metal powders the heating was performed up to 1773 K. Duration of heating varied between 2 and 7 minutes in various runs. The temperature quenching was done by switching off the power. In the experimental run S4390 after 2 minutes of heating at temperature above 1773 K we gradually decreased temperature during 18 min down to 1073 K, and then quenched the sample. In all experiments the uncertainties in pressure and temperature determination were estimated to be 1 GPa and 50 K, respectively.

After experiments the capsules were extracted from the octahedra. Products of synthesis with capsules were treated in a mixture of concentrated $HNO_3$ and HCl (1:3) at ~373 K during several hours. Products of the treatment were extracted from a suspension and cleaned in distilled water.

The morphology and chemical composition of the synthesized samples of single crystals were studied by means of the scanning electron microscopy (SEM) (LEO-1530). Chemical purity of the samples was confirmed using WDX microprobe analysis (Jeol JXA-8200; focused beam; 20 keV, 20 nA). Counting time for each element was 20 s at

the peak position and 10 s at each background position. For calibration BN, Pt, Au, carbon, and MgO were used as standards. ZAF corrections method was applied.

**Table 4.4.3.1.** Summary of experiments on synthesis of single crystals of the orthorhombic $B_{28}$ phase. Intermetallic phases originated from chemical reactions between precursor powders and capsule materials are marked as asterisks (*). Abbreviation "SC" means "single crystal". The size of $B_{28}$ single crystals is given as an average value for every experiment.

| Experiment | Starting material | Conditions | | | | Synthesis products | Average size of $B_{28}$ crystals (μm) |
|---|---|---|---|---|---|---|---|
| | | Capsule material | Temperature (K) | Pressure (GPa) | Heating time (min) | | |
| S4439 | 95 at.% β-B + 5 at.% Cu | Au | 1723 | 12 | 7 | Orthorhombic $B_{28}$, (*) | - |
| S4409 | 90 at.% β-B + 10 at.% Cu | Au | 1723 | 12 | 6 | Orthorhombic $B_{28}$, (*) | SC, 8x8x100 |
| S4442 | 85 at.% β-B + 15 at.% Cu | Au | 1923 | 12 | 2 | Orthorhombic $B_{28}$, $B_{24}Cu$, (*) | 25x50 |
| S4445 | 80 at.% β-B + 20 at.% Cu | Au | 1723 | 12 | 3 | Orthorhombic $B_{28}$, $B_{24}Cu$, (*) | SC, 6x10/6x60, irregular shape |
| S4457 | β-B | Cu | 1523 | 12 | 3 | Orthorhombic $B_{28}$, $B_{24}Cu$, (*) | SC, 6x6x58 |
| S4390 | 98.5 at.% β-B + 1.5 at.% Pt | Au | 1723 | 12 | 2 | Orthorhombic $B_{28}$, BPt, (*) | - |
| S4490 | 95 at.% β-B + 5 at.% Pt | Au | 1723 | 12 | 3 | Orthorhombic $B_{28}$, BPt, (*) | SC, 4x4x92 |
| S4486 | 90 at.% β-B + 10 at.% Pt | Au | 1723 | 12 | 3 | Orthorhombic $B_{28}$, BPt, (*) | SC, 9x9x80, irregular shape |
| S4480 | 85 at.% β-B + 15 at.% Pt | Au | 1723 | 12 | 3-4 | Orthorhombic $B_{28}$, BPt, (*) | - |
| S4400 | 80 at.% β-B + 20 at.% Pt | Au | 1723 | 12 | 6 | Orthorhombic $B_{28}$, BPt, (*) | SC, 3x3x21 |
| Z612 | β-B | Pt | 2173 | 20 | 5 | Orthorhombic $B_{28}$, BPt, (*) | SC, 6x6x25 |
| Z657 | β-B | Pt | 2173 | 14 | quenched immediately | Unknown phases | SC, 6x6x58 |
| S4477 | β-B | Au | 1723 | 12 | 4 | Orthorhombic $B_{28}$, (*) | SC, 8x8x70 |
| S4492 | β-B | Au | 2073 | 12 | quenched immediately | Orthorhombic $B_{28}$+unknown phases | SC, 25x25x104 |

All samples and standards were carbon coated with thickness of the coating of 10 nm. Phase compositions of products were checked using the X-ray diffraction. The *in-house* powder X-ray diffraction studies were conducted using a high-brilliance Rigaku

diffractometer (Mo Kα radiation) equipped with Osmic focusing X-ray optics and Bruker Apex CCD detector.

The quality of the grown single crystals obtained in experiment Z612 (Table 6.4.3.1) with a size of about of 25x6x6 μm was checked at Swiss-Norwegian Beam Lines (SNBL) at the European Synchrotron Radiation Facility (ESRF, France). The diffraction data were collected at 293 K using a single-crystal diffractometer KUMA KM6-CH equipped with a CCD detector with a monochromatic beam (0.7146 Å).

The Raman system with a He-Ne laser (632.8 nm) at a power of 15 mW for excitation and a LabRam spectrometer (the spectral resolution of 2 cm$^{-1}$) was used to collect Raman spectra from the samples. In order to avoid heating of the samples by the laser, Raman spectra were collected for 2 seconds using the x50 objective and D2 filter.

## 4.4.4. Results and discussion

The transition from β-B to the B$_{28}$ phase occurs at pressures higher than 8.5 GPa and temperatures above ~1773 K [8]. We conducted a series of experiments on synthesis of single crystals of B$_{28}$ from HT solutions in metals at pressures above 12 GPa and temperatures in the range of 1523 to 2173 K. Table 4.4.3.1 summarizes experimental data on synthesis of single crystals of B$_{28}$ at HPHT conditions.

## 4.4.4.1 Characterization of the quality of B$_{28}$ single crystals

The formation of red needle-shaped single crystals of B$_{28}$ in HPHT experiments (20 GPa, 1873 K) performed in Pt-capsules has been already reported [8]. The grown single crystals (experimental run Z612) were analyzed using synchrotron radiation at SNBL (ESRF). The rocking curves were measured with a 0.01° step in ω and the peaks were found to be almost symmetrical. As examples, the rocking curves of the distant reflections ((2 $\bar{1}$ 4) and (1 $\bar{1}$ 3)) of the B$_{28}$ phase are presented in Fig. 4.4.4.1.1. The full width at half maximum (FWHM) of the chosen reflections was fitted by the pseudo-Voigt function and determined to be 0.0379(5)° (Fig. 4.4.4.1.1(a)) and 0.0346(4)° (Fig. 4.4.4.1.1(b)) in ω, correspondingly. These values are comparable with the pure

instrumental function of the KUMA diffractometer, thus proving an evidence of a high quality of the B$_{28}$ single crystals. The direction of elongation of B$_{28}$ crystals was established to coincide with the crystallographic *a*-axis, i.e. with the direction of channels in the structure filled by B$_2$ dumbbells. The crystal faces are formed by the (011) prism.
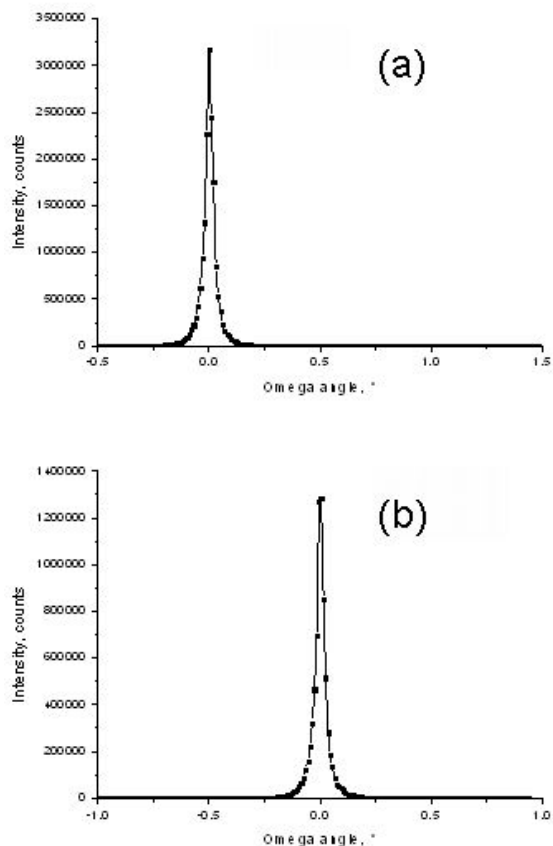


**Figure 4.4.4.1.1.** Rocking curves of ($2\bar{1}4$) (a) and ($1\bar{1}3$) (b) reflections of B$_{28}$ singly crystal (Z612, see Table 6.4.3.1) measured at room temperature.

## 4.4.4.2 Influence of experimental conditions on the synthesis products

The results of synthesis, in particular, the shape and size of grown crystals, their quality, etc. depend on many factors including materials used as a flux. The binary phase diagrams of boron with some metals, in particular Pt, Cu, Au (used in the present work as solvents for boron), were studied mostly at atmospheric pressures [14]. Reaction of Pt

and B under pressure was studied by E.D. Whitney and R.F. Giese [15] at pressures below 5 GPa and temperatures up to about 1023 K. They found that the reaction B + Pt → BPt occurs at non ambient conditions. The slope of the curve representing the boundary in the P-T phase diagram for this reaction was found to have a value of dP/dT =133 bars/degree. H.M. Strong and F.P. Bundy [16] found a value of dP/dT for the melting point of Pt to be 140 bars/degree. Thus, the formation of BPt occurs at temperatures very close, but slightly lower than those necessary for melting of Pt at high pressure.

At atmospheric pressure [14] B and Pt react together and form the phases with the following stoichiometry: B$_2$Pt$_3$, BPt$_2$, and BPt$_3$. In fact, according to Ref. 14, in reality B$_2$Pt$_3$ may be BPt and thus high pressure BPt [15] can be also produced at ambient pressure [14]. Interestingly, the BPt phase in high pressure high temperature experiments of E.D. Whitney and R.F. Giese [15] was traced to the reaction of boron and the platinum foil used to encapsulate the boron containing samples. In our experiments on synthesis of B$_{28}$ single crystals Pt capsules were also used (Table 4.4.3.1). The eutectic point of the B-Pt system at ambient pressure occurs at 1213 K according to Ref. [14]. Following the P-T phase diagram of E.D. Whitney and R.F. Giese [15] we intended to reach temperature above the eutectic point of the B-BPt system at pressures above 8.5 GPa, i.e. in the pressure- temperature range of stability of B$_{28}$ [9]. Decrease of temperature below liquidus had to result in crystallization of B$_{28}$. Indeed, the X-ray diffraction patterns collected from all "as synthesized" samples (i.e. those before the acid treatment, obtained from HP synthesis with β–boron in Pt capsules or with precursors with up to 20 at.% of Pt-additive (see Table 4.4.3.1)) show the presence of the BPt phase additionally to the B$_{28}$ phase. The diffraction peaks of the observed BPt phase (Table 4.4.4.2.1) match well with those of the ICDD PDF #13-0288 for BPt.

In order to explore other possible solvents for the single crystal growth, Cu was used as both an additive to boron and a capsule material, while Au was used only as a capsule material. The Cu-B phase diagram is not complicated by Cu-B compounds. Melting temperature of Cu is considerably lower than that of Au and Pt at the same pressures. This and the relatively low eutectic point (1283 K) at ambient pressure suggest a possibility for the successful single crystal synthesis of B$_{28}$. The same procedure as for a

series of experiments with Pt was used in experiments with Cu. Various amounts of a Cu powder (5, 10, 15, 20 at.%) were used as an additive to β-B. The mixtures were loaded into an Au-capsule. The X-ray diffraction patterns of products showed the presence of the diffraction lines of intermetallic compounds (CuAu, Cu$_3$Au, CuAu$_3$, etc.) or alloys [14], which form when Cu reacts together with Au. Thus, the B$_{28}$ crystals likely grow in the Cu-Au flux. At higher Cu content (above 15 at %) in a mixture with β-B in an Au capsule or at synthesis from pure β-B in a Cu capsule a formation of the Cu- boride (CuB$_{24}$, ICDD PDF #26-1111) (Table 4.4.4.2.1) was observed. At low amount of Cu- additive (up to 10 at %) Cu-boride did not appear. The analysis of the dependence of chemical compositions of intermetallic compounds or alloys as a function of the synthesis conditions was out of the scope of the present work, but seems that in our experiments the only use of an Au capsule and a pure boron precursor resulted in the formation of pure B$_{28}$ single crystals mixed with polycrystalline aggregates of B$_{28}$ (Fig. 4.4.4.2.1) free from any borides.
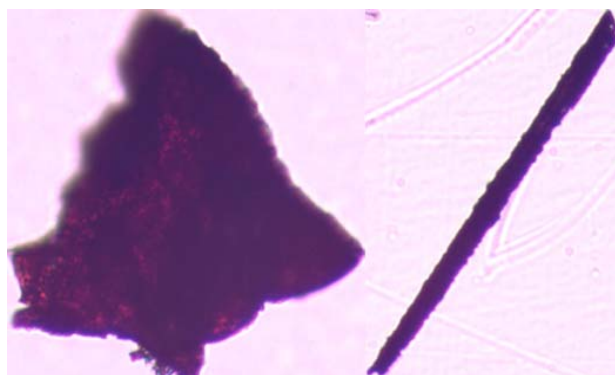


**Figure 4.4.4.2.1.** Microphotograph of a polycrystalline aggregate (left) and a single crystal (right) of B$_{28}$ phase synthesized in an Au capsule at P=12 GPa and T=1723 K (experiment S4477, see Table 4.4.3.1).

As already mentioned above, all used metals, as well as produced intermetallic compounds or alloys, are dissolvable in the mixture of acids, HCl and HNO$_3$ (3:1). Copper- and platinum borides are also dissolvable in the mixture of these acids. After several hours of boiling of samples in the acids at temperature of ~373 K we did not see any trace of these compounds in the residual material. Only crystals of a characteristic red color and their aggregates left.

**Table 4.4.4.2.1.** *d*-spacings of BPt (experiment S4486) and $B_{24}Cu$ (experiment S4445) phases determined from X-ray powder diffraction and those reported in the Powder Diffraction Database (#13-0288 (BPt), #26-1111 ($B_{24}Cu$)).

| Phase | d(PDF) (Å) | d(OBS) (Å) | hkl | $I/I_0$ |
|---|---|---|---|---|
| **BPt** | 2.9100 | 2.9300 | 1 0 0 | 75 |
|  | 2.3620 | 2.3694 | 1 0 1 | 100 |
|  | 2.0270 | 2.0314 | 0 0 2 | 50 |
|  | 1.6780 | 1.6833 | 1 1 0 | 75 |
|  | 1.6670 | 1.6672 | 1 0 2 | 75 |
|  | 1.4570 | 1.4452 | 2 0 0 | 25 |
|  | 1.3700 | 1.3638 | 2 0 1 | 75 |
|  | 1.2950 | 1.2917 | 1 1 2 | 90 |
|  | 1.2260 | 1.2292 | 1 0 3 | 60 |
| **$B_{24}Cu$** | 8.8500 | 8.7484 | 1 0 1 | 80 |
|  | 7.9800 | 8.0211 | 0 0 3 | 90 |
|  | 5.4900 | 5.0639 | 1 1 0 | 100 |
|  | 4.5200 | 4.5499 | 1 1 3 | 12 |
|  | 4.4200 | 4.4425 | 2 0 2 | 16 |
|  | 4.2800 | 4.2839 | 0 1 5 | 10 |
|  | 3.9800 | 4.0592 | 0 0 6 | 60 |
|  | 3.5500 | 3.4883 | 2 1 1 | 100 |
|  | 3.4400 | 3.4394 | 1 2 2 | 30 |
|  | 3.3700 | 3.3357 | 2 0 5 | 4 |
|  | 3.2200 | 3.1910 | 1 0 7 | 30 |
|  | 3.0800 | 3.1016 | 2 1 4 | 12 |
|  | 2.8700 | 2.8679 | 1 2 5 | 5 |
|  | 2.7800 | 2.7787 | 0 2 7 | 20 |
|  | 2.5300 | 2.5345 | 2 0 8 | 6 |
|  | 2.4800 | 2.5144 | 3 0 6 | 50 |
|  | 2.4100 | 2.4707 | 1 3 4 | 4 |
|  | 2.3330 | 2.3200 | 0 4 2 | 55 |
|  | 2.3100 | 2.2947 | 3 1 5 | 4 |
|  | 2.1230 | 2.1478 | 0 1 11 | 12 |
|  | 2.0870 | 2.0936 | 1 3 7 | 25 |
|  | 2.0490 | 2.0481 | 3 2 4 | 65 |
|  | 2.0360 | 2.0329 | 3 0 9 | 35 |
|  | 1.9940 | 1.9919 | 0 0 12 | 10 |
|  | 1.9800 | 1.9615 | 3 1 8 | 12 |
|  | 1.8310 | 1.8398 | 3 3 0 | 16 |
|  | 1.7830 | 1.7991 | 3 3 3 | 14 |
|  | 1.7650 | 1.7668 | 5 0 5 | 60 |
|  | 1.7150 | 1.7311 | 0 2 13 | 20 |
|  | 1.6860 | 1.6830 | 4 0 10 | 40 |

Raman spectra (Fig. 4.4.4.2.2a) of all "as synthesized" samples are similar and resemble that of $B_{28}$ well characterized by various methods in our previous works [8,9,17]. The spectra do not show any difference in the number of active vibration modes or shifts of modes that could indicate metal incorporation into the structure of the $B_{28}$ phase (Fig. 4.4.4.2.2a).

The electrical resistivity of single crystals along the longer direction (Fig. 4.4.4.2.1) was measured by the four-probe method [9] (shorter directions of our crystals are too small for connection of electrodes). Changes in conductivity of orthorhombic B$_{28}$ boron single crystals as a function of temperature are very similar to that observed for the bulk material (Fig. 4.4.4.2.2b).
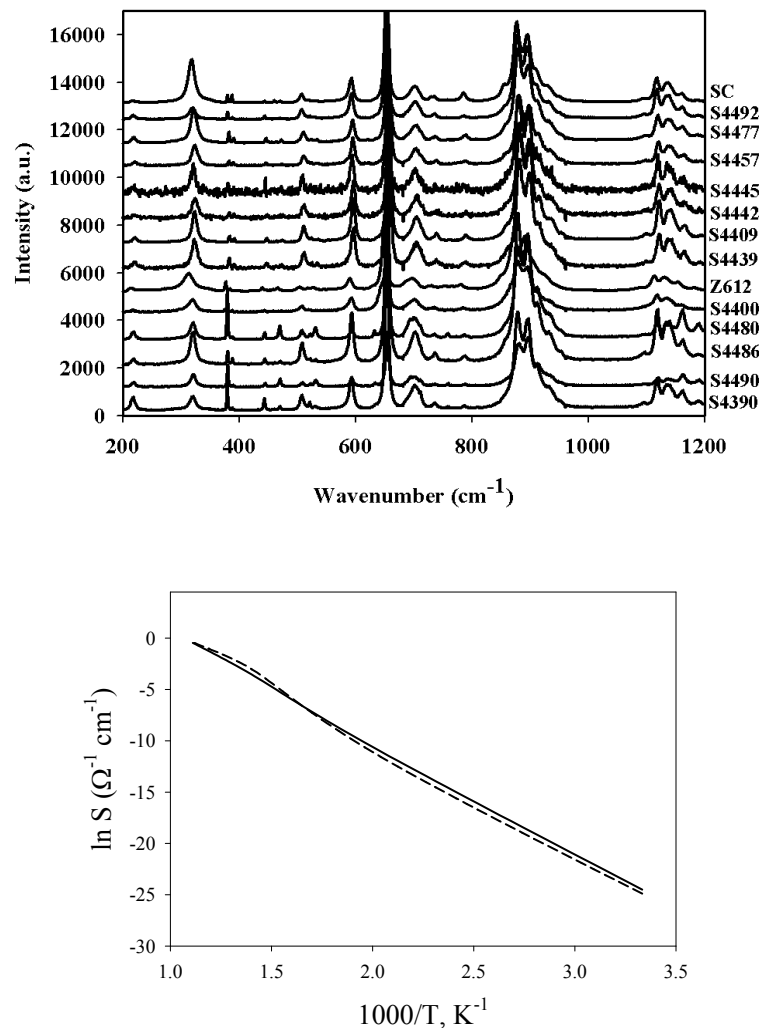


**Figure 4.4.4.2.2.** (a) Raman spectra from products of B$_{28}$ synthesis of various experiments compared with those from a well characterized single crystal (SC-experiment Z612); (b) Changes in conductivity of orthorhombic B$_{28}$ boron single crystals (continuous line; measured along longer direction) and bulk material (dashed line) as a function of temperature.

It is worth noticing that X-ray diffraction of the samples synthesized at elevated temperatures (2073 K and 2173 K) showed the presence of unknown phases (experiments

Z657 and S4492). These phases are likely the products of chemical reactions of precursors and the capsule materials with other materials of the HP assembly surrounding the sample chamber that happened as a result of full melting of capsules.

## 4.4.4.3 Discussion of the mechanism of single crystal growth of B$_{28}$

Growth of crystals from the liquid state plays a dominant role for many technical applications and in basic research. Adverse aspects of the crystal growth from HT solutions are the low growth rate and the low crystal yield, especially if the slope of the liquidus curve is large [18]. Growth processes are characterized by a slow lowering of the temperature in order to force the crystallization. In technology the precise knowledge of the liquidus curve is required in order to avoid either a spontaneous crystallization or dissolving of the seed crystals in synthesis from HT solutions. The application of a suitable solvent or nonstoichiometric composition is capable of reducing a high growth temperature or pressure, so that growth close to thermal equilibrium may yield crystals with a high structural perfection [18]. Our choice of solvents was based on general principles: high solubility of the component of interest, low chemical reactivity between the material and solvent, a possibility to easily remove the solvent after the growth process, its high purity and low toxicity. Dealing with crystal growth at high pressure, we did not have the HP phase diagrams of the systems we explored, as well as we did not introduce seeds and relied on a spontaneous crystallization. In choice of the temperature we oriented on HP melting curves known for the solvents of choice [12].

Single crystal growth can be performed by several methods, for example by controlling the speed of crystallization, degree of oversaturation or overcooling, etc. In one of the experiments we checked if a gradual temperature decrease affects the size of grown single crystals. In the experiment S4390 a mixture of β-B and 1.5 at.% of Pt was loaded into an Au capsule (see Table 4.4.3.1). At 12 GPa the sample was heated at temperature of ~1723 K for 2 min. Then, the temperature was decreased during 18 minutes to ~1023 K and after the sample was quenched. After treatment of the synthesized sample in acids mixture, we observed aggregates of single crystals of B$_{28}$. Such a "gradual temperature decrease" did not have any visible effect on the size of

single crystals in comparison with those grown only upon heating at the same temperature.

Growth of B$_{28}$ single crystals could be controlled by the amount of the boron-containing melt in the pressure chamber. Complete melting of the whole pressure chamber potentially depends on the amount of flux material. Series of synthesis experiments were carried out using different amounts of various metallic powders as fluxes (Table 4.4.3.1). Experiments S4439 and S4400 were conducted at 12 GPa and 1723 K using Au capsules and mixtures of granulated β-B with 5 at.% of Cu-additive and 20 at.% of Pt-additive, respectively (Table 4.4.3.1). The back scattered electron (BSE) images of polished surfaces of the S4390 and S4400 samples (Figs. 4.4.4.3.1 (a) and (b), respectively) show elongated crystals of various sizes up to tens of microns of B$_{28}$ surrounded by Cu-Au or Pt-Au matrixes. Such crystals could be found only in the inner parts of the capsules (at the boron-metal capsule interface).
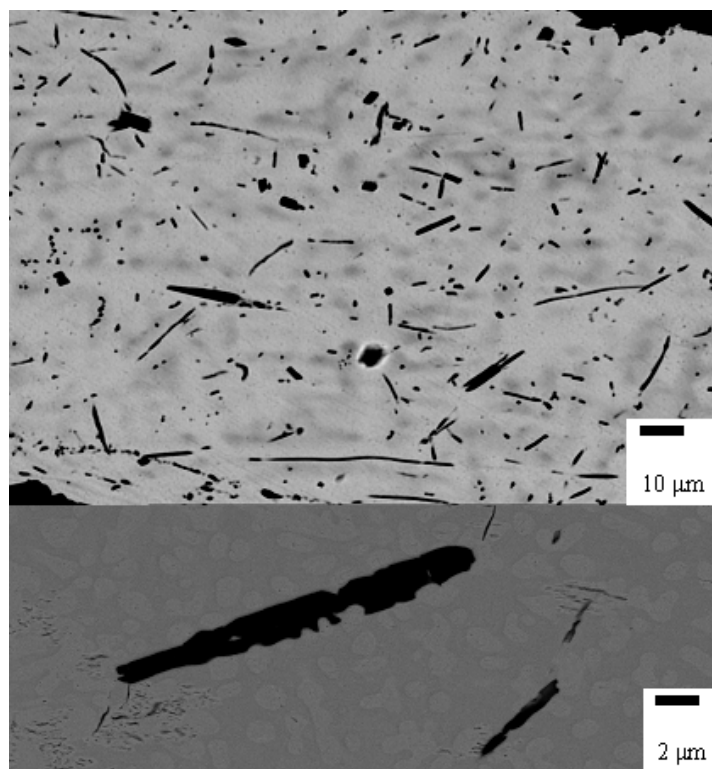


**Figure 4.4.4.3.1.** BSE image of polished surfaces of samples synthesized in Au capsules at 12 GPa and 1723 K with use of (a) 5 at.% of Cu-additive (experiment S4439, Table 4.4.3.1) and (b) 20 at.% of Pt-additive (experiment S4400, Table 4.4.3.1).

The rest of the samples (i.e. their inner parts that were not in direct contact with the capsules) was composed of granules of polycrystalline B$_{28}$. Their surface was covered by very thin, reddish, only a few microns long B$_{28}$ crystals with an irregular or a plate-like shape (the quality of these tiny crystals was not investigated). We believe that this observation, typical for almost all of our experiments, is imposed by a specific character of the B precursor we used. As we already mentioned, only granules (~50-100 μm in size) of pure β-B were available. We could not grind or mill them without a risk of contamination because of extreme hardness of the material, so that we used the granules as they were. It means that dissolution of boron in metals in sufficient amounts for spontaneous crystallization and formation of relatively big single crystals was reached only for the granules which were embedded into the capsules' walls at the capsule-sample boundary. The amount of metallic powders that surrounded the granules was likely insufficient to penetrate deep into the boron grains and cause their complete melting. Boron, only partially dissolved in metals in the inner parts of the samples, on cooling likely either precipitated on polycrystalline aggregates of B$_{28}$ formed due to the solid-solid transition within not molten granules, or formed numerous tiny crystallites described above. Although temperature was high enough to melt whole material in the capsule, only a part of it was actually molten. Potentially, not complete melting could be caused by the temperature gradient within the pressure chamber. However, usually the temperature gradient is estimated to be not more than 50 K across the sample [11], so that, taking into account that melting in the inner parts of the sample was also observed, we could eliminate problems related to the temperature gradient. In principle, it is possible to reach complete melting by overheating a sample. Indeed, in experiments conducted at higher temperatures a complete melting of a capsule was achieved (for example, the gold capsule in the experiment S4492 at ~2073 K and 12 GPa) and we succeeded in synthesis of larger crystals of orthorhombic B$_{28}$ with the length of over 100 μm. However, in such cases of complete melting of capsules chemical reactions with the materials of the assembly surrounding the capsule and samples are unavoidable. Thus, we can not be sure that the amount of melted Au and not a presence of another chemical compounds promotes B$_{28}$ crystal growth. In the future experiments a precaution should

be undertaken to find a refractory, non-reactive material to separate the capsule from its surrounding.

Based on our observations, we can suggest that mechanism of growth of B$_{28}$ single crystals may be similar to that of diamond growth from metallic solutions [19]. Assuming that phase relations of boron with Pt, Cu and Au remain similar to those under atmospheric pressure, we could expect that some amount of boron dissolves in metals: according to [14], several at.% of B could incorporate into Pt; solubility limit of B in Cu is less than 1 at.%, and there are indications that small amount of B could be dissolve in Au-melt as well. On cooling boron dissolved in metals crystallizes as the B$_{28}$ phase. It means that growth of B$_{28}$ crystals is controlled by the amount of B-containing liquid in the pressure chamber.

## 4.4.5 Conclusions

We presented and discussed a procedure of growing of single crystals of orthorhombic B$_{28}$ from metal solutions at high pressure high temperature conditions. Various (Cu, Au, Pt) capsules and solvent materials were tested. In all experiments we observed that B$_{28}$ crystals form from the boron-metal solution during cooling, thus, the mechanism of formation of HPHT boron may be similar to that of diamond growth [19]. A maximal size of the grown B$_{28}$ crystals of a very high quality was about 100 microns. It did not depend on the volume of the pressure chamber and the duration of heating. In our experiments the crystal size was likely imposed by the amount of the solution formed by the melted metallic flux and boron. Only use of Au did not lead to formation of borides. To increase the total yield of B$_{28}$ single crystals the search for less reactive solvents could be suggested.

## Acknowledgements

## References

[1]. B. Albert, H. Hillebrecht, Boron: Elementary Challenge for Experimenters and Theoreticians, Angew. Chem. Int. Ed. 48 (46) (2009) 8640-8668.

[2]. G. Will, K. Ploog, Crystal-Structure of I-Tetragonal Boron, Nature 251(1974) 406-408.

[3]. L.V. McCarty, J.S. Kasper, F.H. Horn, B.F. Decker, A.F. Newkirk, A New Crystalline Modification of Boron, J. Amer. Chem. Soc. 80 (1958) 2592.

[4]. B.F. Decker, J.S. Kasper, The Crystal Structure of a Simple Rhombohedral Form Boron, Acta Cryst. 12 (1959) 503-506.

[5]. D.E. Sands, J.L. Hoard, Rhombohedral Elemental Boron, **J.** Am. Chem. Soc., 79 (1957) 5582–5583.

[6]. Claude P. Talley, A new polymorph of boron, Acta Cryst. 13 (1960) 271-272.

[7]. R.H. Wentorf, Boron:Another form, Science 147 (1965) 49.

[8]. E.Yu. Zarechnaya, L. Dubrovinsky, N. Dubrovinskaia, N. Miyajima, Y. Filinchuk, D. Chernyshov, V. Dmitriev, Synthesis of an orthorhombic high pressure boron phase, Sci. and Technology of Adv. Mat. 9 (2008) 044209.

[9]. E.Yu. Zarechnaya, L. Dubrovinsky, N. Dubrovinskaia, Y. Filinchuk, D. Chernyshov, V. Dmitriev, N. Miyajima, A. El Goresy, H.F. Braun, S. Van Smaalen, I. Kantor, A. Kantor, V. Prakapenka, M. Hanfland, A.S. Mikhaylushkin, I.A. Abrikosov, and S.I. Simak, Superhard Semiconducting Optically Transparent High Pressure Phase of Boron, Phys. Rev. Lett. 102 (2009)185501.

[10]. A.R. Oganov, J. Chen, C. Gatti, Y. Ma, Y. Ma, C.W. Glass, Z. Liu, T. Yu, O.O. Kurakevych, V.L. Solozhenko, Ionic high-pressure form of elemental boron, Nature, 457 (2009) 863-867.

[11]. D.J. Frost , B.T. Poe, R.G. Trønnes, C. Liebske, A. Dubaa, D.C. Rubie, A new large-volume multianvil system , PEPI, 143–144 (2004) 507–514.

[12]. H. Schlosser, P. Vinet, J. Ferrante, Pressure dependence of melting temperature of metals, Phys. Rev. B, 40 (1989) 5929-5935.

[13]. S. Raju, E. Mohandas, and S.V. Raghunathan, The pressure derivative of bulk modulus of transition metals: an estimation using the method of model potentials and a study of the systematics, J. Phys. Chem. Solids 58 (1997) 1367-1373.

[14]. B. Predel, O. Madelung (Eds.), Phase Equilibria, Crystallographic and Thermodynamic Data of Binary Alloys: Ac-Au ... Au-Zr, Landolt-Börnstein, New Series IV/5a (1991), internet resource:DOI:10.1007/b20007; B. Predel, O. Madelung (Eds.) Phase Equilibria, Crystallographic and Thermodynamic Data of Binary Alloys: B-Ba ... C-Zr, Landolt-Börnstein, New Series IV/5b (1992), internet resource: DOI: 10.1007/b43647.

[15]. E.D. Whitney, R.F. Giese Jr., Reaction of Platinum and Boron under Pressure, Nature, 197 (1963) 1293.

[16]. H.M. Strong and F.P. Bundy, Fusion Curves of 4 Group-Viii Metals to 100,000 Atmospheres, Phys. Rev., 115 (1959) 278.

[17]. E.Yu. Zarechnaya, N. Dubrovinskaia, L. Dubrovinsky. Polarized Raman Spectroscopy of High Pressure Boron. High Press. Res. 29 4 (2009) 530-535.

[18]. Crystal Growth Technology. Edts. H.J. Scheel & P. Capper, Wiley-VCH Verlag, Weinheim, (2008) 505p.

[19]. M.A. Prelas, G. Popovici, L.K. Bigelow (Eds.), Handbook of industrial diamonds and diamond films, Marcel Dekker Inc., New York, 1998.

## 4.5   Pressure-Induced Isostructural Phase Transition in γ-B$_{28}$

E. Yu. Zarechnaya[1], N. Dubrovinskaia[2,3], R. Caracas[4], M. Merlini[5], M. Hanfland[6], Y. Filinchuk[6], D. Chernyshov[6], V. Dmitriev[6], L. Dubrovinsky[1]

[1]*Bayerisches Geoinstitut, Universität Bayreuth, 95440 Bayreuth, Germany;* [2]*Mineralphysik, Institut für Geowissenschaften, Universität Heidelberg, 69120 Heidelberg, Germany;* [3]*Lehrstuhl für Kristallographie, Physikalisches Institut, Universität Bayreuth, 95440 Bayreuth, Germany;* [4]*Centre National de la Recherche Scientifique, Ecole Normale Superieure de Lyon, Laboratoire de Sciences de la Terre, 46, allee d'Italie, 69364 Lyon cedex 07, France;* [5]*Dipartimento di Scienze della Terra, Universita degli Studi di Milano Via Botticelli 23, 20133 Milano, Italy;* [6]*ESRF, Boîte Postale 220, 38043 Grenoble, France*

Isostructural phase transformations (ISPhTs) are particular cases of isosymmetric transformations and include discontinuous isostructural transitions and crossovers. They are rare, intriguing phenomena in solids often associated with a significant volume collapse, giant magneto-elastic coupling, or negative thermal expansion.[1-5] So far ISPhTs were reported for heavy elements and their compounds with complex electronic and/or magnetic structures. We have studied the high-pressure boron phase[6-8] γ-B$_{28}$ by means of *in situ* Raman spectroscopy up to 105 GPa, single-crystal X-ray diffraction in diamond anvil cells above 65 GPa and first-principles calculations. The discontinuous behavior of the Raman modes and the abrupt changes in the compressional behavior of γ-B$_{28}$ are manifestations of the isostructural phase transformation at about 40 GPa. The combined experimental and *ab inito* theoretical analysis of the structural and vibrational properties of γ-B$_{28}$ suggest that the ISPhT under compression is due to the changes of the polarity of the covalent bonds between the boron atoms in the complex quasimolecular structure of γ-B$_{28}$.

Elemental boron and boron-rich compounds have been given a particular scientific and technological attention because of their specific physical properties: high melting temperatures, a wide energy band gap, high hardness, strong absorbance of neutrons, etc. The structures of these materials are based on icosahedral units as a common feature. Rhombohedral α-boron consists of only B$_{12}$ icosahedra. It does not show any phase transitions on compression to at least 80 GPa at ambient temperature. The arrangement of B$_{12}$ icosahedra in β-boron is complex and its structure contains partially occupied sites.[9,10] The β-boron is less compressible (the bulk modulus K$_{300}$=185-210 GPa) in comparison with α-boron (K$_{300}$=213-224 GPa).[11,12] The resistivity measurements[13] indicate a transformation from β-boron into yet unknown superconducting phase at about 160 GPa. At pressures above 8.5 GPa and temperatures higher than 1500 °C pure boron crystallizes as a phase with a *Pnnm* space group[6-8]. It contains 28 atoms in the unit cell (and will be called here γ-B$_{28}$). The structure consists of B$_{12}$ icosahedra and B$_2$ dumbbells linked covalently [6,7,14] (*Supplementary Materials*, Fig. S1). γ-B phase was demonstrated[7] to be stable at least to 30 GPa and 2000 K. However, experimental information about the high-pressure behavior of the γ-B$_{28}$ phase is so far limited. Here we fill in this gap and present the results of the high-pressure Raman spectroscopy study of γ-B up to 105 GPa and its single-crystal X-ray diffraction over 65 GPa (see *Supplementary Materials* for technical details).

The γ-B$_{28}$ gives very distinct and strong Raman spectra at ambient conditions[6,7,15] so that the Raman spectroscopy could be the most convenient and useful technique for investigation of the high-pressure behavior of this phase. Polarized Raman spectroscopy studies[15] allowed assigning vibration modes of γ-B$_{28}$ thus creating a basis for the present study. Some examples of Raman spectra of polycrystalline γ-B$_{28}$ collected at high pressure are presented in Fig. 4.5.1a. The pressure dependence of Raman modes (Fig.4.5.1b) can be demonstrated in terms of the mode-Grüneisen parameter, defined as $γ_{ωi} = -\partial \ln ω_i/\partial \ln V = -(B_0/ω_i)\partial ω_i/\partial P$, where $ω_i$ is the phonon frequency, $B_0$ is the bulk modulus (227 GPa at ambient conditions[7]), $V$ is the molar volume and $P$ is the pressure. According to the values of the mode-Grüneisen parameters, all observed Raman peaks could be divided into three groups (*Supplementary Materials*, Table S1). To the first group belongs the mode B$_{2g}$ at 319(3) cm$^{-1}$ for which the Grüneisen parameter (2.8) is

distinctly high. According to theoretical analysis (*Supplementary Materials*, Table S2) this mode is associated with tilts (rotations) around the *a* axis of the B$_{12}$ icosahedra. The second group of mode consists of weakly varying (γ=0.03-0.2) narrow bands in the frequency range 380 - 470 cm$^{-1}$. All these modes are assigned to vibrations of B$_{12}$ icosahedra (380, 388, 460 cm$^{-1}$) or both B$_{12}$ icosahedra and B$_2$ dumbbells (444, 470 cm$^{-1}$) along the unit cell axes (*Supplementary Materials*, Table S2). Note that similar behaviour of icosahedron and icosahedron-dumbbell vibrations were observed in α-boron,[16] in highly ordered pnictides (B$_{12}$As$_2$, B$_{12}$P$_2$),[17] and boron carbide (B$_4$C)[18]. The Grüneisen parameters of modes observed between 507 cm$^{-1}$ and 1200 cm$^{-1}$ (the third group) are in the range of 0.42 - 1.05. These bands arise mainly from intra-icosahedral vibrations, like breathing or rocking-stretching modes. Note that apparent changes in the shape of spectra in the 800 cm$^{-1}$ to 1000 cm$^{-1}$ region on compression to about 39 GPa (Fig. 4.5.1) are entirely due to differences in mode-Grüneisen parameters of the bands.
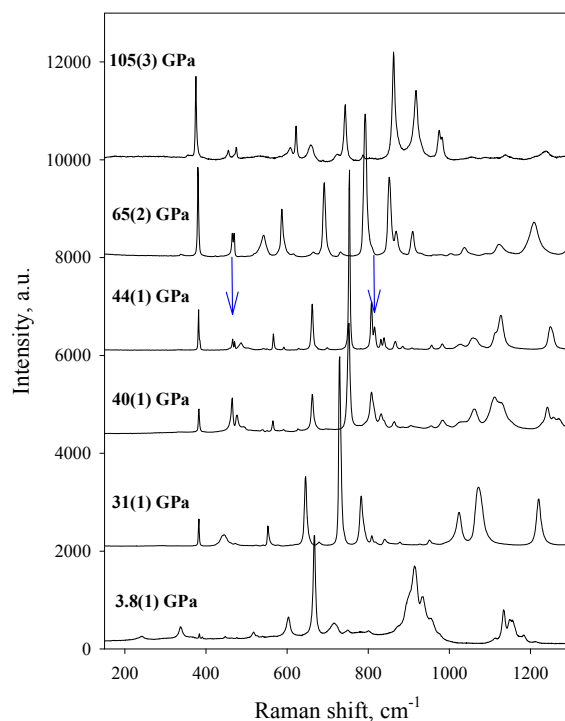


**Figure 4.5.1a.** Examples of Raman spectra of γ-B compressed in neon pressure transmitting medium in a diamond anvil cell. Arrows highlight some parts of the spectra which undergo rapid changes at pressure above 40 GPa.
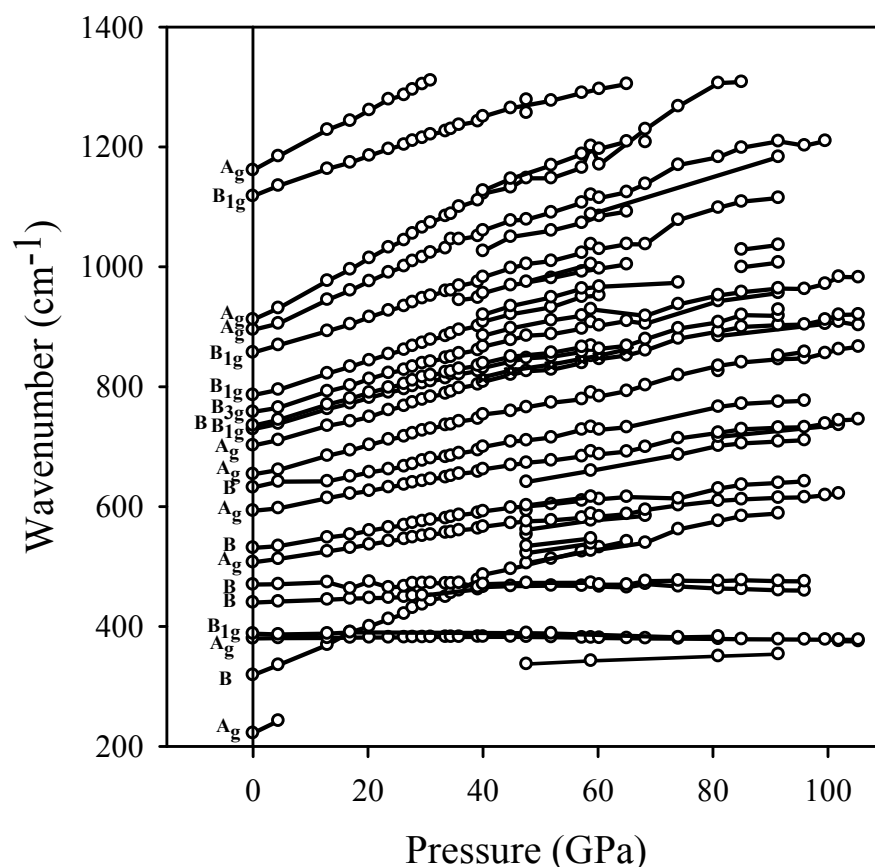
**Figure 4.5.1b.** Variation of the positions of Raman lines of γ-B as a function of pressure. Mode assignment at ambient conditions is given according to Zarechnaya et al.[9].

The observed high-pressure behaviour of Raman modes can be qualitatively related to the response of the γ-B$_{28}$ structure on compression. Indeed, rotations of B$_{12}$ icosahedra, or of the B$_{12}$ icosahedra and B$_2$ dumbbells around *b* and *c* axes (*Supplementary Materials*, Fig. S1, Table S2) require changes in the length of the shortest (i.e. strongest) B-B contacts between icosahedra and/or between an icosahedron and a dumbbell[7] and correspond to the modes with the smallest mode-Grüneisen parameters, while the mode which is most sensitive to the volume changes is associated with the rotation of B$_{12}$ icosahedra around the *a* axis and does not involve tension of the shortest interatomic contacts.

Most the Raman modes monotonically shift to higher wavenumbers with increasing pressure up to about 35 GPa. At pressures higher than 40 GPa in all three

independent experiments we observed an inflection in the modes behaviour (Fig. 4.5.1b, *Supplementary Materials*, Table S1). Under further compression to pressures about 40-45 GPa several broaden peaks split (Fig. 4.5.1a; although above ~40 GPa we detect up to 32 Raman modes in the spectra, the total number of modes was always less than 42 allowed in orthorhombic γ-B$_{28}$[15]). At the same pressure two modes (A$_g$ at 380 cm$^{-1}$ and B$_{3g}$ at 470 cm$^{-1}$) drastically change their behaviour and become soft with Grüneisen parameters of about -0.03 (Fig. 4.5.1; *Supplementary Materials*, Table S1, Fig. S2).

Phonon determination based on first-principles calculations show that the lowest six Raman modes (one A$_g$, one B$_{1g}$, two B$_{2g}$, and two B$_{3g}$) present pressure softening in perfect agreement with the experimental observations. They are lattice modes corresponding mainly to tilts of the B$_{12}$ icosahedra. In particular the behaviour of the lowest B$_{2g}$ mode is relevant as it hardens up to about 50 GPa and it softens beyond that pressure.

Laser annealing at 1500-1800 K at pressures above 40 GPa does not affect the Raman spectra and the changes are fully reversible on decompression suggesting that the orthorhombic B$_{28}$ may undergo a phase transition at high pressures. In order to test this hypothesis we have undertaken an intensive X-ray diffraction investigation of γ-B$_{28}$ under compression.

Being the fifth element in the Periodic Table, boron is a very weak X-ray scatterer. X-ray powder diffraction experiments on boron phases above 30 GPa are difficult[7,19] and could hardly provide even accurate lattice parameters. At the same time, single crystal studies allowed investigating the behaviour of lattice parameters of β-boron at pressure up to 100 GPa.[12] In three independent diamond anvil cell (DAC) experiments we compressed single crystals of γ-B$_{28}$ (grown in a multi-anvil apparatus in metallic fluxes[20]) to pressures over 65 GPa using He as a quasi-hydrostatic pressure transmitting medium. The collected X-ray diffraction data were sufficient in quality to refine both lattice parameters and atomic coordinates (see *Supplementary Materials* for experimental details; Table S3). Remarkably, the quality of the structural refinement based on the data collected in DACs was not worse than that based on the data obtained at ambient conditions (*Supplementary Materials*, Table S3).

Up to the highest pressure reached in this study (65 GPa) all observed reflections perfectly match the γ-B$_{28}$ (space group *Pnnm*) structure (*Supplementary Materials*, Table S3). However, the compressional behaviour of the material at pressures below and above about 40 GPa is considerably different (Fig. 4.5.2). It manifests in an abrupt increase of the stiffness of the structure (more than 20% increase of the bulk modulus) and in the relative softening along the *a* axis in comparison with the *c* and especially the *b* axes. There is a clear change in behaviour of the *b/a* ratio: it decreases monotonously to about 35 GPa and increases above 40 GPa (insert of Fig. 4.5.2). An extrapolation of molar volumes of low-pressure and high-pressure materials to ambient conditions gives a difference of about 3% (Fig. 4.5.2).
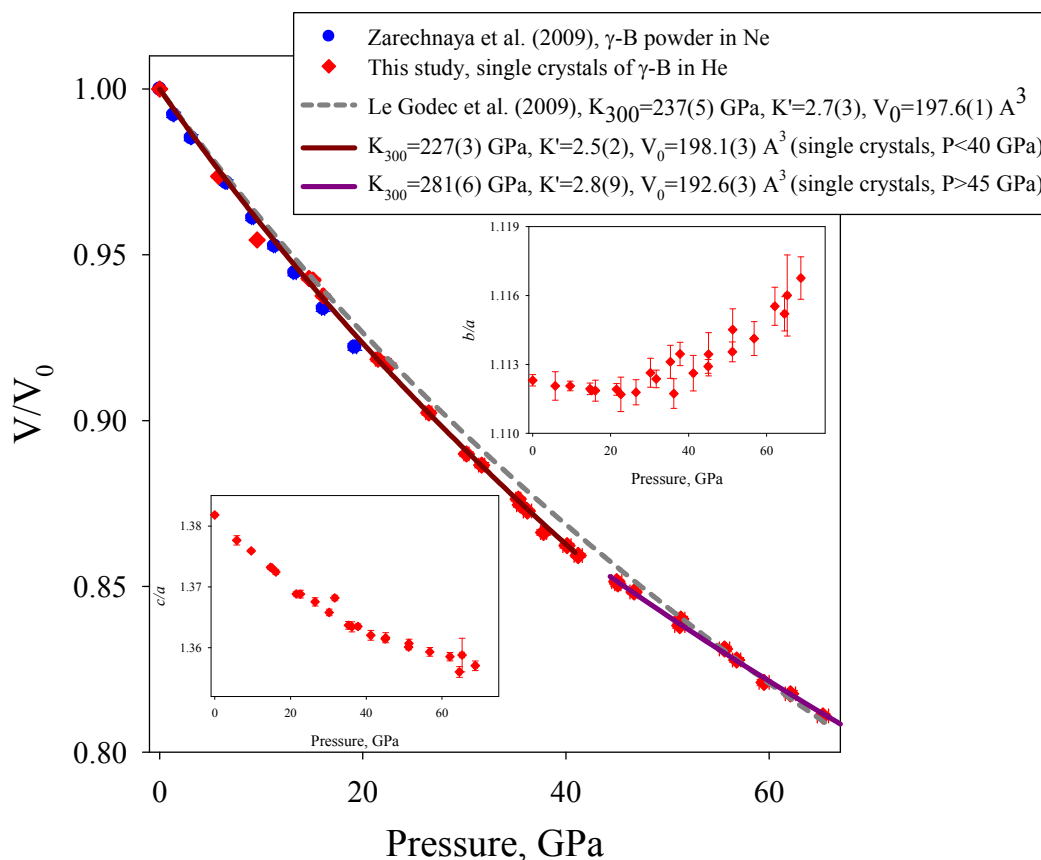


**Figure 4.5.2.** The relative unit cell volume of γ-B as a function of pressure (red diamonds – single crystal data from this study; blue circles – powder diffraction data[6]; lines are fits with the 3$^{rd}$ order Birch-Murnaghan (BM3) equation of state: dark-red for single crystal data below 40 GPa, dark-purple for single crystal data above 45 GPa, and dashed line as reported by Le Godec et al.[18] based on powder x-ray diffraction data to 70 GPa). Inserts show the variations of the ratios of the lattice parameters *c/a* and *b/a* as a function of pressure.

On compression up to 40 GPa the shortest bond lengths as well as the average distances between any atom and its neighbours ("atom's sphere radius" as defined in IVTON software[21]) homogeneously decrease; their compressibility are linear with value in the 0.019 – 0.024 GPa$^{-1}$ range (*Supplementary Materials*, Fig. S3). The volume of the B$_{12}$ icosahedra also decreases smoothly to 40 GPa (*Supplementary Materials*, Fig. S4). However the bulk modulus of this polyhedron (285 GPa) is significantly higher than the bulk modulus of the bulk material (227 GPa) confirming a molecular-solid-like behaviour with inter-icosahedral bonding weaker than intra-icosahedral ones. At pressures above 40 GPa the compressibility of the spheres around the B1 and B4 atoms (see *Supplementary Materials*, Fig. S1 for designation of atoms) does not change (these two atoms are not involved into the shortest inter-icosahedral contacts or into the contacts of the B$_2$ dumbbells and the B$_{12}$ icosahedra). Contrary, the atoms involved in intra- icosahedral bonding (labelled B3) or in bonding between the B$_{12}$ icosahedra and the B$_2$ dumbbells (labelled B2 and B5) show pronounced changes in the compressional behaviour. In parallel the B$_{12}$ icosahedra become much more incompressible, exhibiting a 1/3 increase in the bulk modulus (*Supplementary Materials*, Fig. S4).

Consequently, both the Raman spectroscopy and the single crystal X-ray diffraction studies reveal the existence of *two states* of γ-B$_{28}$with a pronounced difference in their vibrational and compressional properties. The abrupt change of the properties occurs at pressures ~40 GPa. However, neither the symmetry nor the structure change was detected in this pressure range. We conclude, therefore, that B$_{28}$ undergoes an *isostructural* phase transformation.

Isostructural phase transformations are relatively exotic phenomena. They were reported for a few elements, in particular in Ce (the first well-known example of the isostructural transition[1], see Ref. 22 for review) at high pressures, Zr[23], Os[24]. However, established cases of the ISPhTs are related to the elements or compounds containing elements with the variable chemical valence due to fully or partially free *d-* or/and *f-*electronic shells (for example, SmS[25], EuCo$_2$P$_2$[26], rare-earth chalcogenides[27] and pnictides, see Ref. 28 for review), or/and materials which undergo magnetic or spin transitions (for example MnO[29] or YCo$_5$[2]). Boron is an element of the second row of the Periodic Table and the conventional mechanisms of the ISPhT in its crystal structure are

highly unlikely (indeed, theoretical calculations[7,8] do not indicate any significant changes of band structure of γ-B$_{28}$ at least to 100 GPa). At the same time γ-B$_{28}$ is a quasimolecular material. The detailed low-temperature single-crystal X-ray diffraction study[14] revealed the strong polar-covalent bonding with an electron density excess at B2 and B4 atoms (they belong to the B$_{12}$ icosahedra) and an electron density deficit at B5 atoms (which form B$_2$ dumbbells). This suggests that the ISPhT in γ-B$_{28}$ can be a result of changes in the electron density distribution between boron atoms and/or bonds or, in other words, changes in the character of chemical bonding. For compounds with the polar-covalent bonding, the splitting of the IR longitudinal and transversal optical (LO-TO) phonon modes can be used as a measure of the degree of the charge transfer,[8,9,30] which can be characterised by the generalized Lyddane-Sachs-Teller (LST) parameter

$\xi = \prod\limits_{i}^{n} \left(\omega_i^{LO} / \omega_i^{TO}\right)^2$. Using calculated values of frequencies for all IR active modes

(*Supplementary Materials*) at different pressures (Fig. 4.5.3) we found that above 50 GPa, in strict similarity with experimental data on changes in Raman spectra and compressional behaviour, the LST parameter changes its pressure dependence.
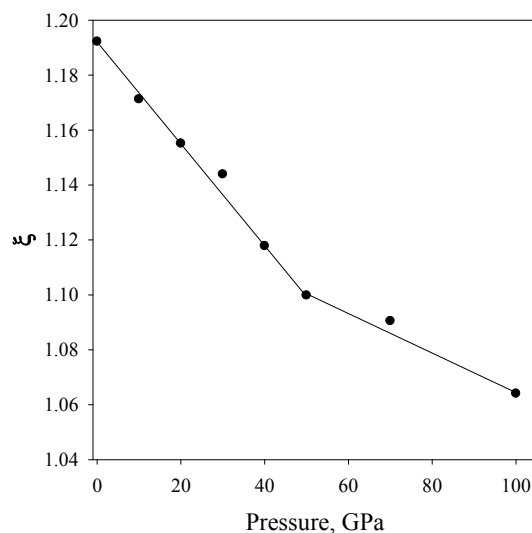


**Figure 4.5.3.** The generalized Lyddane-Sachs-Teller parameter $\xi = \prod\limits_{i}^{n} \left(\omega_i^{LO} / \omega_i^{TO}\right)^2$ of γ-B

($\omega_i^{LO}$ and $\omega_i^{TO}$ are calculated frequencies of longitudinal and transversal optical IR active modes, see *Supplementary Materials*) as a function of pressure. The decrease of ξ with pressure indicates that the covalent bonding in γ-B$_{28}$ becomes less polar under compression.

This result strengthens our assignment of the isostructural phase transformation in γ-B$_{28}$ as due to alteration the polarity of the covalent bonding between the boron atoms in the complex quasimolecular structure.

Boron-rich carbides, nitrides, oxides, and borides of light elements with polar covalent and/or partially ionic bonding represent a large group of materials with prospective applications due to a number of unusual and potentially useful properties.[9,17] Our finding of the ISPhT in γ-B$_{28}$ suggests that the same or similar mechanism, involving rapid pressure- or chemically-induced changes of chemical bonding, could drive isostructural transformations in other boron-rich phases as well.

## References

1. Bridgman, P. W. The compressibility and pressure coefficient of resistance of ten elements. *Proc. Am. Acad. Arts Sci.* **62**, 207–226 (1927).

2. Rosner, H., Koudela, D., Schwarz, U., Handstein, A., Hanfland, M., Opahle, I., Koepernik, K., Kuz'min, M. D., Müller, K.-H., Mydosh, J. A., Richter, M. Magneto-elastic lattice collapse in YCo$_5$. *Nature Physics* **2**, 469 (2006).

3. Lee, S., Pirogov, A., Kang, M., Jang, K.–H, Yonemura, M., Kamiyama, T., Cheong, S.-W., Gozzo, F., Shin, Na., Kimura, H., Noda, Y., Park, J.-G. Giant magneto-elastic coupling in multiferroic hexagonal manganites. *Nature* **451**, 805-808 (2008).

4. Long, Y. W., Hayashi, N., Sait, T., Azuma, M., Muranaka, S., Shimakawa, Y. Temperature-induced A–B intersite charge transfer in an A-site-ordered LaCu$_3$Fe$_4$O$_{12}$ perovskite. *Nature* **458**, 60-64 (2009).

5. Kuznetsov, A., Dmitriev, V., Bandilet, O., Weber, H.P. High-temperature fcc phase of Pr: negative thermal expansion and intermediate valence state. *Phys. Rev.B* **68**, 064109 (2003).

6. Zarechnaya, E. Yu., Dubrovinsky, L., Dubrovinskaia, N., Miyajima, N., Filinchuk, Y., Chernyshov, D., and Dmitriev, V. Synthesis of an orthorhombic high pressure boron phase. *Sci. Thechnol. Adv. Mater* **9**, 0044209 (2008).

7. Zarechnaya, E. Yu., Dubrovinsky, L., Dubrovinskaia, N., Filinchuk, Y., Chernyshov, D., Dmitriev, V., Miyajima, N., El Goresy, A., Braun, H. F., Van Smaalen, S., Kantor, I., Kantor, A., Prakapenka, V., Hanfland, M., Mikhaylushkin, A. S., Abrikosov, I. A., Simak, S. I. Superhard semiconducting optically transparent high pressure phase of boron. *Phys. Rev. Lett.* **102**, 185501 (2009).

8. Oganov, A. R., Chen, J., Gatti, C., Ma, Y., Ma, Y., Glass, C. W., Liu, Zh., Yu, T., Kurakevych, O. O. & Solozhenko, V. L. Ionic high-pressure form of elemental boron, *Nature* **457**, 863-867 (2009); Addendum: *Nature* **460**, 292 (2009).

9. B. Albert, B., Hillebrecht, H. Boron–elementary challenge for experimenters and theoreticians. *Angew. Chem. Int. Ed.* **48**, 2-31 (2009).

10. Ogitsu, T., Gygi, F., Reed, J., Motome, Y., Schwegler, E., Galli, G. Imperfect crystal and unusual semiconductor: Boron, a frustrated element. *J. Am. Chem. Soc.* **131**, 1903–1909 (2009).

11. Nelmes, R. L., Loveday, J. S., Allan, D. R., Besson, J. M., Hamel, G., Grima, P. and Hull, S. Neutron- and x-ray-diffraction measurements of the bulk modulus of boron. *Phys. Rev. B* **47**, 7668 (1993).

12. Sanz, D. N., Loubeyre, P., and Mezouar, M. Equation of state and pressure induced amorphization of *β*-boron from x-ray measurements up to 100 GPa. *Phys. Rev. Lett.* **89**, 245501 (2002).

13. Eremets, M. I., Stuzhkin, V. V., Mao, H.-k. and Hemley, R. J. Superconductivity in boron. *Science* **293**, 272 (2001).

14. Mondal, S., van Smaalen, S., Filinchuk, Y., Chernyshov, D., Dmitriev, V., Zarechnaya, E. Yu., Dubrovinskaia, N., Dubrovinsky, L. Experimental study of electron density distribution in high-pressure boron γ-B$_{28}$ phase. *Angewante Chem. Int. Ed.*, submitted (2010).

15. E. Yu. Zarechnaya, N. Dubrovinskaia, L. Dubrovinsky, Polarized Raman spectroscopy of high-pressure orthorhombic boron phase, *High Pressure Research* **29**, 530-535 (2009).

16. Vast, N., Baroni, S., Zerah, G., Besson, J. M., Polian, A., Grimsditch, M., and Chervin, J. C. Lattice dynamics of icosahedral α-boron under pressure, *Phys. Rev. Lett.* **78**, 693–696 (1997).

17. Polian, A., Ovsyannikov, S. Y., Gauthier, M., Munsch, P., Chervin, J. C., Lemarchand, G. Boron and boron-rich solids at high pressures. *Proc. of the 41st Course High Pressure Crystallography Eriche* v. 2, 437-445 (2009).

18. Tallant, D. R., Aselage, T. L., Campbell, A. N. and Emin, D. Boron carbide structure by Raman spectroscopy. *Phys. Rev. B* **40**, 5649 (1989).

19. Le Godec, Y., Kurakevych, O. O., Munsch, P., Garbarino, G., Solozhenko, V. L. Equation of state of orthorhombic boron, γ-B$_{28}$. *Solid State Commun.* **149**, 1356 (2009).

20. Zarechnaya, E. Yu., Dubrovinskaia, N., Dubrovinsky, L., Filinchuk, Y., Chernyshov, D., Dmitriev, V. Growth of single crystals of B$_{28}$ at high pressures and high temperatures. *J Crystal Growth*, in press, (2010).

21. Žunić, T. B., Vicković, I., IVTON - program for the calculation of geometrical aspects of crystal structures and some crystal chemical applications. *J. Appl. Cryst.* **29**, 305-306 (1996).

22. Johansson, B., Li, S. Itinerant f-electron elements, *Philosophical Magazine* **89**, 22, 1793-1799 (2009)

23. Akahama, Y., Kobayashi, M., Kawamura, H. High-pressure X-ray diffraction study on electronic *s-d* transition in zirconium. *J. Phys. Soc. Japan* **60**, 3211-3214 (1991).

24. Occelli, F., Farber, D. L., Badro, J., Aracne, C. M., Teter, D. M., Hanfland, M., Canny, B., Couzinet, B. Experimental evidence for a high-pressure isostructural phase transition in osmium. *Phys. Rev. Letters* **93**, 095502 (2004).

25. Chatterjee, A., Singh, A. K., Jayaraman, A. Pressure-induced electronic collapse and structural changes in rare-earth monochalcogenides. *Phys. Rev. B* **6,** 2285–2291 (1972).

26. Chefki, M., Abd-Elmeguid, M. M., Micklitz, H., Huhnt, C., Schlabitz, W., Reehuis, M., Jeitschko, W. Pressure-induced transition of the sublattice

magnetization in EuCo$_2$P$_2$: change from local moment Eu (4$f$) to itinerant Co(3$d$) magnetism. *Phys. Rev. Letters* **80**, 802 (1998).

27. Caracas R, Gonze X. Structural, electronic, and dynamical properties of calaverite AuTe$_2$ under pressure*, Phys. Rev. B* **69**, 144114 (2004).

28. Svane, A., Strange, P., Temmerman, W. M., Szotek, Z., Winter, H., Petit, L. Pressure-induced valence transitions in rare earth chalcogenides and pnictides, *Phys. Stat. Sol. (b)* **223**, 105 (2001).

29. Yoo, C. S., Maddox, B., Klepeis, J.-H. P., Iota, V., Evans, W., McMahan, A., Hu, M. Y., Chow, P., Somayazulu, M., Häusermann, D., Scalettar, R. T., Pickett, W. E. First-order isostructural Mott transition in highly compressed MnO, *Phys. Rev. Letters* **94**, 115502 (2005).

30. Kittel, C. *Einführung in die Festkörperphysik*. 9th ed., R. Oldenbourg (München, 1991).

## Supplementary Materials

Methods

Single crystals and polycrystalline aggregates of $\gamma$-$B_{28}$ were grown as described in our previous publications (see Refs. 5, 6, 19).

*Diamond anvil cell experiments*

In different runs the sample was clamped between diamond anvils with culets of 300 μm, 250 μm, or 120 μm in diameter. Rhenium (in the Raman spectroscopy experiments) or steel (in single crystal X-ray diffraction experiments) gaskets were indented to the thickness of about 50 μm and holes with a diameter of 100 μm or 80 μm were drilled in the center. Small isometric pieces of the high-pressure boron phase synthesized in a multi-anvil apparatus were loaded into the holes along with ruby balls served as pressure markers. As a pressure transmitting medium Ne or He were loaded at 1.4 kbar (all single crystal X-ray diffraction experiments were performed in He pressure medium). One- and double-side laser annealing of samples compressed in Ne pressure medium at pressures above 20 GPa at temperatures up to 2000 K was conducted at BGI or at ESRF.

*Raman spectroscopy*

Raman spectroscopy studies were done on single crystals (with characteristic dimensions of ~5x5x25 μm$^3$) and polycrystalline aggregates of the $B_{28}$ phase. Measurements were performed with LabRam and Dilor XY (DILOR GmbH) systems with a resolution better than 2 cm$^{-1}$. The 632.8 nm line of a He-Ne laser and 514 nm of an Ar laser were used for an excitation with a power at the sample position of 15 mW to 50 mW. The positions of Raman peaks were determined by processing experimental data using PeakFit© v4.12 software.

*Single-crystal diffraction:*

Crystals with a size of about 7 μm x 7 μm x 30 μm size were selected and measured at ID09a at the European Synchrotron Radiation Facility (ESRF). Diffraction data were

collected at 293 K using the MAR555 Image Plate detector, radiation with a wavelength of 0.4143 Å, and the crystal-to-detector distance of 399 mm. 120 frames in the omega scanning range of -30 - +30 degree were collected (0.5 deg scanning step size) with exposure time of 1 sec. The data were processed using the Crysalis software (Oxford Diffraction (2006) Crysalis RED, version 1.171.31.8. Oxford Diffraction Ltd., Abingdon, Oxfordshire). Crystal structure refinements on integrated intensities were carried out with Jana2006 software (Petricek, V., Dusek, M., and Palatinus, L. (2006) Jana2006. The crystallographic computing system. Institute of Physics, Praha, Czech Republic).

*Ab initio calculation*

We performed first-principles calculations using the density-functional theory and density-functional perturbation theory formalisms as implemented in the ABINIT code (Gonze X, et al., First-principles computation of material properties: the ABINIT software project. Comp. Mater. Science 25, 478-492 (2002); Gonze, X., Rignanese, G.-M. & Caracas, R. First-principle studies of the lattice dynamics of crystals, and related properties, Z. Kristallogr., 220, 458–472 (2005b)). We employed a 6x6x6 regular grid of high-special *k* points (Monkhorst, H.J., Pack, J.D. Special points for Brillouin zone integrations. Phys Rev B 13, 5188-5192, (1976)) and a kinetic-energy cut-off of 30 Ha (1Ha=27.2116 eV). These ensured a precision of the order of 1 mHa in energy and better than 1 GPa in pressure. The calculations were performed on the JADE machine of CINES under the grant stl2816.
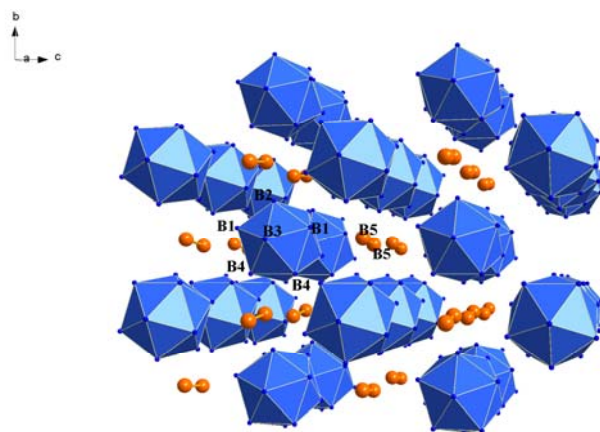


**Fig. S1.** Structure of γ-B (atom labels are according to Ref. 6).
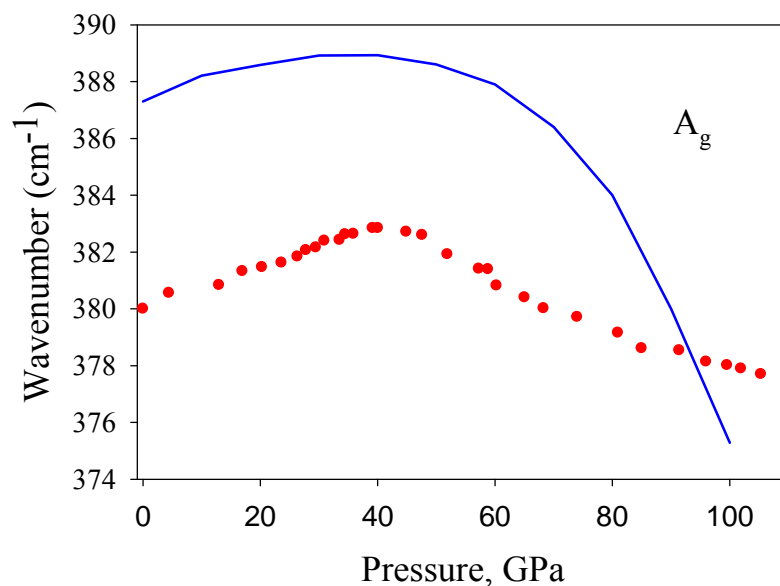
**Fig. S2.** Example of the measured (red dots) and calculated (blue line) Ag Raman mode as a function of pressure.
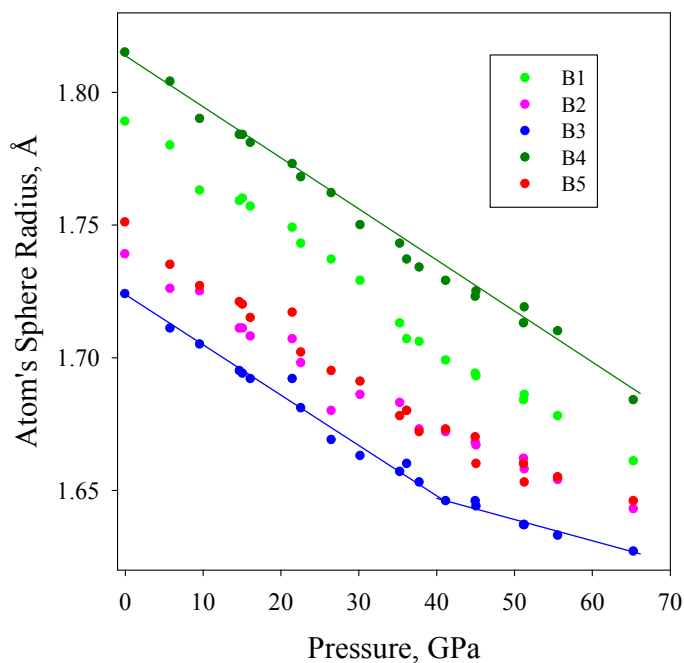


**Fig. S3.** The average distance of the atom from its neighbours ("sphere radius", as defined in IVTON software, see T. Balic Zunic, I. Vickovic, J. Appl. Cryst. 29, 305-306, 1996) as a function of pressure. Continues lines for B3 and B4 atoms are guides for eyes.
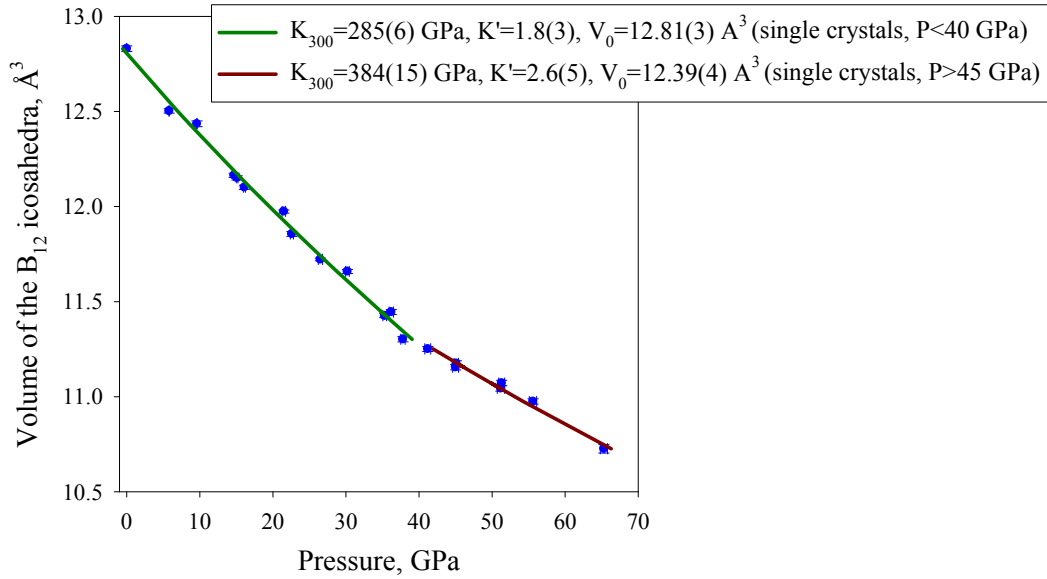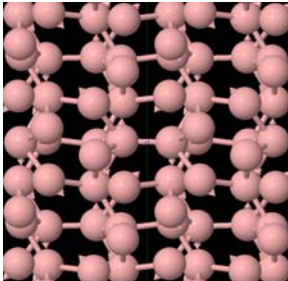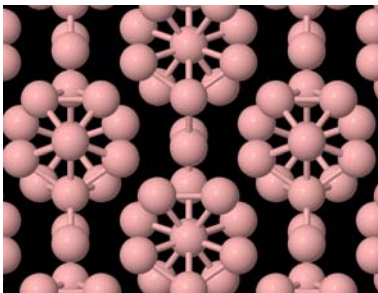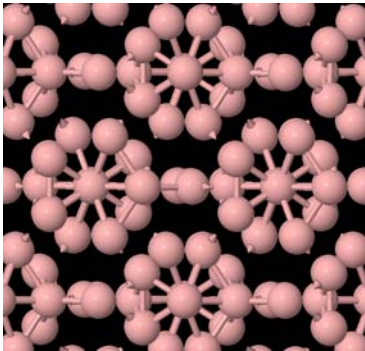
**Fig. S4.** Volume of the B$_{12}$ icosahedra as a function of pressure (blue dots). The polyhedron volumes were calculated in IVTON program (T. Balic Zunic, I. Vickovic, J. Appl. Cryst. 29, 305-306, 1996) Lines are fits with the 3$^{rd}$ order Birch-Murnaghan (BM3) equation of state: dark-green for single crystal data below 40 GPa, dark-red for single crystal data above 45 GPa.
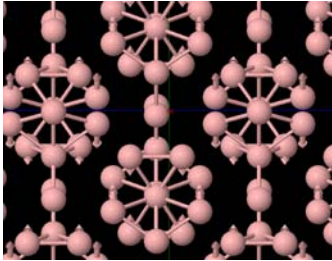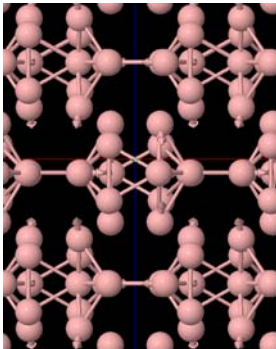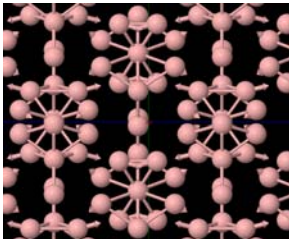
**Table S1.** Assignment of experimental (Ref. 14) and theoretical phonon frequencies at ambient conditions with experimentally determined mode-Grueneisen parameters ($\gamma_{exp}$).

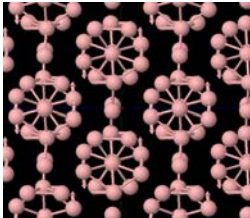| | | **Experiment** | | **Theory** | |
|---|---|---|---|---|---|
| $\omega_{exp}$(cm$^{-1}$) | Assignment | $\gamma_{exp}$ below 39 GPa | $\gamma_{exp}$ above 39 GPa | $\omega_{th}$(cm$^{-1}$) | Assignment |
| 217(2) | B$_{2g}$, B$_{3g}$ | | | | |
| 222(2) | A$_g$ | | | | |
| 319(3) | B$_{2g}$,B$_{3g}$* | 2.76 | 1.04 | 303 | B$_{2g}$ |
| 380(1) | A$_g$ | 0.07 | -0.03 | 387 | A$_g$ |
| 388(2) | B$_{1g}$ | 0.17 | | 389 | B$_{3g}$ |
| 440(2) | B$_{2g}$, B$_{3g}$ | 0.20 | -0.02 | 454 | B$_{3g}$ |
| 460(2) | B$_{1g}$* | | | 464/475 | B$_{3g}$/B$_{1g}$ |
| 470(2) | B$_{2g}$, B$_{3g}$ | 0.03 | | 464/475 | B$_{3g}$/B$_{1g}$ |
| 507(2) | A$_g$ | 0.65 | 0.34 | 536 | A$_g$ |
| 531(2) | B$_{2g}$, B$_{3g}$ | 0.68 | | 537 | B$_{2g}$ |
| 593(3) | A$_g$ | 0.67 | 0.41 | 611 | A$_g$ |
| 632(2) | B$_{2g}$, B$_{3g}$ | 0.53 | 0.42 | 585/575 | B$_{2g}$/B$_{3g}$ |
| 654(2) | A$_g$ | 0.84 | 0.47 | 687 | A$_g$ |
| 686(3) | B$_{1g}$,B$_{2g}$,B$_{3g}$* | | | 658 | B$_{1g}$ |
| 702(3) | A$_g$* | 0.85 | 0.50 | 732 | A$_g$ |
| 712(3) | B$_{2g}$, B$_{3g}$ | | | 714/719 | B$_{3g}$/B$_{2g}$ |
| 729(2) | B$_{1g}$ | 0.78 | 0.40 | 726 | B$_{1g}$ |
| 735(2) | B$_{1g}$,B$_{2g}$,B$_{3g}$* | 0.79 | 0.42 | 735 | B$_{2g}$ |
| 758(2) | B$_{3g}$ | 0.82 | 0.45 | 765 | B$_{3g}$ |
| 786(2) | B$_{1g}$ | 0.87 | 0.54 | 781,784 | B$_{1g}$,B$_{1g}$ |
| 857(3) | B$_{1g}$ | 0.81 | 0.52 | 862 | B$_{1g}$ |
| 878(2) | B$_{1g}$,B$_{3g}$* | | | 884 | B$_{3g}$ |
| 895(2) | A$_g$ | 1.05 | 0.55 | 887 | A$_g$ |
| 912(2) | A$_g$ | 1.26 | 0.66 | 920 | A$_g$ |
| 929(2) | A$_g$ | | | 970? | A$_g$ |
| 952(2) | B$_{2g}$,B$_{3g}$* | | | 959 | B$_{2g}$ |
| 1095(2) | B$_{1g}$,B$_{2g}$,B$_{3g}$* | | | | |
| 1118(2) | B$_{1g}$ | 0.98 | 0.40 | 1118 | B$_{1g}$ |
| 1138(2) | B$_{1g}$ | | | 1138 | B$_{1g}$ |
| 1161(2) | A$_g$ | 0.42 | | 1189 | A$_g$ |
| 1189(2) | A$_g$ | | | 1194 | A$_g$ |
| 1218(2) | A$_g$ | | | | |

*Peaks which are visible also in forbidden scattering geometries (Ref. 14).

**Table S2.** Calculated Raman active modes of γ-B at 0 GPa.

| Assignment | $\omega_{calc}$ (cm$^{-1}$) | Description |
|---|---|---|
| $A_g$ | 387 | The $B_6$ half-caps move up and down and the whole $B_{12}$ ball tilts around the $c$ axis  |
| $A_g$ | 536 | $B_2$ molecules tilt around the $c$ axis; slight participation of the $B_{12}$ balls that tilt much less |
| $A_g$ | 611 | Breathing mode of the $B_{12}$ balls |
| $A_g$ | 687 | Breathing mode of the $B_{12}$ balls |
| $A_g$ | 732 | Tilt of $B_2$ assoaciated with a movement of the B atoms from the sides of the $B_{12}$ balls, looking like a dangling bond; the B atoms from the $B_{12}$ that move are the furthsest apart from $B_2$ |
| $A_g$ | 770 | Breathing mode of the $B_{12}$ balls |
| $A_g$ | 811 | Breathing mode of the $B_{12}$ balls; here the B atoms from the side, the ones that form a bond perpendicular to the $B_2$-$B_{12}$ plane participate to the motion  |
| $A_g$ | 887 | Breathing mode of the $B_{12}$ balls |
| $A_g$ | 920 | Breathing mode of the $B_{12}$ balls  |
| $A_g$ | 970 | Breathing mode of the $B_{12}$ balls |
| $A_g$ | 1119 | Tilt of the $B_2$ molecule associated with a displcement of the two B atoms from the $B_{12}$ balls situated closeste ot the $B_2$ molecules along the $b$ axis |
| $A_g$ | 1194 | Breathing-like mode of the $B_{12}$ balls dominated by the movement of the apex atoms (these are the only ones that really move) |

| | | |
|---|---|---|
| **B₁g** | **475** | Tilts of the B₁₂ balls around the *c* axis |
| **B₁g** | **554** | Tilts of the B₂ molecules |
| **B₁g** | **658** | Vibration corresponding to half the B₁₂ balls vibrating aginast the other half along the *b* axis  |
| **B₁g** | **726** | Breathing mode of the B₁₂ balls |
| **B₁g** | **781** | Breathing mode of the B₁₂ balls; each half-cap breathes indepedently  |
| **B₁g** | **784** | Breathing mode of the B₁₂ balls; each half-cap breathes indepedently; the movement has an important *a* component, the sizes of the half-caps rotating around the z axis |
| **B₁g** | **793** | Breathing mode of the B₁₂ balls; dominated by a tilt of the B-B bond between the B₁₂ cages, in the (010) plane |
| **B₁g** | **862** | Breathing mode of the B₁₂ balls; B₂ do not participate |
| **B₁g** | **906** | Dominated by B₂ extension mode with some smaller participaton from the breathing of B₁₂ cages from the B2 side bonds paralle to the *c* axis |
| **B₁g** | **979** | Breathing mode of the B₁₂ cages, with lateral extension in the (100) planes  |
| **B₁g** | **1118** | Tilt of the B₂ molecule associated with a displcement of the two B atoms from the B₁₂ balls situated closeste ot the B₂ molecules along the *b* axis |
| **B₁g** | **1189** | Breathing-like mode of the B₁₂ balls dominated by the movement of the apex atoms (these are the only ones that really move) |
| **B₂g** | **303** | Tilts (=rotations) of the B₁₂ cages along the x axis |
| **B₂g** | **454** | Titls (rotations) of the B12 cages and of the B₂ molecules. The B₁₂ cages rotate around the *a* axis, while the B₂ molecules have a componenet along the *b* axis |
| **B₂g** | **537** | Tilts of the B₁₂ cages around the *b* axis |

| | | |
|---|---|---|
| | |  |
| $B_{2g}$ | 585 | Tilts of the $B_{12}$ cages around the *a* axis |
| $B_{2g}$ | 719 | Shear-like mode of the $B_{12}$ cages; such that each half of the cage tilts around the *b* axis producing a sheared final $B_{12}$ cage  |
| $B_{2g}$ | 735 | Shear-like mode of the $B_{12}$ cages; the tilt system is slightly different than from the previous mode; there are two subunits within each half that tilt in anti-phase  |
| $B_{2g}$ | 771 | The apex of the $B_{12}$ atoms along the X axis and the $B_2$ molecules vibrate around the *b* axis |
| $B_{2g}$ | 880 | Dominated by a tilt system of the $B_{12}$ apex against the $B_2$ molecules |
| $B_{2g}$ | 959 | Shear mode of the $B_{12}$ cages, associated with a tilt of the half-caps along the *b* axis |
| $B_{3g}$ | 389 | Tilt mode of the $B_{12}$ cages around the *b* axis |
| $B_{3g}$ | 403 | Tilt of the $B_2$ molecules with a sight participation from the $B_{12}$ unit that tilt as well |
| $B_{3g}$ | 464 | Another tilt of both $B_{12}$ and $B_2$ around the *a* axis |
| $B_{3g}$ | 575 | Shear mode of the $B_{12}$ cages; half-caps vibrate against the other half with a tilt around the *b* axis |
| $B_{3g}$ | 714 | Double shear of the $B_{12}$ cages; the mode is dominated by the $B_2$ bond parallel to the *c* axis |
| $B_{3g}$ | 765 | Breathing mode of the $B_{12}$ cages  |
| $B_{3g}$ | 810 | Breathing mode of the $B_{12}$ cages, associated with a shear due to differential displacement in the (100) plane soft the different B of $B_{12}$ cages |
| $B_{3g}$ | 884 | Breathing mode of the $B_{12}$ cages, associated with a shear due to differential displacement along the *a* axis of the different B of $B_{12}$ cages; dominated by lateral displacement of the apex atoms |
| $B_{3g}$ | 929 | Complex breathing mode of the $B_{12}$ cage |

**Table S3.** Structural parameters of B$_{28}$ phase (P$nnm$, Z=28) as revealed by single crystal diffraction experiments in diamond anvil cells at high-pressures.

| Run | Pressure, GPa | Lattice parameters, Å | | | Atomic coordinates | | | | | R$_1$(%) wR$_2$(%) |
|---|---|---|---|---|---|---|---|---|---|---|
| | | a | b | c | B1 8h | B2 4g | B3 4g | B4 8h | B5 4g | |
| B4_1 | 16.1(2) | 4.9554(3) | 5.5097(8) | 6.8011(6) | 0.1540(5) 0.5927(7) 0.7902(5) | 0.6498(7) 0.7264(11) 0.5 | 0.3358(7) 0.5082(9) 0.0 | 0.8395(5) 0.7188(7) 0.8731(5) | 0.6698(7) 0.9803(10) 0.0 | 7.57 8.07 |
| B4_2 | 22.6(2) | 4.9231(4) | 5.4720(14) | 6.7388(10) | 0.1545(5) 0.5920(7) 0.7898(5) | 0.6513(8) 0.7242(11) 0.5 | 0.3355(7) 0.5071(10) 0.0 | 0.8406(6) 0.7181(6) 0.8731(7) | 0.6698(7) 0.9793(10) 0.0 | 6.39 7.12 |
| B4_3 | 30.2(3) | 4.8767(3) | 5.4260(12) | 6.6606(9) | 0.1538(6) 0.5914(8) 0.7895(6) | 0.6518(9) 0.7234(13) 0.5 | 0.3359(9) 0.5066(11) 0.0 | 0.8411(7) 0.7178(9) 0.8733(6) | 0.6698(8) 0.9769(12) 0.0 | 6.92 8.18 |
| B4_4 | 35.5(3) | 4.8535(4) | 5.4025(13) | 6.6187(10) | 0.1534(6) 0.5902(7) 0.7885(5) | 0.6514(7) 0.7231(10) 0.5 | 0.3371(7) 0.5082(9) 0.0 | 0.8404(6) 0.7184(7) 0.8723(5) | 0.6691(7) 0.9776(9) 0.0 | 4.68 5.21 |
| B4_5 | 37.8(3) | 4.8346(3) | 5.3831(9) | 6.5920(6) | 0.1541(6) 0.5910(8) 0.7884(5) | 0.6519(8) 0.7229(12) 0.5 | 0.3358(8) 0.5072(10) 0.0 | 0.8410(6) 0.7188(8) 0.8724(5) | 0.6703(8) 0.9766(11) 0.0 | 6.02 6.92 |
| B4_6 | 45.1(3) | 4.8078(5) | 5.3532(17) | 6.5465(13) | 0.1537(6) 0.5902(8) 0.7878(5) | 0.6513(8) 0.7230(11) 0.5 | 0.3367(7) 0.5072(9) 0.0 | 0.8406(6) 0.7187(7) 0.8719(5) | 0.6701(7) 0.9765(10) 0.0 | 5.46 5.62 |
| B5_1 | 0.001 | 5.0508(2) | 5.6181(4) | 6.9793(5) | 0.1543(4) 0.5928(5) 0.7930(4) | 0.6481(6) 0.7279(7) 0.5 | 0.3357(5) 0.5072(6) 0.0 | 0.8386(4) 0.7195(5) 0.8737(4) | 0.6695(5) 0.9834(7) 0.0 | 6.61 7.43 |
| B5_2 | 5.8(1) | 5.0115(5) | 5.5731(10) | 6.9041(12) | 0.1542(4) 0.5921(5) 0.7917(3) | 0.6485(6) 0.7267(7) 0.5 | 0.3355(5) 0.5059(6) 0.0 | 0.8390(4) 0.7195(4) 0.8733(4) | 0.6701(5) 0.9820(7) 0.0 | 5.58 6.74 |
| B5_3 | 9.6(2) | 4.9810(2) | 5.5392(3) | 6.8535(4) | 0.1542(5) 0.5924(6) 0.7914(4) | 0.6483(6) 0.7277(8) 0.5 | 0.3364(6) 0.5079(7) 0.0 | 0.8392(4) 0.7198(5) 0.8731(4) | 0.6699(6) 0.9813(7) 0.0 | 6.28 7.59 |
| B5_4 | 14.7(2) | 4.9636(2) | 5.5192(4) | 6.8160(5) | 0.1542(6) 0.5921(7) 0.7907(5) | 0.6487(8) 0.7264(9) 0.5 | 0.3357(7) 0.5082(8) 0.0 | 0.8392(5) 0.7193(6) 0.8728(5) | 0.6710(7) 0.9798(8) 0.0 | 7.86 8.58 |
| B5_5 | 15.1(2) | 4.9267(2) | 5.4751(4) | 6.7439(6) | 0.1538(6) 0.5907(6) 0.7893(4) | 0.6499(9) 0.7253(8) 0.5 | 0.3353(8) 0.5064(7) 0.0 | 0.8403(6) 0.7184(5) 0.8722(5) | 0.6718(8) 0.9779(7) 0.0 | 5.42 5.95 |
| B5_6 | 21.5(2) | 4.8986(4) | 5.4462(9) | 6.6990(11) | 0.1544(4) 0.5910(4) 0.7887(3) | 0.6494(7) 0.7244(7) 0.5 | 0.3357(6) 0.5076(6) 0.0 | 0.8401(4) 0.7188(4) 0.8717(4) | 0.6712(6) 0.9779(6) 0.0 | 5.65 6.26 |
| B5_7 | 26.5(2) | 4.8715(3) | 5.4189(6) | 6.6651(7) | 0.1550(11) 0.5930(13) 0.7891(8) | 0.6481(18) 0.7187(16) 0.5 | 0.3352(14) 0.5092(13) 0.0 | 0.8389(10) 0.7146(10) 0.8732(9) | 0.6707(16) 0.9818(16) 0.0 | 10.17 15.55 |
| B5_8 | 31.7(3) | 4.8492(5) | 5.3910(10) | 6.6116(13) | 0.1542(5) 0.5912(7) 0.7873(5) | 0.6494(7) 0.7239(9) 0.5 | 0.3356(7) 0.5098(9) 0.0 | 0.8402(5) 0.7194(7) 0.8714(5) | 0.6712(7) 0.9756(9) 0.0 | 6.79 7.56 |
| B5_9 | 36.2(3) | 4.8246(6) | 5.3679(12) | 6.5713(11) | 0.1539(4) 0.5906(5) 0.7871(3) | 0.6495(6) 0.7240(7) 0.5 | 0.3358(6) 0.5093(7) 0.0 | 0.8409(4) 0.7189(5) 0.8713(4) | 0.6710(6) 0.9758(7) 0.0 | 4.63 5.72 |
| B5_10 | 41.2(3) | 4.8100(2) | 5.3531(5) | 6.5486(5) | 0.1542(5) 0.5905(6) 0.7867(3) | 0.6494(7) 0.7235(8) 0.5 | 0.3357(7) 0.5089(7) 0.0 | 0.8408(5) 0.7182(6) 0.8711(4) | 0.6716(7) 0.9754(7) 0.0 | 5.13 6.08 |
| B5_11 | 45.0(3) | 4.7857(3) | 5.3291(7) | 6.5091(7) | 0.1544(6) 0.5909(6) 0.7862(4) | 0.6498(8) 0.7227(8) 0.5 | 0.3366(7) 0.5086(7) 0.0 | 0.8407(5) 0.7180(6) 0.8709(5) | 0.6710(7) 0.9749(7) 0.0 | 5.02 5.98 |
| B5_12 | 51.2(4) | 4.7208(5) | 5.2508(12) | 6.4015(14) | 0.1543(11) 0.5912(12) 0.7858(9) | 0.6529(17) 0.7214(14) 0.5 | 0.3340(13) 0.5076(13) 0.0 | 0.8401(10) 0.7168(11) 0.8703(8) | 0.6731(14) 0.9729(12) 0.0 | 7.54 8.70 |
| B5_p1 | 65.3(5) | 4.731(3) | 5.280(5) | 6.4285(39) | 0.1533(12) 0.5891(9) 0.7844(6) | 0.6521(16) 0.7204(10) 0.5 | 0.3341(15) 0.5082(9) 0.0 | 0.8425(9) 0.7190(7) 0.8729(8) | 0.6705(15) 0.9763(10) 0.0 | 6.94 6.91 |
| B5_p2 | 55.6(5) | 4.772(3) | 5.318(5) | 6.486(7) | 0.1541(2) 0.5901(6) 0.7859(4) | 0.6506(9) 0.7221(7) 0.5 | 0.3369(7) 0.5079(8) 0.0 | 0.8415(6) 0.7190(1) 0.8712(4) | 0.6723(8) 0.9760(7) 0.0 | 5.55 5.60 |
| B28** | 0.001 | 5.0576(4) | 5.6245(8) | 6.9884(10) | 0.1539(3) 0.5938(2) 0.7924(2) | 0.6469(4) 0.7284(4) 0.5 | 0.3362(4) 0.5076(4) 0.0 | 0.8391(3) 0.7189(3) 0.8737(2) | 0.6690(4), 0.9823(4) 0.0 | 3.73 % 11.5 % |

\* The data have been processed with Crysalis software (Oxford Diffraction (2006) Crysalis RED, version 1.171.31.8. Oxford Diffraction Ltd., Abingdon, Oxfordshire). Crystal structure refinements on integrated intensities have been carried out with Jana2006 software (Petricek, V., Dusek, M., and Palatinus, L. (2006) Jana2006. The crystallographic computing system. Institute of Physics, Praha, Czech Republic)
\*\* E.Yu. Zarechnaya et al., Phys. Pev. Lett. **102**, 185501 (2009).

# 5     FULL LIST OF PUBLICATIONS (WITH PAPERS NOT INCLUDED INTO THE THESIS)

**[1].** E. Yu. Zarechnaya, L. Dubrovinsky, N. Dubrovinskaia, N. Miyajima, Y. Filinchuk, D. Chernyshov, and V. Dmitriev. Synthesis of an orthorhombic high pressure boron phase. *Sci. Technol. Adv. Mater, 9:044209-044212, 2008.*

**[2].** E. Yu. Zarechnaya, L. Dubrovinsky, N. Dubrovinskaia, Y. Filinchuk, D. Chernyshov, V. Dmitriev, N. Miyajima, A. El Goresy, H. F. Braun, S. Van Smaalen, I. Kantor, A. Kantor, V. Prakapenka, M. Hanfland, A. S. Mikhaylushkin, I. A. Abrikosov, S. I. Simak. Superhard semiconducting optically transparent high pressure phase of boron. *Phys. Rev. Lett., 102: 185501-185504, 2009.*

**[3].** E. Yu. Zarechnaya, N. Dubrovinskaia, and L. Dubrovinsky. Polarized Raman spectroscopy of high-pressure orthorhombic boron phase. *High Pressure Research 29:530-535, 2009.*

**[4].** E. Yu. Zarechnaya, N. Dubrovinskaia, L. Dubrovinsky, Y. Filinchuk, D. Chernyshov, V. Dmitriev. Growth of single crystals of B28 at high pressure and high temperatures. Journal of Crystal Growth (in press).

**[5].** E. Yu. Zarechnaya, N. Dubrovinskaia, R. Caracas, M. Merlini, M. Hanfland, Y. Filinchuk, D. Chernyshov, V. Dmitriev, L. Dubrovinsky. Pressure-induced isostructural phase transformation in $\gamma$-B$_{28}$. *Nature (submitted).*

## Papers not included into thesis

**[1].** N. Dubrovinskaia, L. Dubrovinsky, W.A. Crichton, E. Zarechnaya, E.I. Isaev and I.A. Abrikosov. Compressibility of boron-doped diamond. *High Pres. Res. 26: 79-85, 2006.*

**[2].** E. Yu. Zarechnaya, E. I. Isaev, S. I. Simak, Yu. Kh. Vekilov, L. S. Dubrovinsky, N. A. Dubrovinskaia, and I. A. Abrikosov. Ground-State Properties of Boron-Doped Diamond. *J Exp. Theor. Phys., 106, 4: 781–787, 2008.*

**[3].** E. Yu. Zarechnaya, N. V. Skorodumova, S. I. Simak, B. Johansson and E. I. Isaev. Theoretical study of linear monoatomic nanowires, dimer and bulk of Cu, Ag, Au, Ni, Pd and Pt. *Comp. Mat. Sci. 43, 3: 522-530, 2008.*

# 6    BIBLIOGRAPHY

Albert, B. and H. Hillebrecht (2009). "Boron: Elementary Challenge for Experimenters and Theoreticians." Angewandte Chemie-International Edition **48**(46): 8640-8668.

Amberger E., Stumpf W. (1981). "Gmelin Handbook of Inorganic Chemistry, Boron." 8th ed. (eds.: K.-C. Buschbeck), Springer, Berlin 13 2.

Amberger, E. and K. Ploog (1971). "Formation of Lattices of Pure Boron." Journal of the Less-Common Metals **23**(1): 21-&.

Ashcroft, N.W. and Mermin, N.D. (1976). "Solid State Physics." Harcourt Brace College Publishers, Fort Worth.

Benard, F., P. Moutou, et al. (1985). "Phase-Relations of Tourmaline Leucogranites and the Significance of Tourmaline in Silicic Magmas." Journal of Geology **93**(3): 271-291.

Blochl, P. E., (1994). "Projector augmented-wave method" Physical Review B **50**: 17953-17979.

Bonatti, E., J. R. Lawrence, et al. (1984). "Serpentinization of Oceanic Peridotites - Temperature-Dependence of Mineralogy and Boron Content." Earth and Planetary Science Letters **70**(1): 88-94.

Bylander, D. M., L. Kleinman, et al. (1982). "Self-Consistent Energy-Bands and Bonding of Nisi2." Physical Review B **26**(12): 6379-6383.

Chopra, N. G., R. J. Luyken, et al. (1995). "Boron-Nitride Nanotubes." Science **269**(5226): 966-967.

Damen, T. C., S. P. S. Porto, et al. (1966). "Raman Effect in Zinc Oxide." Physical Review **142**(2): 570-&.

Decker, B. F. and J. S. Kasper (1959). "The Crystal Structure of a Simple Rhombohedral Form Boron." Acta Crystallographica **12**(7): 503-506.

Dingwell, D. B., R. Knoche, et al. (1992). "The Effect of B2o3 on the Viscosity of Haplogranitic Liquids." American Mineralogist **77**(5-6): 457-461.

Donohue J. (1974). "The structures of the elements." Wiley, New York: 48 – 82.

Eremets, M. I., V. W. Struzhkin, et al. (2001). "Superconductivity in boron." Science 293(5528): 272-274.

Eremets M.I. (1996). "High Pressure experimental Methods." Oxford University Press, New York.

Fasalino L.G. (1965). "Heats of Solution of Crystalline and Amorphous Boron Oxide and Boric Acid". J. Chem. Engineering data 10: 373-374.

Fei Y., Wang Y. (2000). "High-temperature and high-pressure powder diffraction." Reviews in mineralogy and geochemistry, Hazen R.M. and Downs R.T. (eds) Mineral. Soc. Am., Washington D.C 41: 521-557.

Fogg, T. R. and R. A. Duce (1985). "Boron in the Troposphere - Distribution and Fluxes." Journal of Geophysical Research-Atmospheres **90**(Nd2): 3781-3796.

Gabel D., Endo Y. (2004). "Molecular Clusters of the Main Group Elements." (eds.: M. Driess, H. Noeth), VCH, Weinheim: 95–125.

Gabel, D. (1997). "Boron neutron capture therapy in oncology." Chemie in Unserer Zeit **31**(5): 235-240.

Gillespie, R. J. and E. A. Robinson (1962). "Sulphuric Acid Solvent System .3. Preparation and Structures of Some Complex Sulphatoborates." <u>Canadian Journal of Chemistry-Revue Canadienne De Chimie</u> **40**(5): 1009-&.

Golikova, O. A., V. K. Zaitsev, et al. (1974). "Thermal-Conductivity of Boron and of Its Crystal-Structure Analogs." <u>Physica Status Solidi a-Applied Research</u> **21**(2): 405-412.

Greenwood N.N. (1973). "Boron." In JC Bailar Jr, HJ Eméleus, R. Nyholm, A.F. Trotman-Dickenson (eds) Comprehensive Organic Chemistry, <u>Pergamon, Oxford</u>: 665-991.

Hamann D.R., Schlüter M., and Chaing C. (1979). "Norm-conserving pseudopotentials" <u>Phys. Rev. Lett.</u> 43: 1494.

Harrison W.A. (1966). "Pseudopotentials." <u>Benjamin, New York.</u>

Haussermann, U., S. I. Simak, et al. (2003). "Metal-nonmetal transition in the boron group elements." <u>Physical Review Letters</u> **90**(6): -.

Hayun, S., H. Dilman, et al. (2009). "The effect of aluminum on the microstructure and phase composition of boron carbide infiltrated with silicon." <u>Materials Chemistry and Physics</u> **118**(2-3): 490-495.

Hazen R.J., Finger L.W. (1982). "Comparative Crystal Chemistry." <u>John Willey&Sons, New York.</u>

Hemley R.J. (ed.) (1998)."Ultrahigh-pressure Mineralogy." <u>Rev. Mineralogy, New York</u> 37.

Hohenberg, P. and W. Kohn (1964). "Inhomogeneous Electron Gas." <u>Physical Review B</u> **136**(3B): B864-&.

Holcombe C.E. Jr., Smith D.D., Lorc J.D., Duerlesen W.K., Carpenter D.A. (1973). "Physucal-chemical properties of beta-Rhombohedral Boron", <u>High Temp. Sci</u> 5: 349.

Horn, F. H. (1959). "Some Electrical and Optical Properties of Simple Rhombohedral Boron." <u>Journal of Applied Physics</u> **30**(10): 1611-1612.

Humphris, S. E. and G. Thompson (1978). "Hydrothermal Alteration of Oceanic Basalts by Seawater." <u>Geochimica Et Cosmochimica Acta</u> **42**(1): 107-125.

Imai, Y., M. Mukaida, et al. (2001). "Screening of the possible boron-based n-type thermoelectric conversion materials on the basis of the calculated densities of states of metal borides and doped beta-boron." <u>Intermetallics</u> **9**(8): 721-734.

Kaneshige M., Hirayama S., Yabuuchi T., Matsuoka T., Shimizu K., Mita Y., Hyoudo H., Kimura K. (2007). "Measurement of Electrical Resistance and Raman Spectrum of $\alpha$-Boron under High Pressure." <u>J. Phys. Soc. Jpn.</u> 76: 19-20.

Kawai, N. and S. Endo (1970). "Generation of Ultrahig Hydrostatic Pressures by a Split Sphere Apparatus." <u>Review of Scientific Instruments</u> **41**(8): 1178-&.

Kawai, N., M. Togaya, et al. (1973). "New Device for Pressure-Vessels." <u>Proceedings of the Japan Academy</u> **49**(8): 623-626.

Kerker, G. P. (1980). "Non-Singular Atomic Pseudopotentials for Solid-State Applications." <u>Journal of Physics C-Solid State Physics</u> **13**(9): L189-L194.

Kitamura J., Usuba S., Kakudate Y., Yokoi H., Yamamoto K., Tanaka A., Fujiwara S. (2003). "Structure and mechanical properties of boron carbide coatings formed by electromagnetically accelerated plasma spraying." <u>Diamond and related materials</u> 12: 1891-1896.

Kobayashi, M., I. Higashi, et al. (1997). "Fundamental structure of amorphous boron." Journal of Solid State Chemistry **133**(1): 211-214.

Kohn, W. and L. J. Sham (1965). "Quantum Density Oscillations in an Inhomogeneous Electron Gas." Physical Review **1**(6A): 1697-&.

Kresse, G. and J. Furthmuller (1996). "Efficient iterative schemes for ab initio total-energy calculations using a plane-wave basis set." Physical Review B **54**(16): 11169-11186.

Laubengayer A.W., Hurd D.T., Newkirk A.E., Hoard J.I. (1943). "Boron. I. Preparation and Properties of Pure Crystalline Boron." J. Am. Chem. Soc. 65: 1924.

Leeman, W. P., V. B. Sisson, et al. (1992). "Boron Geochemistry of the Lower Crust - Evidence from Granulite Terranes and Deep Crustal Xenoliths." Geochimica Et Cosmochimica Acta **56**(2): 775-788.

Lin, J. F., J. Shu, et al. (2003). "Amorphous boron gasket in diamond anvil cell research." Review of Scientific Instruments **74**(11): 4732-4736.

Loiseau, A., F. Willaime, et al. (1996). "Boron nitride nanotubes with reduced numbers of layers synthesized by arc discharge." Physical Review Letters **76**(25): 4737-4740.

Ma, Y. Z., C. T. Prewitt, et al. (2003). "High-pressure high-temperature x-ray diffraction of beta-boron to 30 GPa." Physical Review B **67**(17): -.

Mcmahon, M. I. (2004). "High pressure diffraction from good powders, poor powders and poor single crystals". Katrusiak A. and McMillan P. (eds.). High-pressure crystallography/NATO Science.Series.140/ Dordrecht: kluwer: 1-20.

Mao, H. K., J. Xu, et al. (1986). "Calibration of the Ruby Pressure Gauge to 800-Kbar under Quasi-Hydrostatic Conditions." Journal of Geophysical Research-Solid Earth and Planets **91**(B5): 4673-4676.

Marder, T. B. (2007). "Will we soon be fueling our automobiles with ammonia-borane?" Angewandte Chemie-International Edition **46**(43): 8116-8118.

Masago, A., K. Shirai, et al. (2006). "Crystal stability of alpha- and beta-boron." Physical Review B **73**(10): -.

Mccarty, L. V., J. S. Kasper, et al. (1958). "A New Crystalline Modification of Boron." Journal of the American Chemical Society **80**(10): 2592-2592.

Miletich , R et al. (2000). " High-Pressure and High-Temperature Crystal Chemistry". Hazen, R. M. & Downs, R. T. (eds). DC: Mineralogical Society of America, Washington: 445-519.

MillenniumCell. http://www. aboutus.org/MillenniumCell.com

Mottl, M. J. and H. D. Holland (1978). "Chemical Exchange during Hydrothermal Alteration of Basalt by Seawater .1. Experimental Results for Major and Minor Components of Seawater." Geochimica Et Cosmochimica Acta **42**(8): 1103-1115.

Nagamatsu, J., N. Nakagawa, et al. (2001). "Superconductivity at 39 K in magnesium diboride." Nature **410**(6824): 63-64.

Nelmes, R. J., J. S. Loveday, et al. (1993). "Neutorn-Diffraction and X-Ray-Diffraction Measurements of the Bulk Modulus of Boron." Physical Review B **47**(13): 7668-7673.

Oganov A.R., Chen J., Gatti5 C., Ma Y., Ma Y., Glass C.W., Liu Zh., Yu T., Kurakevych O.O., Solozhenko V.L. (2009) "Ionic high-pressure form of elemental boron." Nature 457: 863-.

Ogitsu, T., F. Gygit, et al. (2009). "Imperfect Crystal and Unusual Semiconductor: Boron, a Frustrated Element." Journal of the American Chemical Society **131**(5): 1903-1909.

Oxford Diffraction (2006). Oxford diffraction Ltd., Xcalibur CCD system, CrysAlis Software system, Version 171.30.2.

Perdew, J. P., K. Burke, et al. (1996). "Generalized gradient approximation made simple." Physical Review Letters **77**(18): 3865-3868.

Pichavant, M. (1987). "Effects of B and H2o on Liquidus Phase-Relations in the Haplogranite System at 1-Kbar." American Mineralogist **72**(11-12): 1056-1070.

Ploog, K. and E. Amberger (1971). "Carbon Induced Boron." Journal of the Less-Common Metals **23**(1): 33-&.

Ploog, K., Kossobut. Kh, et al. (1972). "B48b2c2 and B48b2n2, 2 Non-Metal Borides with Structure of So-Called I-Tetragonal Boron." Journal of the Less-Common Metals **29**(2): 161-&.

Pyzik, A. J. and D. R. Beaman (1995). "Al-B-C Phase Development and Effects on Mechanical-Properties of B4c/Al-Derived Composites." Journal of the American Ceramic Society **78**(2): 305-312.

Riedel, R. (1994). "Novel Ultrahard Materials." Advanced Materials **6**(7-8): 549-560.

Riedel R. (2000). "Handbook of Ceramic Hard Materials" (Ed.: R. Riedel), VCH, Weinheim.

Ross V.F., Edwards J.O. (1967). "The structural chemestry of the borates, In EL Muetterties (ed) The Chemistry of Boron and its Compounds." Wiley, New York, NY: 155-207.

Rubie, D. C. (1999). "Characterising the sample environment in multianvil high-pressure experiments." Phase Transitions **68**(3): 431-451.

Rubie, D. C., S. Karato, et al. (1993). "Low Differential Stress and Controlled Chemical Environment in Multianvil High-Pressure Experiments." Physics and Chemistry of Minerals **20**(5): 315-322.

Sanz, D. N., P. Loubeyre, et al. (2002). "Equation of state and pressure induced amorphization of beta-boron from X-ray measurements up to 100 GPa." Physical Review Letters **89**(24): -.

Schlapbach, L. and A. Zuttel (2001). "Hydrogen-storage materials for mobile applications." Nature **414**(6861): 353-358.

Seyfried, W. E., D. R. Janecky, et al. (1984). "Alteration of the Oceanic-Crust - Implications for Geochemical Cycles of Lithium and Boron." Geochimica Et Cosmochimica Acta **48**(3): 557-569.

Shaw, D. M., M. G. Truscott, et al. (1988). "Boron and Lithium in High-Grade Rocks and Minerals from the Wawa-Kapuskasing-Region, Ontario." Canadian Journal of Earth Sciences **25**(9): 1485-1502.

Sheldrick G.M.(1997) (a) "SADABS" University of Gottingen, Germany.

Sheldrick G.M. (1997) (b). "SHELXS97 and SHELXL97." University of Gottingen, Germany.

Slack, G. A., C. I. Hejna, et al. (1988). "The Crystal-Structure and Density of Beta-Rhombohedral Boron." Journal of Solid State Chemistry **76**(1): 52-63.

Taylor S.R., McLennan S.M. (1985)."The Continental Crust: its Composition and Evolution. An Examination of the Geochemical record Preserved in Sedimentary Rocks." Blackwell, Oxford.

Taylor, S. R. and S. M. Mclennan (1995). "The Geochemical Evolution of the Continental-Crust." Reviews of Geophysics **33**(2): 241-265.

Telle, R. (1988). "Borides, a New Generation of Hard Substances." Chemie in Unserer Zeit **22**(3): 93-99.

Thompson, G. and W. G. Melson (1970). "Boron Contents of Serpentinites and Metabasalts in Oceanic Crust - Implications for Boron Cycle in Oceans." Earth and Planetary Science Letters **8**(1): 61-&.

Vanderbilt, D. (1990). "Soft Self-Consistent Pseudopotentials in a Generalized Eigenvalue Formalism." Physical Review B **41**(11): 7892-7895.

Viala, J. C., G. Gonzales, et al. (1992). "Composition and Lattice-Parameters of a New Aluminum-Rich Borocarbide." Journal of Materials Science Letters **11**(10): 711-714.

Wade, K. (1972). "Skeletal Bond Orders in Borane Anions Bnhn2- and Related Closo-Cluster Species." Inorganic & Nuclear Chemistry Letters **8**(9): 823-&.

Wentorf R.H. (1965) "Boron:Another form." Science 147:49-50.

Werheit, H. (1970). "Optical and Photoelectrical Properties of Beta-Rhombohedral Boron .2. Photoeffects." Physica Status Solidi **39**(1): 109-&.

Werheit, H. (1995). "Boron-Rich Solids - a Chance for High-Efficiency High-Temperature Thermoelectric Energy-Conversion." Materials Science and Engineering B-Solid State Materials for Advanced Technology **29**(1-3): 228-232.

Wilkins M.L. (1977). "Boron and Refractory Borides." (ed. by V. I. Matkovich) Springer, Berlin: 633–648.

Will, G. and K. Ploog (1974). "Crystal-Structure of I-Tetragonal Boron." Nature **251**(5474): 406-408.

Yoon, C. W., P. J. Carroll, et al. (2009). "Ammonia Triborane: A New Synthesis, Structural Determinations, and Hydrolytic Hydrogen-Release Properties." Journal of the American Chemical Society **131**(2): 855-864.

Zhang, H., Q. Zhang, et al. (2005). "Single-crystal line GdB6 nanowire field emitters." Journal of the American Chemical Society **127**(38): 13120-13121.

Zhao, J. J. and J. P. Lu (2002). "Pressure-induced metallization in solid boron." Physical Review B **66**(9): -.

Zuttel, A., A. Borgschulte, et al. (2007). "Tetrahydroborates as new hydrogen storage materials." Scripta Materialia **56**(10): 823-828.

# 7   ACKNOWLEDGMENTS

Last, but not least, I thank my parents, Marina Zarechnaya and Yuri Zarechniy, for educating me in different aspects, and for unconditional support and encouragement in everything and believing in me.

## Erklärung

Hiermit erkläre ich, dass ich die Arbeit selbständing verfasst und keine anderen als die von mir angegebenen Quellen und Hilfsmittel benutzt habe.

Ferner erkläre ich, dass ich anderweitig mit oder ohne Erfolg nicht versucht habe, diese Dissertation einzureichen. Ich habe keine gleichartige Doktorprüfung an einer anderen Hochschule endgültig nicht bestanden.

Bayreuth, im April 2010

Zarechnaya Evgeniya